# Atomically dispersed antimony on carbon nitride for the artificial photosynthesis of hydrogen peroxide

| | |
|---|---|
| 著者 | Teng Zhenyuan, Zhang Qitao, Yang Hongbin, Kato Kosaku, Yang Wenjuan, Lu Ying-Rui, Liu Sixiao, Wang Chengyin, Yamakata Akira, Su Chenliang, Liu Bin, Ohno Teruhisa |
| journal or publication title | Nature Catalysis |
| volume | 4 |
| number | 5 |
| page range | 374-384 |
| year | 2021-05-21 |
| URL | http://hdl.handle.net/10228/00008562 |

doi: https://doi.org/10.1038/s41929-021-00605-1

This is the accepted version of the following article: https://www.nature.com/articles/s41929-021-00605-1, which has been published in final form at https://doi.org/10.1038/s41929-021-00605-1.

# Atomically Dispersed Antimony on Carbon Nitride for the Artificial Photosynthesis of Hydrogen Peroxide

Zhenyuan Teng,[1,7,8] Qitao Zhang,[2,8] Hongbin Yang,[3,8] Kosaku Kato,[4] Wenjuan Yang,[2] Ying-Rui Lu,[5] Sixiao Liu,[6,7] Chengyin Wang,[6,7] Akira Yamakata,[4] Chenliang Su,[2,*] Bin Liu,[3,*] and Teruhisa Ohno[1,7,*]

[1]Department of Applied Chemistry, Faculty of Engineering, Kyushu Institute of Technology, Kitakyushu 804-8550, Japan

[2]International Collaborative Laboratory of 2D Materials for Optoelectronics Science and Technology of Ministry of Education, Institute of Microscale Optoelectronics, Shenzhen University, Shenzhen 518060, China

[3]School of Chemical and Biomedical Engineering, Nanyang Technological University, 62 Nanyang Drive, Singapore 637459, Singapore

[4]Graduate School of Engineering, Toyota Technological Institute, 2-12-1 Hisakata, Tempaku Nagoya 468-8511, Japan

[5]National Synchrotron Radiation Research Center, Hsinchu 30076, Taiwan

[6]College of Chemistry and Chemical Engineering, Yangzhou University, 180 Si-Wang-Ting Road, Yangzhou 225002, China

[7]Joint Laboratory of Yangzhou University, Kyushu Institute of Technology, Yangzhou University, 180 Si-Wang-Ting Road, Yangzhou 225002, China

[8]These authors contributed equally.

ORCID:

Teruhisa Ohno: https://orcid.org/0000-0002-7825-8189

Chenliang Su: https://orcid.org/0000-0002-8453-1938

Bin Liu: https://orcid.org/0000-0002-4685-2052

E-mail address:

Teruhisa Ohno: tohno@che.kyutech.ac.jp

Chenliang Su: chmsuc@nus.edu.sg

Bin Liu: liubin@ntu.edu.sg

**Commented [TB1]:** * The choice of title is largely yours and must be under 150 characters. However, we think it may be good to include "carbon nitride" so we suggest the alternative:

"Atomically Dispersed Antimony on Carbon Nitride for the artificial Photosynthesis of Hydrogen Peroxide"

**Commented [TB2R1]:** We agree with the editor that the revised title is more specific. We have changed the title of this work.

## Abstract

Artificial photosynthesis offers a promising strategy to produce hydrogen peroxide ($H_2O_2$) – an environmentally friendly oxidant and a clean fuel. However, the low activity and selectivity of the two-electron oxygen reduction reaction (ORR) in the photocatalytic process greatly restricts the $H_2O_2$ production efficiency. Here we show a robust antimony single-atom photocatalyst (Sb-SAPC, single-Sb-atom dispersed on carbon nitride) for the synthesis of $H_2O_2$ in a simple water and oxygen mixture under visible light irradiation. An apparent quantum yield of 17.6% at 420 nm together with a solar-to-chemical conversion efficiency of 0.61% for $H_2O_2$ synthesis was achieved. Based on time-dependent density function theory calculations, isotopic experiments and advanced spectroscopic characterizations, the outstanding photocatalytic performance is ascribed to the significantly promoted two-electron ORR by forming *μ*-peroxide at the Sb sites and highly concentrated holes at the neighboring N atoms. The *in-situ* generated $O_2$ via water oxidation is rapidly consumed by ORR, leading to boosted overall reaction kinetics.

## Introduction

Hydrogen peroxide ($H_2O_2$) is an important green oxidant[1] widely used in a variety of industries and a promising clean fuel for jet car and rockets[2-7] (60 wt.% $H_2O_2$ has an energy density of 3.0 MJ $L^{-1}$, higher than compressed $H_2$ gas at 35 MPa, 2.8 MJ $L^{-1}$). Currently, $H_2O_2$ is manufactured by the energy-consuming, waste-intensive, and indirect anthraquinone method[8,9]. Photocatalytic $H_2O_2$ synthesis on semiconductor materials from water and oxygen has emerged as a safe, environmental-friendly and energy-saving process[10,11]. To achieve high selectivity and rate for $H_2O_2$ production, it is crucial to boost the $2e^-$ oxygen reduction reaction (ORR, Equation 1)[12] or the $2e^-$ water oxidation reaction (WOR, Equation 2)[13]. The light-driven $2e^-$ WOR pathway is difficult to be achieved because of the uphill thermodynamics (1.76 V vs. NHE), i.e. the as-synthesized $H_2O_2$ will decompose at this highly oxidative potential since $H_2O_2$ is an excellent hole scavenger[11,14,15]. On the contrary, the $2e^-$ ORR pathway has been realized for artificial photosynthesis of $H_2O_2$ in several particulate systems[12,16-23]. However, the highest apparent quantum yield (ΦAQY) for non-sacrificial $H_2O_2$ production (Equation 3) is still smaller than 8% (at λ = 420 nm)[16-24], much lower than the highest ΦAQY values reached



**Commented [TB3]:** The abstract — which should be roughly 150 words long and contain no references — should serve both as a general introduction to the topic and a non-technical summary of your main results and their implications. It should contain a brief account of the background and rationale of the work, followed by a statement of the main conclusions introduced by the phrase 'Here we show' or some equivalent phrase. Because we hope that researchers in a wide range of disciplines will be interested in your work, the abstract should be as accessible as possible, explaining essential but specialized terms concisely. We encourage you to show your abstract to colleagues outside of your direct field of expertise to uncover any problematic concepts.

**Commented [TB4R3]:** We have revised the abstract to meet the requirements.

**Commented [TB5]:** Please remove this, We avoid the use of phrases such as 'novel', 'for the first time', 'record', etc. This should be clear from the context.

**Commented [TB6R5]:** We have revmoved all phrases of ('novel', 'for the first time', 'record') in both manuscript and supplementary informantion.

**Commented [TB7]:** spectroscopic

**Commented [TB8R7]:** We have revised the word 'spectral' to 'spectroscopic'.

**Commented [TB9]:** Please avoid the repetition of because, change to "since"

**Commented [TB10R9]:** We have change the word 'because' to 'since' to avoid the repetition.

**Commented [TB11]:** In the introduction, we realised that some sentences have a high degree of overlap with your recent https://doi.org/10.1016/j.apcatb.2020.119589. Please revise the sentences or add the appropriate citation to this work.

**Commented [TB12R11]:** We have added the appropratiate citations.

for overall water splitting (~30% at λ = 420 nm)[25]. To boost the photocatalytic activity for the non-sacrificial $H_2O_2$ production, both $2e^-$ ORR (Equation 2) and $4e^-$ WOR (Equation 4) should be promoted simultaneously. Unlike some other photocatalytic processes (e.g., overall water splitting and $N_2$ fixation)[25,26], these redox reactions cannot be separately considered as irrelevant half reactions, since $O_2$ is not only a product in the $4e^-$ WOR (Equation 4), but also a reactant in the $2e^-$ ORR (Equation 1). If the *in-situ* generated $O_2$ from WOR (Equation 4) can be consumed rapidly by ORR, it will kinetically facilitate the WOR. Therefore, introducing highly active and selective sites for the $2e^-$ ORR in the photocatalytic system to consume the $O_2$ generated from the WOR shall offer a promising strategy for breaking the bottleneck of photocatalytic $H_2O_2$ synthesis.

$$O_2+2H^++2e^-\rightarrow H_2O_2 \quad (0.695\ V\ vs.\ NHE) \quad (1)$$

$$2H_2O\rightarrow H_2O_2+2H^++2e^- \quad (1.76\ V\ vs.\ NHE) \quad (2)$$

$$2H_2O+O_2\rightarrow 2H_2O_2 \quad (3)$$

$$2H_2O+4h^+\rightarrow O_2+4H^+ \quad (1.23\ V\ vs.\ NHE) \quad (4)$$

$$O_2+4H^++4e^-\rightarrow 2H_2O \quad (1.23\ V\ vs.\ NHE) \quad (5)$$

Manipulating metallic sites can change both the activity and selectivity of ORR[27]. The $O_2$ molecular adsorption on metal surface can be generally classified into three types (Figure 1a): Pauling-type (end-on), Griffiths-type (side-on), and Yeager-type (side-on)[27,28]. The end-on $O_2$ adsorption configuration is able to minimize the O-O bond breaking, leading to a suppressed $4e^-$ ORR (Equation 5), and thus, a highly selective $2e^-$ ORR. On metal particles, both end-on and side-on $O_2$ molecular adsorption exist, and thus the O-O bond splitting on the surface of metal particles can hardly be prevented[29,30]. Benefiting from the desirable features of single atom catalyst (SAC), the adsorption of $O_2$ molecules on atomically isolated sites is usually end-on type, which therefore could reduce the possibility of O-O bond breaking (Figure 1b)[31-34]. For instance, SACs with $Pt^{2+}$ [35] and Co-$N_4$[36,37] centers could electrochemically reduce $O_2$ to $H_2O_2$ via a $2e^-$ ORR pathway with ultrahigh selectivity (>96 %). However, $Pt^{2+}$ and Co-$N_4$ sites can hardly be coupled in the photocatalytic system due to their high charge recombination characteristics, which originate from the intermediate band formed by the half-filled d electrons. Constructing photocatalysts with atomically dispersed elements possessing the $d^{10}$ electronic

**Commented [TB13]:** the highest AQY values reached for

**Commented [TB14R13]:** We have changed the word ' current record ΦAQY for' to 'the highest ΦAQY values reached for'.

configuration can eliminate the formation of the intermediate band in the band structure, which shall be favorable for efficient charge separation and formation of reactive centers with high density of electrons/holes[15,38,39]. This implies that SACs with $d^{10}$ electronic configuration would be ideal candidates for photocatalytic $H_2O_2$ synthesis via the $2e^-$ ORR.

Herein, we develop a Sb single atom photocatalyst (Sb-SAPC) for non-sacrificial photocatalytic $H_2O_2$ synthesis in a water and oxygen mixture under visible light irradiation, in which the oxidation state of Sb is regulated to +3 with a $4d^{10}5s^2$ electron configuration. Notably, an apparent quantum efficiency of 17.6% at 420 nm and a solar-to-chemical conversion (SCC) efficiency of 0.61% are achieved on the as-developed photocatalyst. Combining experimental and theoretical investigations, it is found that the adsorption of $O_2$ on isolated Sb atomic sites is end-on type, which promotes formation of Sb-*μ*-peroxide (Sb-OOH), leading to an efficient $2e^-$ ORR pathway for $H_2O_2$ production. More importantly, the Sb sites also induce highly concentrated holes at the neighboring melem units, promoting the $4e^-$ WOR. The concept of using SAC to simultaneously boost reduction and oxidation reactions shall provide a design guide to develop more advanced photocatalytic systems for extensive applications.

**Commented [TB15]:** please rephrase

**Commented [TB16R15]:** We have revmoved the word record-high.

**Commented [TB17]:** this can be removed

**Commented [TB18R17]:** The word “the” has been removed.

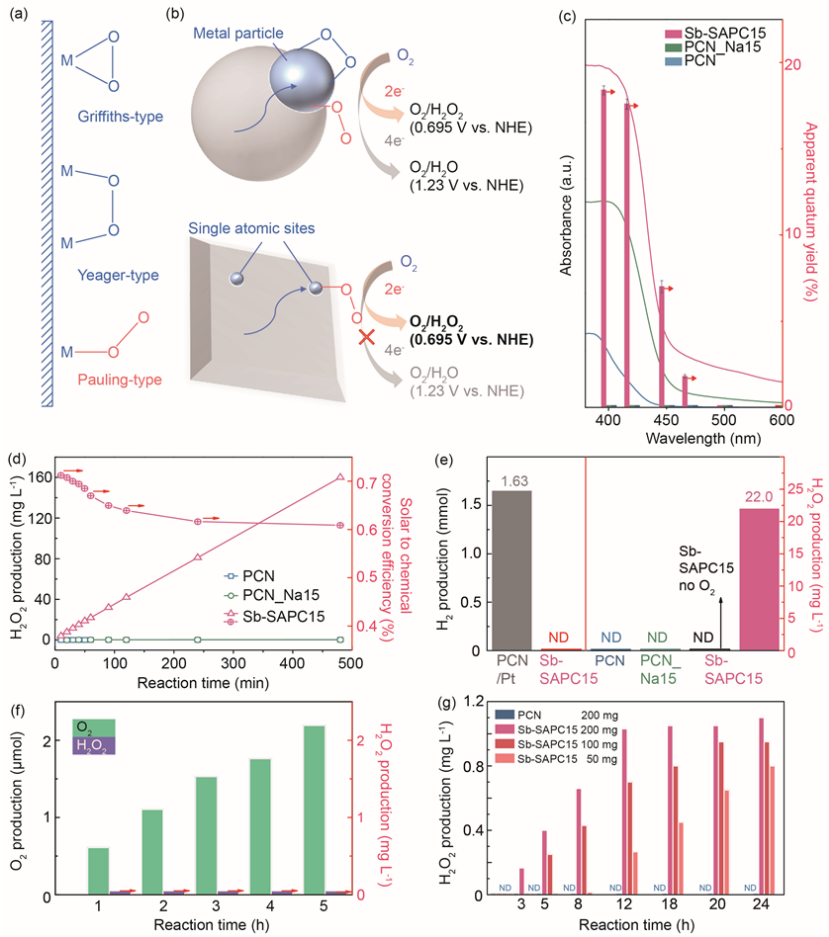


**Figure 1 | Photocatalytic performance of Sb-SAPC toward $H_2O_2$ production. a**, Schematic structures of $O_2$ adsorption on metal surface. **b**, ORR on a metal particle (top) and an isolated atomic site (bottom). **c**, Action spectra of PCN, PCN_Na15 and Sb-SAPC15 toward $H_2O_2$ production in a phosphate buffer solution (pH = 7.4). Error bars represent the standard deviations of 3 replicate measurements. **d**, Solar-to-chemical conversion efficiency of PCN, PCN_Na15 and Sb-SAPC15 under AM 1.5 illumination in a phosphate buffer solution. **e**, Selectivity comparison of Sb-SAPC15 and pristine PCN for different photoreduction reactions (Reaction time: 1h). Left: comparison of hydrogen evolution activity of Sb-SAPC15 and PCN loaded with 1 wt.% Pt in a 10% (v/v) 2-propanol aqueous solution. Right: comparison of activity for photocatalytic $H_2O_2$ production on pristine PCN, PCN_Na15 and Sb-SAPC15 in a phosphate

buffer solution with or without $O_2$. **f**, Amount of $O_2$ and $H_2O_2$ produced on Sb-SAPC15 in $NaIO_3$ (0.1 M, as the electron acceptor) solution. **g**, Photocatalytic $H_2O_2$ production with electron acceptor (0.1 mM $Ag^+$) under $N_2$ atmosphere. Irradiation condition: λ > 420 nm (Xe lamp, light intensity at 420-500 nm: 30.3 W $m^{-2}$), at 298 K. NDs in Figure 1e and Figure 1g mean that $H_2O_2$ cannot be detected in the photocatalytic system.

## Results

### *Photocatalytic $H_2O_2$ production on Sb-SAPC*

The Sb-SAPC was prepared by a wet chemical method using $NaSbF_6$ and melamine as the precursor (Supplementary Figure 1). Control samples including pristine polymetric carbon nitride (PCN) and $Na^+$ incorporated PCNs, were also prepared for references. According to the amount of metal salt added (x = 0.5, 1, 3, 5, 10, 15 or 20 mmol of NaF or $NaSbF_6$) into 4 g melamine, the samples are denoted as PCN_Nax or Sb-SAPCx, respectively. The as-prepared Sb-SAPC reached a quantity of 100 grams in one batch, which is very promising for scalable production (Supplementary Figure 2).

The photocatalytic performance of Sb-SAPC for $H_2O_2$ production was assessed in a water and oxygen mixture without presence of any sacrificial agents under visible light illumination. As shown in Supplementary Figure 3, Sb-SAPC15 shows the highest $H_2O_2$ production rate (12.4 mg $L^{-1}$ in 120 min) among the samples, which is about 248 times higher than pristine PCN (0.05 mg $L^{-1}$ in 120 min). The surface area of Sb-SAPC15 (1.89 $m^2$ $g^{-1}$, Supplementary Figure 4) is only about 1/7.78 of pristine PCN (14.7 $m^2$ $g^{-1}$), indicating that the activity per area enhancement induced by introducing Sb into PCN is increased by more than 1900 folds as compared to pristine PCN. After we optimized the reaction conditions (Supplementary Figures 5-6)[19], the action spectra (Figure 1c) for $H_2O_2$ production were measured. The ΦAQY of Sb-SAPC15 at 420 nm is determined to be 17.6%, which is twice of the most efficient photocatalyst (RF-resin, Supplementary Table 1) for non-sacrificial $H_2O_2$ production[16]. The solar-to-chemical conversion efficiency of Sb-SAPC15 reaches as high as 0.61% (Figure 1d), comparable with the most efficient water splitting photocatalyst (~0.8%)[25]. Interestingly, the Sb-SAPC15 displays negligible photocatalytic activity for the hydrogen evolution reaction (Figure 1e, left). Furthermore, by



**Commented [TB19]:** * We do not use combined "Results and Discussion" section. Please change to "Results".

**Commented [TB20R19]:** We have changed the word "Results and Discussion" to "Results".

**Commented [TB21]:** Please shorten any section subheadings that are longer than 60 characters (including spaces).

**Commented [TB22R21]:** This section subheading has been shortened to be no longer than 60 characters (including spaces).

**Commented [TB23]:** Our style does not allow for the use of Schemes.
Please change this into a Supplementary Figure.
* Supplementary Figures should be referred to as 'Supplementary Figure 1', etc., in both the SI and main text. Note that the 'S' prefix is not used in the SI-

**Commented [TB24R23]:** We have revised all the styles of Figures in the revised manuscript and supplementary information.

comparing the photocatalytic products at two different reaction conditions (with and without $O_2$), the $H_2O_2$ is clearly shown to be produced via the $2e^-$ ORR (no $H_2O_2$ was detected in the photocatalytic system without $O_2$, Figure 1e, right). Besides activity, more than 95% of the initial activity (Sb-SAPC15) could be maintained after 5 consecutive photocatalytic runs indicating the good stability (Supplementary Figure 7a). Reproducibilities of Sb-SAPC15 (5 different batches) are also excellent for AQY and SCC measurements (Supplementary Figures 7b-c). The long-term stability and potential for scalable photocatalytic $H_2O_2$ production using the Sb-SAPC photocatalyst were demonstrated in a fixed bed reactor (Supplementary Figure 8).

To study the overall reaction for photocatalytic $H_2O_2$ production, the half redox reactions on Sb-SAPC15 were separately investigated as follows: Sb-SAPC15 in a 2-propanol aqueous solution (2-propanol as an electron donor, 10% v/v) with saturated $O_2$ (Supplementary Figure 9) and in a $NaIO_3$ aqueous solution ($NaIO_3$ as an electron acceptor) with $N_2$ (Figure 1f and Supplementary Figure 10) respectively under visible light irradiation, which confirm that the $H_2O_2$ is indeed produced via the ORR on Sb-SAPC15. Isotope experiments[16] (Supplementary Figure 11) were further performed to verify the $4e^-$ WOR mechanism, in which Sb-SAPC15 in $H_2{}^{16}O$ and $^{18}O_2$ gas was irradiated for 6, 24 and 72 h. $Fe^{3+}$ and high concentration $H^+$ were added into the reaction system to decompose $H_2O_2$ to release $O_2$, and the evolved gas was analyzed by gas chromatography-mass spectrometry. The gaseous product obtained after 6 h reaction exhibits a strong $^{18}O_2$ (m/z) peak (94.5%) and a weak $^{16}O_2$ (m/z) peak (25.2%), manifesting that $H_2{}^{18}O_2$ was produced by $O_2$ reduction at the initial stage of the reaction. The gaseous product obtained with increasing reaction time shows a decreased intensity of $^{18}O_2$ peak (24 h: 55.7%; 72 h: 45.5%) and an increased intensity of $^{16}O_2$ peak (24 h: 32.5%; 72 h: 45.5%), indicating that the oxygen generated by WOR gradually participated in the ORR process[16].

To quantitatively reveal the relationship between the WOR and ORR, low-concentration electron acceptor (0.1 mM $Ag^+$) was added into the PCN and Sb-SAPC system in the absence of $O_2$. In this case, $H_2O_2$ can only be produced via the reduction of $O_2$ generated from water oxidation. PCN showed no photocatalytic activity in this condition, while Sb-SAPC gradually produced $H_2O_2$ in a certain time interval. After that, the $H_2O_2$ concentration

kept constant ~1.0 mg $L^{-1}$ no matter how much catalyst was used (Figure 1g). The quantitive relationship between the amount of added $Ag^+$ and $H_2O_2$ produced from WOR is discussed in Supplemenatary note 1. Isotope experiment using $H_2{}^{18}O$ was also conducted to confirm that the $H_2O_2$ generated in the system is indeed derived from the $O_2$ produced by the $4e^-$ WOR process (Supplementary Figure 12). The intensity of ${}^{18}O_2$ peak (m/z=36) gradually increases with increasing reaction time, indicating that $H_2{}^{18}O_2$ is originated from the ${}^{18}O_2$ generated by WOR. Therefore, the $O_2$ generated from WOR in Sb-SAPC system was rapidly consumed by the $2e^-$ ORR process to produce $H_2O_2$.

***Characterization of Sb-SAPC***

To understand the superb photocatalytic performance of Sb-SAPC for $H_2O_2$ production, the catalyst synthesis process (Supplementary Figures 13-17, Supplementary note 2) and the structural characteristics of the as-synthesized catalysts were carefully investigated. As revealed in the ζ-potential measurements, negative surface charges appeared on the as-prepared Sb-SAPCs to neutralize the positive charges induced by the incorporated Na and Sb cations (Supplementary Figure 18). The crystalline structures of Sb-SAPCx show no obvious changes as compared to the pristine PCN, as evidenced in the XRD patterns and high-resolution transmission electron microscopy (HRTEM) images (Supplementary note 3, Supplementary Figures 19-20). As a powerful tool for visualizing individual heavy atoms, high-angle annular dark-field scanning transmission electron microscopy (HAADF-STEM) was used to further examine the morphology and elemental distribution. The Sb-SAPC15 is composed of aggregated two-dimensional nanosheets, on which Sb and Na elements are homogeneously distributed (Supplementary Figure 21). For Sb-SAPC0.5, 1, 3, 5, 10 and 15, Supplementary Figure 22 and Figure 2a show that the bright spots with high density are uniformly dispersed in the entire carbon nitride matrix. The electron energy loss spectroscopy (EELS) (Figure 2b and Supplementary Figure 23) measurement reveals the bright spots corresponding to Sb atoms. The size distribution as displayed in Figure 2a shows that 99.6% of Sb species are less than 0.2 nm, demonstrating that Sb exists exclusively as isolated single atoms[40]. The mass ratio of Sb species in Sb-SAPC15 (10.9 wt.%, Supplementary Table 2) is considerably larger than that of the noble or transition

metal single atom species in many reported SACs.

To investigate the interaction between the isolated Sb atoms and the PCN skeleton, FT-IR and XPS measurements were conducted. The spectra of PCN, PCN_Na15 and Sb-SAPC15 show no obvious difference in the wavenumber range of 700-900 $cm^{-1}$ and 1200-1600 $cm^{-1}$ (Supplementary Figure 24), indicating that the skeleton of PCN hardly changes before and after incorporation of Na and Sb ions (Supplementary Table 3, Supplemental note 4). All fluoride elements have been removed during the cacination process (Supplementary Figures 25-26). In the high-resolution C 1s spectrum of pristine PCN (Figure 2c), the typical components at around 287.6 and 284.6 eV can be indexed as the C=N and adventitious carbon, respectively. It is important to note that a new nitrogen peak (N 1s) emerges at 398.1 eV in the spectrum of Sb-SAPC15 (Figure 2d), which can be assigned to the chemical bond of Sb-N. The binding energy of Sb 3d for Sb-SAPC15 (Sb $3d_{3/2}$ at 539.5 eV and Sb $3d_{5/2}$ at 530.2 eV) is close to that for $Sb_2O_3$ (Sb $3d_{3/2}$ at 539.8 eV and Sb $3d_{5/2}$ at 530.5 eV)[41], indicating that the oxidation state of Sb in Sb-SAPC15 is close to +3 (Figure 2e).

The oxidation state of the Sb atoms in Sb-SAPC15 was further determined by the position of the absorption edge in the Sb K-edge X-ray absorption near edge structure (XANES) (Figure 2f). The absorption edge for Sb-SAPC15 is 2.2 eV higher than that for the $Sb^0$ foil, and 1.5 eV lower than that for $Sb^{+5}{}_2O_5$, suggesting around +3 valence state of the Sb atoms in Sb-SAPC15. FT-EXAFS spectrum (Figure 2g) obtained from $k^3$-weighted k-space (Supplementary Figure 27) of Sb-SAPC15 shows only one peak at about 1.53 Å, and no Sb-Sb bond at 2.71 Å can be detected, implying that the Sb sites in Sb-SAPC15 are atomically dispersed. The coordination structure of the Sb atoms was estimated by fitting the EXAFS spectrum of Sb-SAPC15 using Artemis (version 0.9.25)[42] (Figure 2h, Supplementary Table 4) based on the DFT optimization result of the carbon nitride cluster with single Sb sites (Melem_3Sb3+, Supplementary Figure 28c). The best fitting result for the first shell shows that each Sb atom is coordinated with 3.3 N atoms in average and can be fitted well with the optimized DFT model (Supplementary Figure 28d), further indicating that the Sb species are atomically dispersed, consistent with the HAADF-STEM results (Figure 2a and Supplementary Figure 22). It is noteworthy that post-characterizations of

Sb-SAPC15 after continuous reaction for 5 days are almost the same as the fresh one (Supplementary Figure 29), confirming the excellent stability of Sb-SAPC (Supplementary Figure 7, note 5).

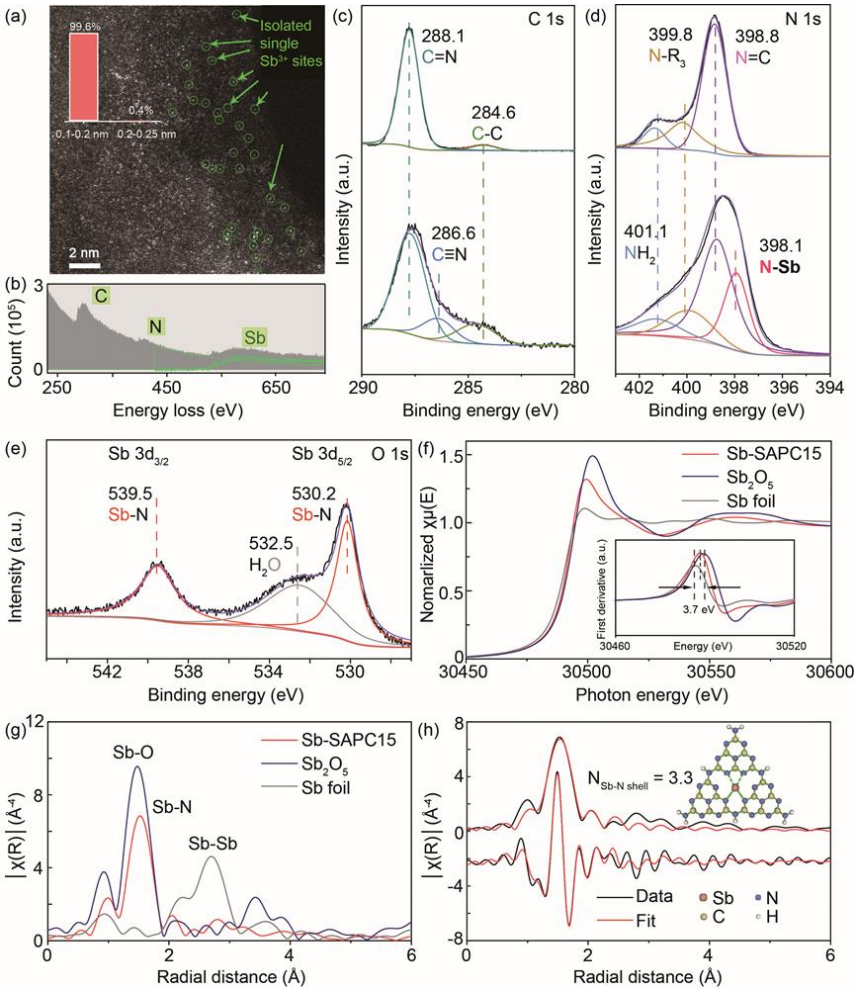


**Figure 2 | Characterization of Sb-SAPC. a**, High-magnification HAADF-STEM image of Sb-SAPC15. Inset is the size distribution of the bright spots. **b**, EELS spectrum of Sb-SAPC15. **c-e**, High-resolution C 1s (**c**) and N 1s XPS spectra (**d**) of PCN (up) and Sb-SAPC15 (down) and Sb 3d XPS spectrum (**e**) of Sb-SAPC15. **f**,**g**, Sb-K edge XANES (**f**) and Fourier transform-extended X-ray absorption fine structure (FT-EXAFS) spectra (**g**) of the Sb foil, $Sb_2O_5$ and Sb-SAPC15. **h**, Fitting of the EXAFS data of the Sb-SAPC15

based on the model obtained from DFT optimization. Inserted figures: optimized molecular models based on DFT for EXAFS fitting.

### *Properties of Sb-SAPC and photocatalytic mechanism*

The optical properies and the band diagram of Sb-SAPC were investigated. The introduction of Sb and Na species slightly narrowed the bandgap (2.77 eV for PCN and 2.63 eV for Sb-SAPC15) and significantly improved the light absorbance (Figure 1c and Supplementary Figure 30a-b). Confirmed by valence-band XPS and Mott-Schottky measurements, the introduction of Na and/or Sb species slightly shifted the conduction band minimum (CBM) from ~-1.3 eV (vs. NHE) to ~-1.2 eV while rarely influencing the valence band maximun (~1.45 eV) (Supplementary Figure 30c-g, Supplementary note 6).

The charge separation and recombination process were monitored by steady-state photoluminescence emission (PL) spectroscopy (Supplementary Figure 31a).[43] The radiative recombination of excited charge pairs was clearly observed in pristine PCN while the PL intensity was markedly reduced with addition of Sb and/or Na, indicating that the radiative recombination was greatly retarded after addition of Sb and/or Na species. This phenomenon is consistent with the highest photocatalytic activity of Sb-SAPC15. In addition, the onset of PL wavelength gradually red-shifted, which is also consistent with the narrowed bandgap. The facilitated charge migration in Sb-SAPC15 could be further verified by the enhanced photocurrent density (Supplementary Figure 31b) and decreased electrochemical impedance in the Nyquist plots (Supplementary Figure 31c). It is noteworthy that the significantly shortened life-time of PL (Supplementary Figure 31d) could be attributed to the generated deeply trapped sites, which have been proved to facilitate the ORR process[43,44].

To further investigate whether the deeply trapped sites in Sb-SAPC15 could facilitate both ORR and OER, time-resolved infrared absorption (TR-IR) spectroscopy was performed to monitor the charge carrier dynamics and the reativities of Sb-SAPC15 for ORR and WOR in microsecond time-scale[43,45]. To probe the charge transfer dynamics from electron to $O_2$ and hole to $H_2O$, the decay kinetics of deeply trapped electrons (at 5000 $cm^{-1}$) of PCN, PCN_Na15 and Sb-SAPC15 were investigated (Supplementary Figure 32,

**Commented [TB25]:** Subheadings must be no longer than 60 characters including spaces and should not contain punctuation.
Perhaps shorten this to "Properties of Sb-SAPC and photocatalytic mechanism" or similar

**Commented [TB26R25]:** We have changed the subtitle to "Properties of Sb-SAPC and photocatalytic mechanism"

Figure 3a) and compared under $N_2$, $O_2$ and $H_2O$ atmosphere (Figure 3b). The decay of the deeply trapped electrons at 5000 $cm^{-1}$ on pristine PCN accelerated very slightly (Figure 3b) in $O_2$ as compared to that in $N_2$ ($I_{O2}/I_{N2}$ = 0.83). The decay on PCN_Na15 showed a little acceleration in $O_2$ than that in $N_2$ ($I_{O2}/I_{N2}$ = 0.66), indicating that introduction of Na could generate reactive sites for charge transfer of trapped electrons to $O_2$[43,44]. When Sb was introduced into the catalyst, we observed significant decay of the deeply trapped electrons on Sb-SAPC15 in $O_2$ as compared to that in $N_2$ ($I_{O2}/I_{N2}$ = 0.46). This indicates that the reactant $O_2$ would preferentially react with the deeply trapped electrons that were induced by the Sb sites. In the case of holes, the decay on pristine PCN and PCN_Na15 changed very little in $H_2O$ environment compared to that in $N_2$ ($I_{H2O}/I_{N2}$ = 0.86 for PCN and $I_{H2O}/I_{N2}$ = 1.09 for PCN_Na15), indicating that the photogenerated holes barely transferred to $H_2O$. On the contrary, the decay on Sb-SAPC15 was significantly retarded in $H_2O$ as compared to that in $N_2$ ($I_{H2O}/I_{N2}$ = 1.92), suggesting that the photogenerated holes could readily transfer to $H_2O$ molecules: hole-consuming reaction by $H_2O$ reduced the number of surviving holes in the catalyst and hence elongated the lifetime of electrons[45]. Additionally, an isotopic experiment (Supplementary Figure 33) to simulate the real system (without $Ag^+$ or $NaIO_3$) was conducted to verify the as-proposed mechanism of WOR by utilizing $^{16}O_2$ (as an electron acceptor) and $H_2{}^{18}O$ (as an electron donor). As shown in Supplementary Figure 32b, the signal of $^{18}O_2$ (m/z = 36) could be detected after photocatalytic reaction for 1 h, indicating that the oxygen evolution reaction indeed occurred in the real reaction system. It is important to note that this signal could not be detected in absence of Sb-SAPC15 or light irradiation, indicating that the photogenerated holes participated in the WOR to generate $^{18}O_2$. The highly active holes for OER could also be confirmed by rotating ring disk electrode measurements (Supplementary Figure 34). A clear signal of $O_2$ reduction to $H_2O$ was detected by the ring disk, verifying $O_2$ generation on the Sb-SAPC surface via WOR. These results confirm that the deeply trapped electrons and the corresponding holes in Sb-SAPC15 are the major contributors for the ORR and OER process (Supplementary note 7), respectively, leading to a significantly promoted photocatalytic activity of $H_2O_2$ production.

The density functional theory (DFT) calculation also shows how the Sb and Na species

promote the inner and inter layer charge transfer in Sb-SAPC (Supplementary Figures 35-36). Four periodic models including graphitic carbon nitride (GCN), sodium incorporated graphitic carbon nitride (Na-GCN), antimony incorporated graphitic carbon nitride (Sb-GCN), and sodium and antimony co-incorporated graphitic carbon nitride (NaSb-GCN) were optimized, and the Bader charges of each layer in different models are presented in Supplementary Figure 35[43,46]. The Bader charge difference between each adjacent layers of pristine GCN is extremely small (|Δq| ~ 0.004 e), suggesting very weak adiabatic coupling between interlayers in GCN[45,46], leading to poor interlayer charge transfer. Both Na-GCN and Sb-GCN display a relatively large number of electrons accumulation on the 2$^{nd}$ and 4$^{th}$ layer (~0.1 e of layer charge)[46,47]. As a result, the Na-GCN and Sb-GCN exhibit a high value of charge difference between the adjacent layers (|Δq| ~ 0.3 e), indicating that the adiabatic coupling has been significantly boosted by introducing Na or Sb. The co-presence of Na and Sb atoms makes the electron distribution more balanced between the layers (Supplementary Figure 35l). In other words, when both Na and Sb are present in the carbon nitride structure, the Na-induced and Sb-induced electron density polarization can be counterbalanced to lower the |Δq| (~0.05 e) and at the same time the distance for adiabatic coupling is significantly increased (|Δq| between the 1$^{st}$ and 2$^{nd}$ layer and between the 3$^{rd}$ and 4$^{th}$ layer are significantly increased). This implies that the charge transfer between the interlayers in carbon nitride incorporated with Sb and Na atoms is more facilitated than that in pristine GCN[46,47]. The deformation charge density near surface of NaSb-GCN (Supplementary Figure 36) reveals a clear pathway from Na to Sb. The Sb on the surface of GCN with weak interlayer bridging shows a larger number of electron accumulation on the first layer (–0.0395 e of layer charge) than the second layer (0.1345 e of layer charge)[46-50]. Note that a clear electron accumulation region and an electron depletion region respectively locate at the 1$^{st}$ and 2$^{nd}$ layer while the pristine CN layer (the 3$^{rd}$ layer) can hardly be polarized, indicating that the inner layer charge transfer is significantly improved with incorporation of Sb and Na species[48-50]. These results show that the electron transfer can be significantly promoted by the incorporation of Sb and Na species in GCN, which can explain the higher photocatalytic activities of Sb-SAPC15.

The excited properties of Sb-SAPC were further studied by Time Dependent DFT

(TDDFT) to understand the correlation between structure and photocatalytic activity using a mono-layer cluster model[51,52]. The possible simulated excited states (ES) that contributed to photocatalytic $H_2O_2$ production (corresponding to the spectra from 420 nm to 470 nm) were confirmed by comparing the action spectra (Figure 1c, Supplementary note 6) with the simulated ones (Supplementary Figure 37a-c). Based on the action spectra and the photocatalytic $H_2O_2$ production activities, the ES1-16 of Melem_3, the ES 1-15 of Melem_3Na+ and the ES 1-26 of Melem_3Sb3+ are highlighted in the distribution heatmap of photogenerated electrons and holes (Supplementary Figure 37d-i)[53]. On the one hand, most of electrons are accumulated at the Sb sites (ES 1-26, Supplementary Table 5), a ligand-to-metal charge transfer from neighboring melem units to Sb, in Melem_3Sb3+ with high density (~20-80%), while most of states (ES 1-16 for Melem_3, Supplementary Table 6; ES 1-15 for Melem_3Na+, Supplementary Table 7) show averagely distributed electrons at the C sites (< 10%) in Melem_3 and Melem_3Na+[51-53]. Note that the photogenerated electrons and holes barely locate at the Na atoms, indicating that the coordinated Na species on the catalyst's surface could not serve as the active sites for the photocatalytic reaction. Additionally, a comprehensive investigation of charge separation and delocalization of holes and electrons were conducted by utiling Melem_6, Melem_6Na+ and Melem_6Sb3+ as models (Supplementary Figure 38-40, Suplementary note 7). The significantly improved separation of electron-hole pairs and highly concentrated elelctron/holes may effectively promote both photocatalytic ORR and WOR in Sb-SAPC15 by introducing atomic Sb sites.

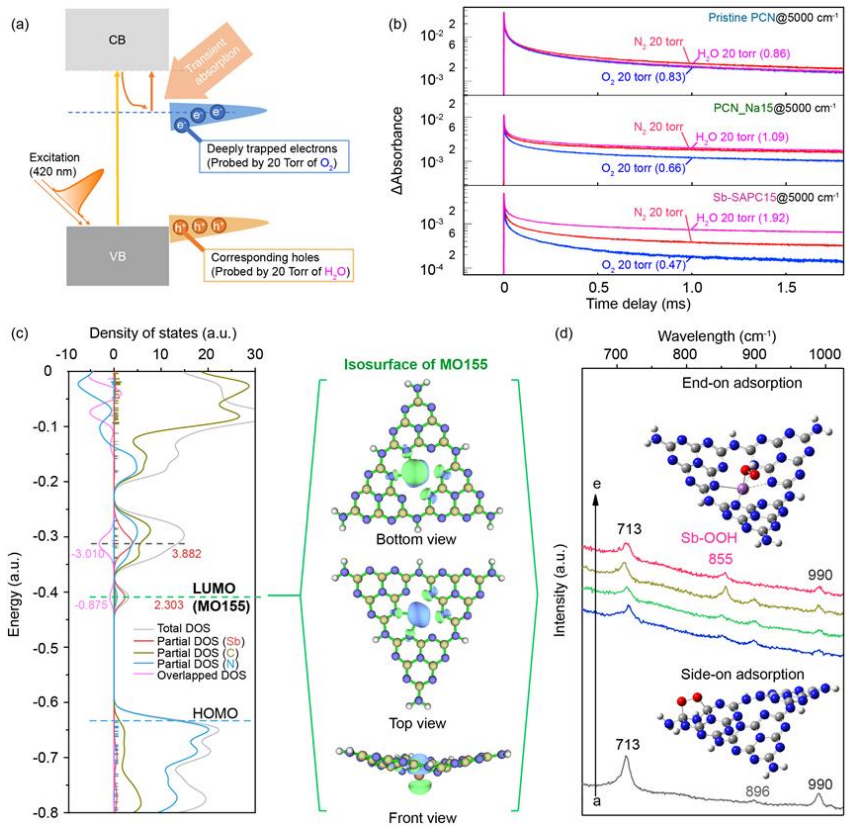


**Figure 3 | Excitation properties and OER/ORR reactivities of Sb-SAPC15. a**, The systematic diagram of transition absorption after excitation as the probe for OER/ORR (details for the pulse light: 420 nm, 6 ns, 5 mJ and 0.2 Hz). **b**, The comparison of transient absorption decay among PCN, PCN_Na15 and Sb-SAPC15 at 5000 $cm^{-1}$ under $N_2$, $O_2$ and $H_2O$ atmosphere (20 Torr). The absorption intensities at the time point of 1 ms was used as the benchmark for investigating how deeply trapped electrons/holes interact with $O_2$/$H_2O$. **c**, Total density of states (TDOS), partial density of states (PDOS) and overlapped density of states (ODOS) of Melem_3Sb3+ conbined with the isosurface of LUMO (Isovalue is 0.05). **d**, Experimental Raman spectra recorded during photoreaction in a 2-propanol aqueous solution with saturated oxygen. Spectrum a, b, c and d: PCN, Sb-SAPC1, Sb-SAPC5 and Sb-SAPC15 in 10% (v/v) 2-propanol aqueous solution. Spectrum e: Sb-SAPC15 in pure water.

The influence of Sb single atoms on the photo-redox reactions was further studied by

analyzing the contributions of MOs to holes and electrons from ES1 to ES26 of Melem_3Sb3+ (Supplementary Table 5). Several MOs with energetic levels equal to or lower than HOMO all contribute to holes (ranging from 0% to ~60%), while almost of electrons are contributed by LUMO (MO155) in most of transitions. This observation implies that the electronic configuration of LUMO can almost represent the photogenerated electronic configuration. The result from partial DOS (PDOS) of Melem_3Sb3+ shows that a new molecular orbital (MO) mainly contributed by electrons from Sb forms the LUMO. It is important to note that this MO exhibits a slightly lower energetic level than the MO contributed by C and N, which is in accordance with the slightly shifted CBM of Sb-SAPC15[22]. Combined with the simulated results of charge separation, iso-surface of LUMO of Melem_3Sb3+ reveals that most of the electrons (>75%) are concentrated at the single Sb sites with ideal electronic configuration for adsorption of electrophilic oxygen (Figure 3c). To study the ORR mechanism on Sb-SAPC, rotating disk electrode (RDE) analysis was performed to investigate the number of electrons (n) transferred in the ORR process (Supplementary Figure 41). The estimated "n" value is close to 2 for Sb-SAPC15 in both dark and light irradiation conditions. The preferred $2e^-$ ORR pathway on Sb-SAPC can be further supported by DFT calculation using the computational hydrogen electrode (CHE) method. As shown in Supplementary Figure 42a, the calculated $\Delta G_{*OOH}$ is 4.53 eV (U = 0 V versus the reversible hydrogen electrode [RHE]), which is smaller than 4.59 eV of $\Delta G_{*O}$, a crucial intermediate in $4e^-$ ORR[36]. The large energetic barrier toward forming *O would suppress the $4e^-$ ORR process. For a $2e^-$ ORR catalyst, the adsorption energy of *OOH should be larger than the thermoneutral value at the equilibrium potential (U = 0.7 V vs. RHE), corresponding to $\Delta G_{*OOH}$ of 3.52 eV. The calculated $\Delta G_{*OOH}$ is 3.83 eV (U = 0.7 V vs. RHE), suggesting that the ORR on single atom Sb may follow a $2e^-$ pathway (Supplementary Figure 42b). It can be seen that the difference between *OH and *O is as high as 3.742 eV, indicating that a considerably large energetic barrier needs to be overcome for the $4e^-$ OER process. In this case, the Sb site should not function as an effective site to catalyze $4e^-$ OER. It is noteworthy that the calculated $\Delta G_{*H}$ on Sb-SAPC15 is significantly larger (0.937 eV) than that on Pt (111) (Supplementary Figure 43), suggesting that HER on Sb-SAPC15 is energitically unfavorable, matching well with the

experimental result (Figure 1e).

To identify the intermediate in the photocatalytic process, Raman spectroscopy measurements (Figure 3d) were performed under *operando* condition. For PCN, after reaction with 2-propanol as an electron donor under visible light irradiation, a new band appears at 896 $cm^{-1}$, which can be assigned to the C−O vibration and O−O stretching on the melem[12]. While for Sb-SAPCs, a new absorption band at 855 $cm^{-1}$ increases with Sb content in the sample, which can be assigned to the O-O stretching mode of a Sb-OOH species with end-on adsorption configuration[54,55]. This relative chemical shift between $O_2$ end-on/side-on adsorption configuration has been also confirmed by DFT calculations (Supplementary Figure 44, Supplementary note 8). It is noteworthy that Sb-OOH exists even without addition of electron donor, implying that formation of Sb-OOH, rather than the side-on configuration, dominates in the photocatalytic process on Sb-SAPCs. The end-on adsorption shall significantly suppress the $4e^-$ ORR, leading to a high selectivity of the $2e^-$ process[29,30]. Additionally, electron spin resonance (ESR) signal of 5,5-Dimethyl-1-pyrroline N-oxide-$\cdot O_2^-$ (DMPO-$\cdot O_2^-$) could be hardly observed in the Sb-SAPC system (Supplementary Figure 45). Since $\cdot O_2^-$ is an important intermediate in the stepwise $1e^-$ pathway (Equation 6) during formation of 1-4 endoperoxide, the invisible signal of DMPO-$\cdot O_2^-$ in the Sb-SAPC system demonstrates rapid reduction of $O_2$ on Sb-SAPC to generate $H_2O_2$ via a $2e^-$ ORR pathway[22,23,55].

$$O_2+H^++e^-\rightarrow\bullet OOH\ (-0.046\ V\ vs.\ NHE) \quad (6)$$

**Commented [TB27]:** * Please do not refer to parts of figures ('top', 'middle', 'left', etc.) in the text.

**Commented [TB28R27]:** According to the editor's suggestion, we have removed the word "left".

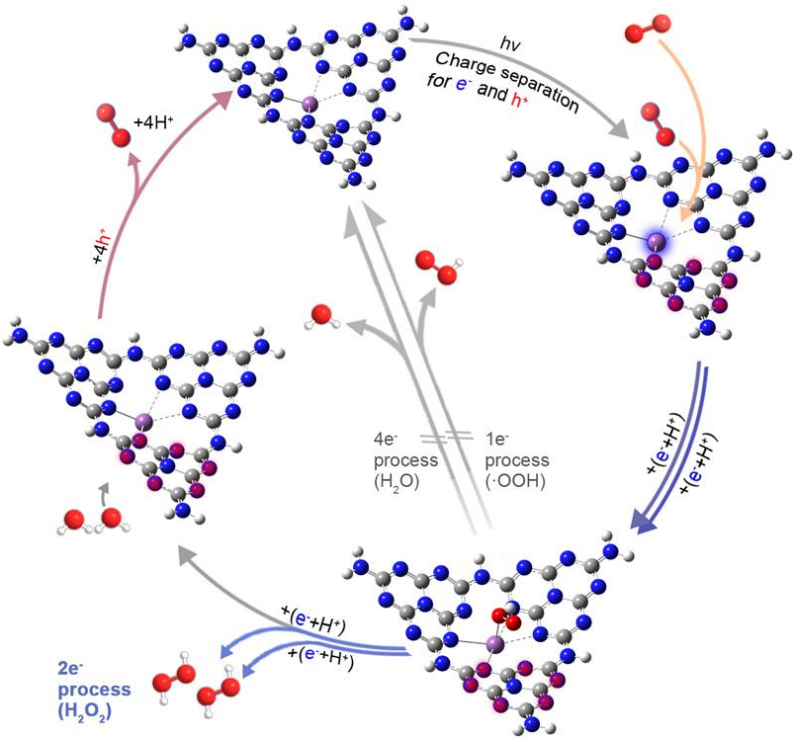


**Figure 4 | Mechanism of photocatalytic $H_2O_2$ production. (The white, gray, bule, red and magenta spheres refer to hydrogen, carbon, nitrogen, oxygen and Sb atoms).** After shining visible light, the photogenerated electrons are localized at the Sb sites (with blue glow), while the photogenerated holes are localized at the N atoms at the melem units (with red glow). Subsequently, the dissolved $O_2$ molecules are adsorbed (orange arrows) onto the Sb sites and then get reduced (blue arrows) via a $2e^-$ transfer pathway through forming an electron μ-peroxide as the intermediate. Simultaneously, water molecules are oxidized (pink arrows) to generate $O_2$ by the highly concentrated holes on the melem units.

Based on the above characterizations and analyses, the reaction mechanism (Figure 4) of Sb-SAPC for photocatalytic $H_2O_2$ production is proposed as follows: Firstly, efficient charge separation occurred on Sb-SAPC under visible light irradiation, generating photoexcited electrons and holes for ORR and WOR, respectively. Then, water molecules were oxidized to evolve $O_2$ by photogenerated holes localized at the N atoms near the single Sb atoms. Simultaenously, $O_2$ dissolved in water and generated from the WOR both

**Commented [TB29]:** * In addition to the title, Figures should also have a brief caption describing the figure. Ideally figures should be understandable without reference to the main text. Please provide this. The color legend must be placed in the caption.

**Commented [TB30R29]:** We have provided a brief caption describing the figure. The color legend has been placed in the caption.

**Commented [TB31]:** * In keeping with our style, please do not use numbered or bulleted lists.

**Commented [TB32R31]:** We removed the numbered lists. Instead, some conjunctions are used for discribing the process.

participated in the ORR process to produce $H_2O_2$. It is worthy noting that the efficient charge separation, ideal single atomic sites for end-on type $O_2$ adsorption and close spatial distribution of active sites boost both the $2e^-$ ORR and $4e^-$ WOR for efficient $H_2O_2$ production.

## Conclusions

In summary, we have reported a well-defined, highly active, selective, and photochemically robust single Sb atom photocatalyst for non-sacrificial $H_2O_2$ production in a water and oxygen mixture under visible light irradiation. The single Sb sites are able to accumulate electrons, which act as the photo-reduction sites for $O_2$ via a $2e^-$ ORR pathway. Simultaneously, the accumulated holes at the N atoms of the melem units neighboring to the Sb sites accelerate the water oxidation kinetics. The collaborative effect between the single atom sites and the support shall open up a vista for designing various single atom catalysts for a variety of photocatalytic reactions in energy conversion and environmental remediation.

## Methods

### Preparation of photocatalysts

Unless otherwise stated, the purities of all reagents for photocatalysts preparation and for photoelectrochemical measurements are above the analytical grade. The pristine PCN and PCN_Na15 were prepared according to the reported methods[19]. The Sb-SAPCs were prepared by a bottom-up method as follows: a certain amount of $NaSbF_6$ (HuNan HuaJing Powdery Material Co., LTD, 0.5 mmol, 1 mmol, 3 mmol, 5 mmol, 10 mmol, 15 mmol and 20 mmol) was dissolved in 30 mL ethanol under sonication for 60 min at 60 °C, followed by adding 4 g melamine (Wako Pure Chemical Industries, Ltd.). The solvent in the solution was removed by combination of rotatory evaporator and vacuum oven. The as-obtained white powder was transferred into a tube furnace. To ensure that oxygen was not present during thermal treatment, the tube furnace was firstly vacuumed to <1 Torr before switching on the $N_2$ gas flow. This process was repeated 3 times, and then 50 mL $min^{-1}$ $N_2$ gas flow was maintained for 30 min before heat treatment. During the synthesis process (including

**Commented [TB33]:** * We avoid the use of phrases such as 'novel', 'for the first time', 'unprecedented', etc. The novelty should be clear from the context.
Please rephrase

**Commented [TB34R33]:** We believe the novelty has been presented already by proposing the collaborative effects between the single atom sites and supports. Therefore, we have change the word "new direction" to "vista".

**Commented [TB35]:** We have chaged the phrase "Experimental section " into "Methods".

**Commented [TB36R35]:** This section subheading has been shortened to be no longer than 60 characters (including spaces).

**Commented [TB37]:** Please remove this part.
the Methods section can be up to 3000 words, so please incorporate as much of the Supplementary Information into the main paper as possible.

**Commented [TB38R37]:** We have incorporated as much of the Supplementary Information into the main paper as possible.

heating and cooling), the system was pressurized by $N_2$ flow so that oxygen could hardly influence the synthesis. The temperature of the furnace was increased from 25 °C to 560 °C at a ramp rate of 2 °C $min^{-1}$ in $N_2$ atmosphere then kept at 560 °C for 4 h. After heat treatment, the furnace was cooled down naturally to 25 °C lasting for at least 8 h with continuous $N_2$ flowing.

**Photocatalytic reaction toward $H_2O_2$ production**

100 mg of photocatalyst was added to 50 mL of deionized water in a borosilicate glass bottle (φ: 60 mm; capacity: 100 mL), and the bottle was sealed with a rubber septum cap. The catalyst was dispersed by ultrasonication for 15 min, and $O_2$ was bubbled through the solution for 30 min. The bottle was kept in a temperature-controlled air bath at 25 ± 0.5 °C with wind flow and was irradiated at λ > 420 nm using a 300 W Xe lamp (PXE-500, USHIO Inc.) under magnetic stirring. To study the WOR, 50 mg of photocatalyst was added into $NaIO_3$ (0.1 M, 50 mL) solution in a borosilicate glass bottle (φ: 60 mm; capacity: 100 mL). After completely removing $O_2$ from the reaction system, the bottle was irradiated by a 300 W Xenon Lamp. The light intensity of visible light and infrared-red light ($I_{>400}$) after passing a UV cut filter (λ > 400 nm) was firstly measured. Then, a glass filter with λ > 500 nm was used to replace the UV cut filter for measuring the light intensity ($I_{>500}$). The difference between $I_{>400}$ and $I_{>500}$ was used to calibrate the total light intensity. After a certain time interval, the gas was extracted from the bottle and examined by gas chromatography equipped with a TCD detector. To examine the $H_2O_2$ production from $O_2$ generated by WOR, a certain amount of photocatalyst (Sb-SAPC15: 200 mg, 100 mg and 50 mg; Pristine PCN: 200 mg) was added into 50 mL of $NaNO_3$ solution (pH = 7) with $AgNO_3$ (0.1 mM). 1.5 mL of solution was extracted every hour to acquire the time-dependent $H_2O_2$ production without the initial introduction of $O_2$. The amount of $H_2O_2$ in these experiments was determined by a colorimetric method using PACKTEST (WAK-$H_2O_2$, KYORITSU CHEMICAL-CHECK Lab., Corp.) equipped with a digital PACKTEST spectrometer (ED723, GL Sciences Inc.).

**Apparent quantum efficiency analysis**

The photocatalytic reaction was carried out in pure deionized water (30 mL) with photocatalyst (60 mg) with or without addition of ethanol as an electron donor in a borosilicate glass bottle. After ultrasonication and $O_2$ bubbling, the bottle was irradiated by an Xe lamp for 4 h with magnetic stirring. The incident light was monochromated by band-pass glass filters (Asahi Techno Glass Co.), where the full-width at half-maximum of the light is 11−16 nm. The number of photons that enter the reaction vessel was determined by a 3684 optical power meter (HIOKI E.E. CORPORATION).

**Determination of solar-to-chemical conversion efficiency**

Solar-to-chemical conversion efficiency was determined by a PEC-L01 solar simulator (Peccell Technologies, Inc.). The photoreaction was performed in pure deionized water (100 mL) with photocatalyst (500 mg) under $O_2$ atmosphere (1 atm) in a borosilicate glass bottle. A UV cut filter (λ > 420 nm) was used to avoid decomposition of the formed $H_2O_2$ by absorbing UV light[12,16,23]. The irradiance of the solar simulator was adjusted to the AM1.5 global spectrum[12,16,23]. The solar-to-chemical conversion efficiency ($\eta$) was calculated by the following equation:

$$\eta(\%) = \frac{\Delta G_{H_2O_2} \times n_{H_2O_2}}{t_{ir} \times S_{ir} \times I_{AM}} \times 100\%. \quad (6)$$

where $\Delta G_{H_2O_2}$ is the free energy for $H_2O_2$ generation (117 kJ mol$^{-1}$). $n_{H_2O_2}$ is the amount of $H_2O_2$ generated, and $t_{ir}$ is the irradiation time (s). The overall irradiation intensity ($I_{AM}$) of the AM1.5 global spectrum (300−2500 nm) is 1000 W m$^{-2}$, and the irradiation area ($S_{ir}$) is 3.14 × 10$^{-4}$ m$^2$.

**Commented [TB39]:** Please name this section as "Methods"

**Commented [TB40R39]:** We have added the number of the equation presented here.

**Instruments**

High-resolution transmission electron microscopy, high-angle annular dark field scanning transmission electron microscopy, selected area electron diffraction and energy-dispersive X-ray spectroscopy were performed on a Titan Cubed Themis G2 300 electron microscope with an accelerating voltage of 300 kV. Electron energy loss spectroscopy was conducted using a Quantum ER/965 P detector. The crystalline phases were characterized by a powder X−ray diffraction instrument (MiniFlex II, Rigaku Co.) with CuKα (λ = 1.5418

Å) radiation (cathode voltage: 30 kV, current: 15 mA). Absorption properties of the powder samples were determined using the diffuse reflection method on a UV/VIS/NIR spectrometer (UV-2600, Shimadzu Co.) attached to an integral sphere at room temperature. X−ray photoelectron spectroscopy measurements were performed on a Kratos AXIS Nova spectrometer (Shimazu Co., Japan) with a monochromatic Al Kα X−ray source. The binding energy was calibrated by taking the carbon (C) 1s peak of adventitious carbon at 284.6 eV. Valence band X-ray photoelectron spectroscopy was performed on an ESCALAB 250Xi (Thermo Scientific, USA). The equilibration of Fermi level of the instrument was performed by measuring the VB-XPS of Au metal basis as the reference. The Fermi level of the instrument was equilibrated at 4.5 eV. In this case, the numerical value of the binding energy in the calibrated VB-XPS spectrum is the same as the potential vs. standard hydrogen electrode. Electron spin resonance signals of spin-trapped paramagnetic species with 5,5-diemthyl-1-pyrroline N-oxide (DMPO, methanol solution) were recorded with an A300-10/12 spectrometer. Photoluminescence spectroscopy was performed on a FP-8500 spectrofluorometer (JASCO Corporation, Japan). The temperature for the photoluminescence measurements was about 25 °C controlled by an air conditioner, which worked 24/7. Time-dependent photoluminescence spectroscopy was conducted on a FS5 fluorescence spectrometer (Edinburgh Instruments Ltd., UK). Raman spectra was performed on a Laser Microscopic Confocal Raman Spectrometer (Renishaw inVia, UK) at 785 nm. The pH value of the solution was measured by a pH meter (HORIBA pH meter D-51, HORIBA, Ltd.).

The X-ray absorption spectroscopy for Sb K-edge was measured at beamline BL01C at the National Synchrotron Radiation Research Center (NSRRC, Hsinchu, Taiwan). The data analysis for the X-ray absorption spectroscopy using IFEFFIT was conducted by Demeter system.

**Photoelectrochemical characterizations**

Photoelectrochemical (PEC) characterizations were conducted on a conventional three-electrode potentiostat setup connected to an electrochemical analyzer (Model 604D, CH Instruments, Inc.). The fluorine-doped tin oxide (FTO) glass of 1 cm × 2 cm in size was

covered with photocatalyst that was achieved by first mixing a catalyst (100 mg) with ethyl cellulose binder (10 mg) in ethanol (6 mL) for one hour and then depositing the final viscous mixture by a doctor blade method followed by drying at room temperature and further drying at 40 °C overnight in a vacuum oven. The area of the photoelectrode was controlled to be 1 $cm^2$. The PEC system consisted of an FTO glass covered by the photocatalyst, a coiled Pt wire and a saturated Ag/AgCl/KCl (saturated) electrode as the working, counter, and reference electrode, respectively. The photocurrent was collected at 0.8 V vs. NHE (0.6 V vs. Ag/AgCl) in a phosphate buffer solution (PBS, pH = 7.4). The solution was saturated with $O_2$ by bubbling $O_2$ for 15 min (0.5 L $min^{-1}$)[12,56,57]. Electrochemical impedance spectroscopy (EIS) analysis was performed at a DC voltage of -0.6 V vs. Ag/AgCl with an AC voltage amplitude of 5 mV in a frequency range from 100 kHz to 0.01 Hz. For the Mott-Schottky measurements, similar strategy was performed on FTO glass (1.5 cm × 3 cm) by the same doctor blade method. The area of the electrode for the Mott-Schottky measurements was controlled to be 0.50 $cm^2$. Mott-Schottky measurements were performed at a potential range from 0.2 V to -0.6 V *vs*. NHE, with an AC voltage amplitude of 5 mV, and in a frequency range from 25 Hz to 500 Hz. Each increase of potential is 0.05 V. The quiet time for each test is 2 s.

**Isotopic experiments with $^{18}O_2$ and $H_2{}^{16}O$**

Firstly, 60 mg of Sb-SAPC15 was dispersed in 30 ml of $H_2{}^{16}O$ via sonication for 15 min. Subsequently, 10 mL of $^{18}O_2$ gas (≥ 98% $^{18}O$; TAIYO NIPPON SANSO Corporation) was injected to the suspension. Then, the system was completely sealed and irradiated by visible light. After a certain time interval (6 h, 24 h, and 72 h), 1 mL suspension was extracted and injected into a glass test tube filled with $N_2$ and 0.1 g $Fe_2(SO_4)_3$ dissolved in 1 mL $H_2SO_4$. After injection of suspension, the test tube was sealed and irradiated under UV light for 5 h. The gas (0.1 mL) in the test tube was extracted by gas chromatography syringe and injected into a Shimadzu GC-MS system (GCMS-QP2010).

**Isotopic experiments with $H_2{}^{18}O$**

20 mg of Sb-SAPC15 was dispersed in 10 g of $H_2{}^{18}O$ (≥ 98% $^{18}O$; TAIYO NIPPON

SANSO Corporation) containing 1 mM $AgNO_3$ under sonication for 15 min. Afterwards, $N_2$ was bubbled into the suspension for 2 h at a flow rate of 0.5 L $min^{-1}$ to ensure complete removal of the dissolved oxygen ($^{16}O_2$) in the system[16]. Then, the system was completely sealed and irradiated by visible light. After a certain time interval (0.5 h, 1 h, 3 h, 5 h, 10 h and 24 h), 1 mL suspension was extracted and injected into a glass test tube filled with $N_2$ and 0.1 g $Fe_2(SO_4)_3$ dissolved in 1 mL $H_2SO_4$. After injection of suspension, the test tube was sealed and irradiated under UV light for 5 h. The gas (0.1 mL) in the test tube was extracted by gas chromatography syringe and injected into a Shimadzu GC-MS system (GCMS-QP2010).

**Isotopic experiments in real experimental conditions**

A poly tetra fluoroethylene gas bag was used for the isotopic experiment. First of all, 3 mL ultrapure $N_2$ was injected into the bag, followed by injecting 1 mL aqueous suspension of Sb-SAPC15 (concentration: 1 mg $mL^{-1}$; 1 mg Sb-SAPC15 powder dissolved in 1 mL $H_2{}^{18}O$). Subsequently, 100 μL $O_2$ gas was injected and the bag was properly sealed and put over an ultrasonicator. Additionally, control experiments in absence of Sb-SAPC15 or light irradiation were conducted for confirming the photo-induced oxygen generation reaction. Furthermore, GC-MS spectra of the gas extracted from the Sb-SAPC15 system with other electron acceptors (0.1 M $Ag^+$ or 0.1 M $NaIO_3$) or without addition of Sb-SAPC were also conducted for comparison.

**$H_2O_2$ degradation study**

50 mL of deionized water in a borosilicate glass bottle (φ: 60 mm; capacity: 100 mL) without addition of catalyst was bubbled with $O_2$ for 30 min. Then, a certain amount of $H_2O_2$ was added into the bottle, and the concentration of $H_2O_2$ was manipulated to be 1 $\times 10^2$ mg $L^{-1}$. Finally, the bottle was sealed with a rubber septum cap. To investigate the hole transfer to $H_2O_2$, the following experiment was performed: 50 mg of photocatalyst was added into 50 mL $NaIO_3$ (0.1 M) and $H_2O_2$ (0.01wt.%) solution in a borosilicate glass bottle (φ: 60 mm; capacity: 100 mL). The same solution without addition of photocatalyst was also measured as a control. Additionally, the same experiment was also conducted in 50 mL $NaIO_3$ (0.1

**Commented [TB41]:** Subheadings must be no longer than 60 characters including spaces and should not contain punctuation.

**Commented [TB42R41]:** This section subheading has been shortened to be no longer than 60 characters (including spaces).

M) phosphate buffer solution (0.1 M, pH = 7.4). After completely removing $O_2$ from the reaction system, the bottle was irradiated by a 300 W Xenon lamp with a UV cut filter (light intensity: 30.3 W $m^{-2}$ at 420-500 nm).

**Details for TD-DFT calculations**

The optimization and frequency combined with the vertical excitation properties were performed via time-dependent density functional theory (TD-DFT) in the Gaussian 09 program S2, which was carried out by utilizing wb97xd/6-311g(d) level of theory for C, N and H elements and SDD for Sb element. 3 monolayer cluster models were optimized to represent the major surface properties of CN sites in PCN, Na sites in PCN_Na15 and Sb sites in Sb-SAPC15[50,58]. The charges of monolayer cluster models were settled in consideration of the oxidation state of Sb and Na based on the experimental results as follows: 0 for Melem_3; +1 for Melem_Na1+; and +3 for Melem_3Sb3+. To give a comprehensive understanding of the relationships between the electronic configuration during excitation and the realistic experiment results. 50 excited states (ES) of these three cluster models have been used to simulate of UV absorption spectra[50]. Note that the absorption edge of simulated UV spectra is usually large than that of experimental ones because of the following two reasons: (1) To simulate the charge-transfer properties of the model with high qualities, function of ω97xd, a function including large amount of Hartree–Fock exchange, were used. These exchange functions usually overestimate the excitation energies, as well as the simulated HOMO-LUMO gap[51,52,58]; (2) In the solid state, p-conjugated molecules adjacent to the one carrying a charge do strongly polarize, an effect that stabilizes the cationic and anionic states (each generally by about one eV in p-conjugated materials). In this case, the band gap is typically considerably smaller in energy than the molecular fundamental gap, as well as the optical gap[52]. Since the evitable system error cannot be eliminated, the possible simulated ES that contributed to $H_2O_2$ production (corresponding to the spectra from 420 nm – 470 nm) was confirmed by comparing the experimental spectra and simulated ones. Then, the transition density of electron/holes were considered at all these ES.

For analysis of the excitation and charge transfer properties, Multiwfn Ver. 3.6 (released

on May 21, 2019)[53] was performed. Visualization of hole, electron and transition density was also performed by Multiwfn; functions of *IOp(9/40 = 3)* were set during the vertical excitation based on TD-DFT calculation[53]. The electron distributions at these ES were presented as heatmaps by combination of GaussView and Multiwfn[53,59-62]. The iso surface of LUMO orbitals were presented by setting the isovalue of 0.05.

**Details for Free energy diagram**

The cluster model is more likely to predict the ORR process based on our previous investigation[36]. The free energy diagram of Melem_3Sb3+ was calculated as follows:

The optimized structure of Melem_3Sb3+ was used as the initial structure for calculating the most stable adsorption configurations of *OOH, *O, and *OH. The ORR following the $2e^-$ and $4e^-$ pathway produces $H_2O$ and $H_2O_2$, respectively. The associative $4e^-$ ORR is composed of four elementary steps (Equation 7-10):

$$* + O_2(g) + H^+ + e^- \rightarrow *OOH \quad (7)$$

$$* OOH + H^+ + e^- \rightarrow O* + H_2O(l) \quad (8)$$

$$O* + H^+ + e^- \rightarrow *OH \quad (9)$$

$$*OH + H^+ + e^- \rightarrow H_2O(l) + * \quad (10)$$

The $2e^-$ ORR comprises of two elementary steps (Equation 11-12):

$$* + O_2(g) + H^+ + e^- \rightarrow *OOH \quad (11)$$

$$*OOH + H^+ + e^- \rightarrow H_2O_2(l) + * \quad (12)$$

The asterisk (*) denotes the active site of the catalyst.

The free energy for each reaction intermediate is defined as:

$$G = E_{DFT} + E_{ZPE} - TS + E_{sol} \quad (13)$$

where $E_{DFT}$ is the electronic energy calculated by DFT, $E_{ZPE}$ denotes the zero point energy estimated within the harmonic approximation, and TS is the entropy at 298.15 K (T = 298.15 K). The $E_{ZPE}$ and TS of gas-phase $H_2$ and reaction intermediates are based on our previous work[36]. For the concerted proton-electron transfer, the free energy of a pair of proton and electron ($H^+ + e^-$) was calculated as a function of applied potential relative to RHE (U versus RHE), i.e., $\mu(H^+)+\mu(e^-) = 1/2\mu(H_2)-eU$, according to the computational hydrogen electrode (CHE) model proposed by Nørskov.[63] In addition, the solvent effect

was reported to play an important role in ORR. In our calculations, the solvent corrections ($E_{sol}$) for *OOH and *OH are 0.45 eV in accordance with previous studies[64,65]. We used the energies of $H_2O$ and $H_2$ molecules calculated by DFT together with experimental formation energy of $H_2O$ (4.92 eV) to construct the free energy diagram. The free energies of $O_2$, *OOH, *O, and *OH at a given potential U relative to RHE are defined as:

$$\Delta G(O_2) = 4.92 - 4eU \tag{14}$$

$$\Delta G(OOH) = G(*OOH) + \frac{3G(H_2)}{2} - G(*) - 2G(H_2O) - 3eU \tag{15}$$

$$\Delta G(O) = G(*O) + G(H_2) - G(*) - G(H_2O) - 2eU \tag{16}$$

$$\Delta G(OH) = G(*OH) + \frac{G(H_2)}{2} - G(*) - G(H_2O) - eU \tag{17}$$

**Details for simulations of charge transfer**

All theoretical calculations were performed based on density functional theory (DFT), implemented in the Vienna ab initio simulation package (VASP)[66,67]. The electron exchange and correlation energy were treated within the generalized gradient approximation in the Perdew-Burke-Ernzerhof functional (GGA-PBE)[68,69]. The valence orbitals were described by plane-wave basis sets with cutoff energies of 400 eV. For the simulation of Na and Sb incorporated in bulk phase of g-$C_3N_4$, a 1 × 1 × 2 supercell of pristine bulk g-$C_3N_4$ was adopted. And the k-points were sampled in a 3 × 3 × 2 Monkhorst-Pack grid. For the simulation of Na and Sb near the surface of g-$C_3N_4$, the k-point sampling was obtained from the Monkhorst-Pack scheme with a (2 × 2 × 1) mesh. The atomic coordinates are fully relaxed using the conjugate gradient method (CG)[70]. The convergence criteria for the electronic self-consistent iteration and force were set to $10^{-4}$ eV and 0.02 eV/Å, respectively. The vacuum gap was set as 15 Å. To quantitatively compare the degree of charge transfer, a Bader charge analysis has been carried out[45].

**Data availbility**

The data that support the findings of this study are available from the corresponding author upon reasonable request. Source data are provided with this paper.

**Commented [TB43]:** Please add a 'Data availability' section at the end of the Methods
This journal strongly supports public availability of all data: we encourage you to make arrangements, wherever possible, to place the data used in your paper into a public data repository. If data can only be shared on request, we ask that you explain why in your Data Availability Statement.

**Commented [TB44R43]:** We have added the "data avaibility part" here. The source data of this paper will be uploaded in sereval separated files.

**Code availability**

The codes that support the findings of this study are available from the corresponding author upon reasonable request.

## References


[1] Bryliakov, K.P. Catalytic asymmetric oxygenations with the environmentally benign oxidants $H_2O_2$ and $O_2$, *Chem. Rev.* **117**, 11406-11459 (2017).

[2] Shaegh, S.A.M., Nguyen, N.-T., Ehteshamiab, S.M.M. & Chan, S.H., A membraneless hydrogen peroxide fuel cell using Prussian Blue as cathode material, *Energy Environ. Sci.* **5**, 8225-8228 (2012).

[3] Gray, H.B. Powering the planet with solar fuel, *Nat. Chem.* **1**, (2009) 7-7.

[4] Kim, D., Sakimoto, K.K., Hong, D. & Yang, P. Artificial photosynthesis for sustainable fuel and chemical production, *Angew. Chem. Int. Ed.* **54**, 3259-3266 (2015).

[5] Xia, C., Xia, Y., Zhu, P., L. Fan & Wang, H. Direct electrosynthesis of pure aqueous $H_2O_2$ solutions up to 20% by weight using a solid electrolyte, *Science* **366**, 226-231 (2019).

[6] Edwards, J.K. *et al.* Direct synthesis of $H_2O_2$ from $H_2$ and $O_2$ over gold, palladium, and gold-palladium catalysts supported on acid-pretreated $TiO_2$, *Angew. Chem. Int. Ed.* **48**, 8512–8515 (2009).

[7] Freakley, S.J. *et al.* Palladium-tin catalysts for the direct synthesis of $H_2O_2$ with high selectivity, *Science* **351**, 965-968 (2016).

[8] Yang, S. *et al.* Toward the decentralized electrochemical production of $H_2O_2$: A focus on the catalysis, *ACS Catal.* **8**, 4064-4081 (2018).

[9] Yi, Y., Wang, L., Li, G. & Guo, H. A review on research progress in the direct synthesis of hydrogen peroxide from hydrogen and oxygen: Noble-metal catalytic method, fuel-cell method and plasma method, *Catal. Sci. Technol.* **6**, 1593-1610 (2016).

[10] Hou, H., Zeng & X. Zhang, X. Production of hydrogen peroxide through photocatalytic process: A critical review of recent advances, *Angew. Chem. Int. Ed.*, (2019).

[11] Shi, X. *et al.* Understanding activity trends in electrochemical water oxidation to form hydrogen peroxide, *Nat. Commun.* **8**, 701 (2017).

[12] Shiraishi, Y. *et al.* Sunlight-driven hydrogen peroxide production from water and molecular oxygen by metal-free photocatalysts, *Angew. Chem.* **126**, 13672-13677 (2014).

[13] Fuku, K. & Sayama, K. Efficient oxidative hydrogen peroxide production and accumulation in photoelectrochemical water splitting using a tungsten trioxide/bismuth vanadate photoanode, *Chem. Commun.* **52**, 5406-5409 (2016).

[14] Baek, J.H. *et al.* Selective and efficient Gd-doped $BiVO_4$ photoanode for two-electron water oxidation to $H_2O_2$, *ACS Energy Lett.* **4**, 720-728 (2019).

[15] Teng, *et al.* Photoexcited single metal atom catalysts for heterogeneous photocatalytic $H_2O_2$ production: Pragmatic guidelines for predicting charge separation, *Appl. Catal. B-Environ.* **282**, 119589 (2020).

[16] Shiraishi, Y. *et al.* Resorcinol–formaldehyde resins as metal-free semiconductor photocatalysts for solar-to-hydrogen peroxide energy conversion, *Nat. Mater.* **18**, 985-993 (2019).

[17] Fan, W. *et al.* Efficient hydrogen peroxide synthesis by metal-free polyterthiophene via


**Commented [TB45]:** All authors should be included in reference lists unless there are more than five, in which case only the first author should be given, followed by 'et al.'.
Authors should be listed last name first, followed by a comma and initials of given names. There should be no spaces between initials. Article titles should be in Roman text and book titles in italics; the first word of the title is capitalized, the title written exactly as it appears in the work cited, ending with a period. Journal names are italicized and abbreviated (with periods) according to common usage. Volume numbers appear in bold. Please correct the format of your references as necessary.
All authors should be included in reference lists unless there are more than five, in which case only the first author should be given, followed by 'et al.'.
Authors should be listed last name first, followed by a comma and initials of given names. There should be no spaces between initials. Article titles should be in Roman text and book titles in italics; the first word of the title is capitalized, the title written exactly as it appears in the work cited, ending with a period. Journal names are italicized and abbreviated (with periods) according to common usage. Volume numbers appear in bold. Please correct the format of your references as necessary.
DOIs are not included.

**Commented [TB46R45]:** We have revised the formats of references by following the editor's suggestion.

photoelectrocatalytic dioxygen reduction, *Energy Environ. Sci.* **13**, 238-245 (2020).

[18] Kim, H., Choi, Y., Hu, S., Choi, W. & Kim, J.-H. Photocatalytic hydrogen peroxide production by anthraquinone-augmented polymeric carbon nitride, *Appl. Catal. B-Environ.* **229**, 121-129 (2018).

[19] Moon, G.-H. *et al.* Eco-friendly photochemical production of $H_2O_2$ through $O_2$ reduction over carbon nitride frameworks incorporated with multiple heteroelements, *ACS Catal.* **7**, 2886-2895 (2017).

[20] Chu, C. *et al.* Spatially separating redox centers on 2D carbon nitride with cobalt single atom for photocatalytic $H_2O_2$ production, *PNAS* **117**, 6376-6382 (2020).

[21] Wei, Z. *et al.* Efficient visible-light-driven selective oxygen reduction to hydrogen peroxide by oxygen-enriched graphitic carbon nitride polymer, *Energy Environ. Sci.* **11**, 2581-2589 (2018).

[22] Kaynan, N., Berke, B.A., Hazut, O. & Yerushalmi, R. Sustainable photocatalytic production of hydrogen peroxide from water and molecular oxygen, *J. Mater. Chem. A* **2**, 13822−13826 (2014).

[23] Teng, Z. *et al.* Bandgap engineering of polymetric carbon nitride copolymerized by 2,5,8-triamino-tri-s-triazine (melem) and barbituric acid for efficient nonsacrificial photocatalytic $H_2O_2$ production. *Appl. Catal. B* **271**, 118917 (2020).

[24] Zeng, X. *et al.* Simultaneously tuning charge separation and oxygen reduction pathway on graphitic carbon nitride by polyethylenimine for boosted photocatalytic hydrogen peroxide production, *ACS Catal.* **10**, 3697–3706 (2020).

[25] Wang, Q. & Domen, K., Particulate photocatalysts for light-driven water splitting: Mechanisms, challenges, and design strategies, *Chem. Rev.* **120**, 919-985 (2020).

[26] Hirakawa, H., Hashimoto, M., Shiraishi, Y. & Hirai, T. Photocatalytic conversion of nitrogen to ammonia with water on surface oxygen vacancies of titanium dioxide photocatalytic conversion of nitrogen to ammonia with water on surface oxygen vacancies of titanium dioxide, *J. Am. Chem. Soc.* **139**, 10929-10936 (2017).

[27] Kulkarni, A., Siahrostami, S., Patel, A. & Nørskov, J.K. Understanding catalytic activity trends in the oxygen reduction reaction, *Chem. Rev.* **118**, 2302-2312 (2018).

[28] Watanabe, E., Ushiyama, H. & Yamashita, K., Theoretical studies on the mechanism of oxygen reduction reaction on clean and O-substituted $Ta_3N_5$(100) surfaces. *Catal. Sci. Technol.* **5**, 2769-2776 (2015).

[29] Choi, C.H. *et al.* Hydrogen peroxide synthesis via enhanced two-electron oxygen reduction pathway on carbon-coated Pt surface. *J. Phys. Chem. C* **118**, 30063-30070 (2014).

[30] Chu, C. *et al.*, Electronic tuning of metal nanoparticles for highly efficient photocatalytic hydrogen peroxide production. *ACS Catal.* **9**, 626−631 (2019).

[31] Pegis, M.L., Wise, C.F., Martin, D.J. & Mayer, J.M. Oxygen reduction by homogeneous molecular catalysts and electrocatalysts. *Chem. Rev.* **118**, 2340-2391 (2018).

[32] Yang, S., Kim, J., Tak, Y.J., Soon, A. & Lee, H. Single-atom catalyst of platinum supported on titanium nitride for selective electrochemical reactions. *Angew. Chem. Int. Ed.* **55**, 2058-2062 (2016).

[33] Montemore, M.M., van Spronsen, M.A., Madix, R.J. & Friend, C.M. $O_2$ activation by metal surfaces: Implications for bonding and reactivity on heterogeneous catalysts. *Chem. Rev.* **118**, 2816-2862 (2018).

[34] Wang, A., Li, J. & Zhang, T. Heterogeneous single-atom catalysis, *Nat. Rev. Chem.* **2**, 65–81

(2018).
[35] Shen, R. *et al.* High-concentration single atomic Pt sites on hollow CuSx for selective $O_2$ reduction to $H_2O_2$ in acid solution, *Chem* **5**, 2099–2110 (2019).
[36] Gao, J. *et al.* Enabling direct $H_2O_2$ production in acidic media through rational design of transition metal single atom catalyst, *Chem* **6**, 1-17 (2020).
[37] Jung, E. *et al.* Atomic-level tuning of Co-C-N catalyst for high performance electrochemical $H_2O_2$ production, *Nat. Mater.* **19**, 436–442 (2020).
[38] Nosaka, Y. & Nosaka, A. Introduction to Photocatalysis: From Basic Science to Applications (Royal Society of Chemistry, 2016).
[39] Inoue, Y. Photocatalytic water splitting by $RuO_2$-loaded metal oxides and nitrides with $d^0$- and $d^{10}$ -related electronic configurations, *Energy Environ. Sci.* **2**, 364-386 (2009).
[40] Li, X. *et al.* Single-atom Pt as co-catalyst for enhanced photocatalytic $H_2$ evolution, *Adv. Mater.* **28**, 2427–2431 (2016).
[41] Naumkin, A.V., Kraut-Vass, A., Gaarenstroom, S.W. & Powell, C.J. NIST X-ray photoelectron spectroscopy database. figshare http://dx.doi.org/10.18434/T4T88K (2012).
[42] Ravel, B. & Newville, M. ATHENA, ARTEMIS, HEPHAESTUS: data analysis for X-ray absorption spectroscopy using IFEFFIT, *J. Synchrotron Radiat.* **12**, 537–541 (2005).
[43] Zhang, P. *et al.* Heteroatom dopants promote two-electron $O_2$ reduction for photocatalytic production of $H_2O_2$ on polymeric carbon nitride, *Angew. Chem. Int. Ed.*, **59**, 16209-16217 (2020).
[44] Kim, S. *et al.* Selective charge transfer to dioxygen on $KPF_6$-modified carbon nitride for photocatalytic synthesis of $H_2O_2$ under visible light, *J Catal.* **357**, 51-58 (2018).
[45] Yamakata, A., Ishibashi, T. & Onishi, H. Water- and oxygen-induced decay kinetics of photogenerated electrons in $TiO_2$ and Pt/$TiO_2$: A time-resolved infrared absorption study, J. Phys. Chem. B **105**, 7258-7262 (2001).
[46] Zhang, P. *et al.* Modified carbon nitride nanozyme as bifunctional glucose oxidase-peroxidase for metal-free bioinspired cascade photocatalysis, *Nat. Commun.* **10**, 940 (2019).
[47] Sanville, E., Kenny, S.D., Smith, R. & Henkelman, G. Improved grid based algorithm for Bader charge allocation. *J. Comput. Chem.* **28**, 899–908 (2001).
[48] Gao, H., Yan, S., Wang, J. & Zou, Z. Ion coordination significantly enhances the photocatalytic activity of graphitic-phase carbon nitride, *Dalton Trans.* **43**, 8178–8183 (2014).
[49] Xiong, T. *et al.* KCl-mediated dual electronic channels in layered g-$C_3N_4$ for enhanced visible light photocatalytic NO removal, *Nanoscale* **10**, 8066–8074 (2018).
[50] Xiong, T., Cen, W., Zhang, Y. & Dong, F. Bridging the g-$C_3N_4$ interlayers for enhanced photocatalysis, *ACS Catal.* **6**, 2462–2472 (2016).
[51] Ghuman, K.K. *et al.* Photoexcited surface frustrated Lewis pairs for heterogeneous photocatalytic $CO_2$ reduction, *J. Am. Chem. Soc.* **138**, 1206-1214 (2016).
[52] Bredas, J.-L. Mind the gap! *Mater. Horiz.*, **1**, 17-19 (2014).
[53] Lu, T. & Chen, F. Multiwfn: A multifunctional wavefunction analyzer, *J. Comput. Chem.* **33**, 580-592 (2012).
[54] Nakamura, R. & Nakato, Y. Primary intermediates of oxygen photoevolution reaction on $TiO_2$ (Rutile) particles, revealed by in situ FTIR absorption and photoluminescence measurements, *J. Am. Chem. Soc.* **126**, 1290-1298 (2004).
[55] Jones, R., Summerville, D. & Basolo, F. Synthetic oxygen carriers related to biological systems,

*Chem. Rev.* **79**, 139-179 (1979).
[56] Li, S. *et al.* Effective photocatalytic $H_2O_2$ production under visible light irradiation at g-$C_3N_4$ modulated by carbon vacancies, *Appl. Catal. B* **190**, 26–35 (2016).
[57] Kofuji, Y. *et al.* Carbon nitride–aromatic diimide–graphene nanohybrids: Metal-free photocatalysts for solar-to-hydrogen peroxide energy conversion with 0.2% efficiency, *J. Am. Chem. Soc.* **138**, 10019-10025 (2016).
[58] Govind, N., Lopata, K., Rousseau, R., Andersen, A. & Kowalski, K. Visible light absorption of N-doped $TiO_2$ rutile using (LR/RT)-TDDFT and active space EOMCCSD calculations. *J. Phys. Chem. Lett.* **2**, 2696-2701 (2011).
[59] Bahers, T.L., Adamo, C. & Ciofini, I. A qualitative index of spatial extent in charge-transfer excitations, *J. Chem. Theory Comput.* **7**, 2498-2506 (2011).
[60] Kraner, S., Scholz, R., Plasser, F., Koerner, C. & Leo, K. Exciton size and binding energy limitations in one-dimensional organic materials, *J. Chem. Phys.* **143**, 244905 (2015).
[61] Kraner, S., Prampolini, O. & Cuniberti, G. Exciton binding energy in molecular triads, *J. Phys. Chem. C* **121**, 17088-17095 (2017).
[62] Kislitsyn, D. *et al.* Spatial mapping of sub-bandgap states induced by local nonstoichiometry in individual lead sulfide nanocrystals, *J. Phys. Chem. Lett.* **5**, 3701-3707 (2014).
[63] Nørskov, J.K. *et al.* Origin of the overpotential for oxygen reduction at a fuel-cell cathode. *J. Phys. Chem. B* **108**, 17886-17892 (2004).
[64] Calle-Vallejo, F., Martı´nez, J.I. & Rossmeisl, J. Density functional studies of functionalized graphitic materials with late transition metals for oxygen reduction reactions. *Phys. Chem. Chem. Phys.* **13**, 15639–15643 (2011).
[65] Xu, H., Cheng, D., Cao, D. & Zeng, X.C. A universal principle for a rational design of single-atom electrocatalysts. *Nat. Catal.* **1**, 339–348 (2018).
[66] Kresse, G. & Furthmüller, J. Efficient iterative schemes for *ab initio* total-energy calculations using a plane-wave basis set, *J. Phys. Rev. B* **54**, 11169–11186 (1996).
[67] Kresse, G. & Furthmüller, J. Efficiency of ab-initio total energy calculations for metals and semiconductors using a plane-wave basis set. *J. Comput. Mater. Sci.* **6**, 15–50 (1996).
[68] Perdew, J.P., Burke K. & Ernzerhof, M. Generalized gradient approximation made simple, *Phys. Rev. Lett.* 77, 3865-3868 (1996).
[69] Blöchl, P.E. Projector augmented-wave method, *Phys. Rev. B* **50**, 17953-17979 (1994).
[70] Press, W.H., Teukolsky, S.A., Vetterling, W.T. & Flannery, B.P. Numerical recipes, (Cambridge University Press, 2007).

## Acknowledgements

The authors acknowledge the financial support of Mitsubishi Chemical Corporation, JSPS Grant-in-Aid for Scientific Research (B, No. 20H02847), Grant-in-Aid for JSPS Fellows (DC2, 20J13064), Project National Natural Science Foundation of China (21805191, 21972094), the Guangdong Basic and Applied Basic Research Foundation (2020A1515010982), Shenzhen Pengcheng Scholar Program, Shenzhen Peacock Plan (KQJSCX20170727100802505, KQTD2016053112042971), the Singapore Ministry of

**Commented [TB47]:** this section together with Author contributions and Competing interests should be placed at the end of the manuscript.

**Commented [TB48R47]:** We have removed these sections at the end of manuscript.

Education Academic Research Fund (AcRF) Tier 1: RG115/17 and RG115/18, and Tier 2: MOE2016-T2-2-004, and Singapore Energy Center (SgEC) M4062755.120. The authors thank Dr. Xiang Huang from Department of Physics, Southern University of Science and Technology for his help in theoretical calculation and Dr. Nan Jian from the Electron Microscope Center of the Shenzhen University for for his help in HRTEM measurement.

**Author Contributions Statement**

Z.T., Q.Z. and T.O. conceptualized the project. T.O., C.S. and B.L. supervised the project. Z.T. synthesized the catalysts, conducted the catalytic tests and the related data processing, and performed materials characterization and analysis with the help of H.Y., Q.Z., Y.-R.L. and S.L. K.K. and A.Y. conducted transient absorption spectroscopy. Z.T., W.Y. and C.W. performed the theoretical study. Z.T., H.Y. and B.L. wrote the manuscript with support from all authors.

**Competing Interests Statement**

The authors declare no competing interests.

**Commented [TB49]:** Competing Interests

**Commented [TB50R49]:** The title of this section has been revised.

**Commented [TB51]:** Please remove "financial", the declarations must be broader as per our policy.

**Commented [TB52R51]:** We have removed the word "financial" by following the suggestion of editor.

Supplementary Information for

# Atomically Dispersed Antimony on Carbon Nitride for the Artificial Photosynthesis of Hydrogen Peroxide

Zhenyuan Teng,[1,7,8] Qitao Zhang,[2,8] Hongbin Yang,[3,8] Kosaku Kato,[4] Wenjuan Yang,[2] Ying-Rui Lu,[5] Sixiao Liu,[6,7] Chengyin Wang,[6,7] Akira Yamakata,[4] Chenliang Su,[2,*] Bin Liu,[3,*] and Teruhisa Ohno[1,7,*]

[1]Department of Applied Chemistry, Faculty of Engineering, Kyushu Institute of Technology, Kitakyushu 804-8550, Japan
[2]International Collaborative Laboratory of 2D Materials for Optoelectronics Science and Technology of Ministry of Education, Institute of Microscale Optoelectronics, Shenzhen University, Shenzhen 518060, China
[3]School of Chemical and Biomedical Engineering, Nanyang Technological University, 62 Nanyang Drive, Singapore 637459, Singapore
[4]Graduate School of Engineering, Toyota Technological Institute, 2-12-1 Hisakata, Tempaku Nagoya 468-8511, Japan
[5]National Synchrotron Radiation Research Center, Hsinchu 30076, Taiwan
[6]College of Chemistry and Chemical Engineering, Yangzhou University, 180 Si-Wang-Ting Road, Yangzhou 225002, China
[7]Joint Laboratory of Yangzhou University, Kyushu Institute of Technology, Yangzhou University, 180 Si-Wang-Ting Road, Yangzhou 225002, China
[8]These authors contributed equally.

ORCID:
Teruhisa Ohno: https://orcid.org/0000-0002-7825-8189
Chenliang Su: https://orcid.org/0000-0002-8453-1938
Bin Liu: https://orcid.org/0000-0002-4685-2052
E-mail address:
Teruhisa Ohno: tohno@che.kyutech.ac.jp
Chenliang Su: chmsuc@nus.edu.sg
Bin Liu: liubin@ntu.edu.sg

**Commented [TB53]:** Please make the title consistent with the one in the Main Manuscript

**Commented [TB54R53]:** We agree with the editor that the revised title is more specific. We have changed the title.

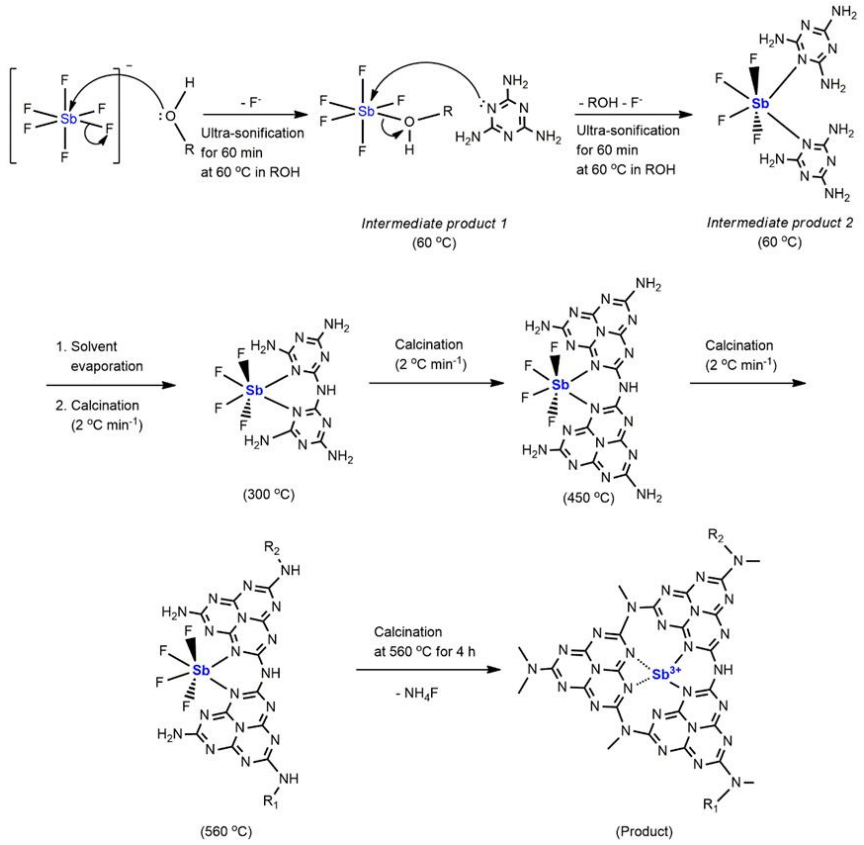


**Supplementary Figure 1. The preparation procedure of the single Sb atom photocatalyst (Sb-SAPC).** Dashed bonds in the product refers to the weak interaction between N and Sb atoms**.**

**Commented [TB55]:** Please change this into a figure.

**Commented [TB56R55]:** We have changed the "scheme" into "figure".

**Commented [TB57]:** Please consider submitting part of the supplementary figures as EXTENDED DATA: Extended Data is an integral part of the paper and only data that directly contribute to the main message should be presented.

**Commented [TB58R57]:** Figure 19,23,27,29,30,31,34,40,44 will be submitted as EXTENDED DATA.

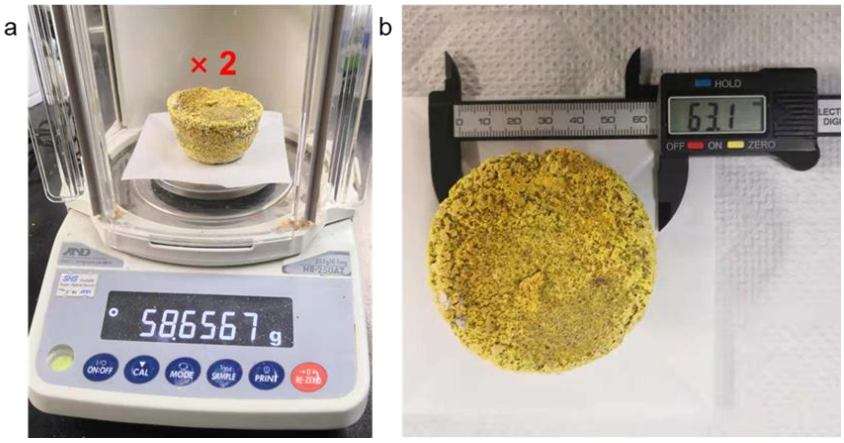


**Supplementary Figure 2 | Digital photographs showing the as-prepared Sb-SAPC15 in one batch.**

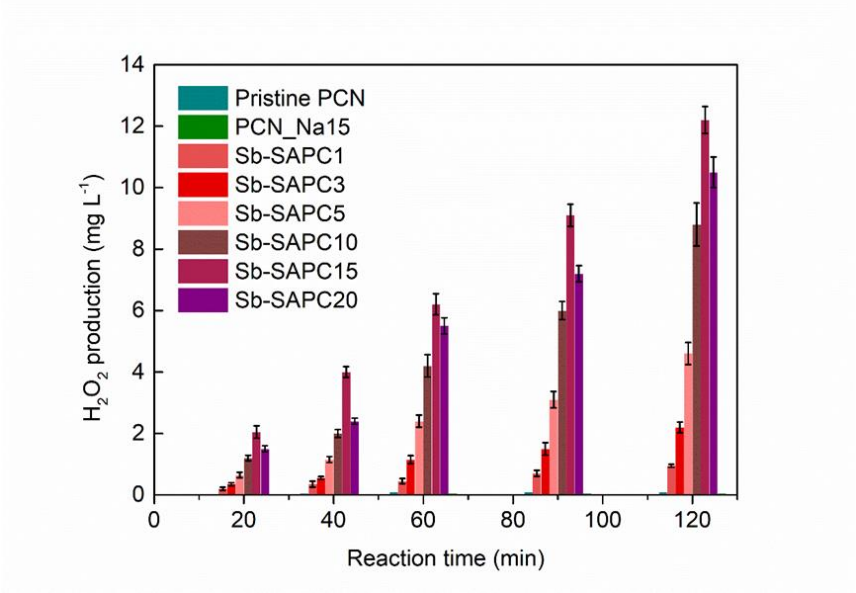


**Supplementary Figure 3 | Comparison of activities of Sb-SAPCs and PCNs for photocatalytic $H_2O_2$ production** (light source: Xe lamp, light intensity at 420−500 nm: 30.3 W $m^{-2}$; reaction medium: water at pH = 10.1 for Sb-SAPC15). Error bars represent the standard deviations of 3 replicate measurements.

The pH of the Sb-SAPC15 aqueous suspension (solvent is pure water) is 10.1 because addition of Sb-SAPC15 particles significantly accelerated self-ionization of water. The zeta potential of Sb-SAPC15 reached -30 mV in an acid solution, indicating that Sb-SAPC15 could be recognized as a solid-state Lewis base. Addition of Lewis base into pure water could accelerate water self-ionization, thus leading to a significantly increased pH.

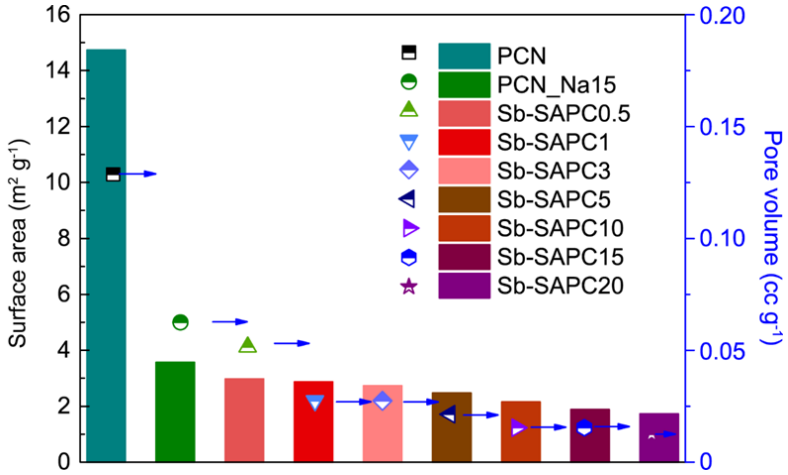


**Supplementary Figure 4 | Specific surface area and average pole volume of PCN, PCN_Na15 and Sb-SAPCx.**

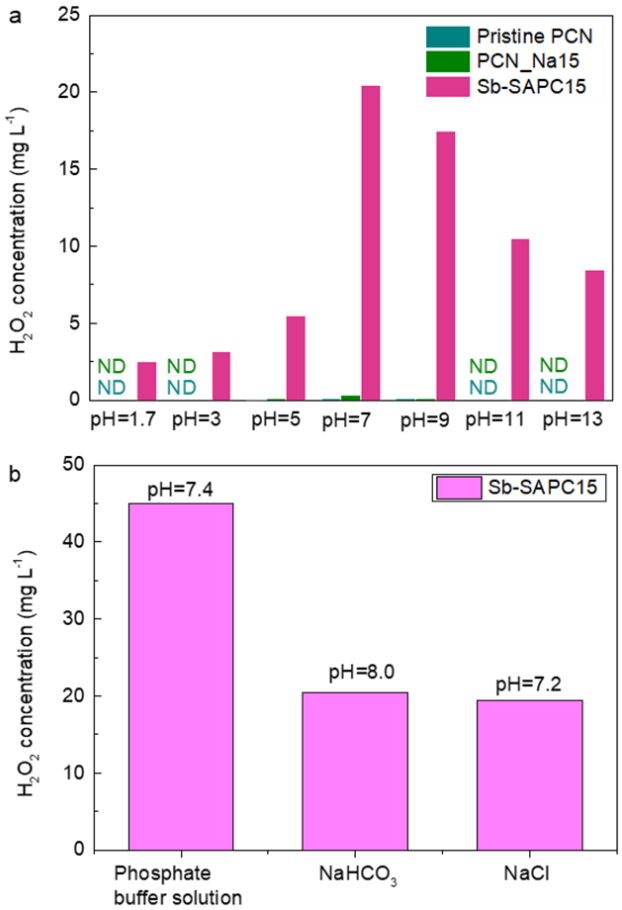


**Supplementary Figure 5 | Optimization experiments for non-sacrificial photocatalytic $H_2O_2$ production. a**, pH optimization. **b**, Solvent optimization. (light source: Xe lamp, light intensity at 420−500 nm: 30.3 W $m^{-2}$). The reaction time is 90 min.

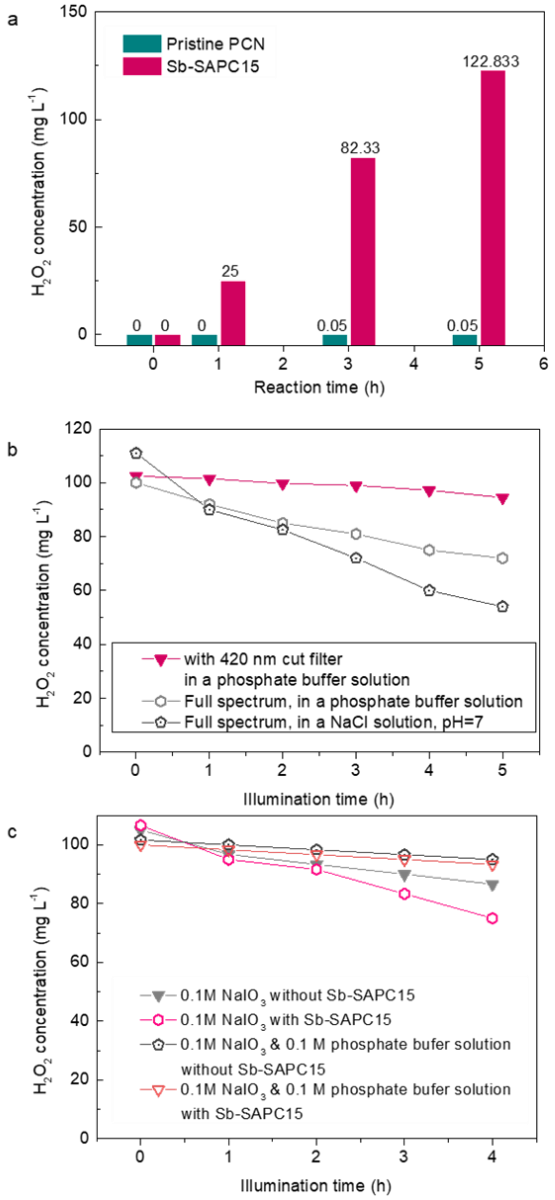


**Supplementary Figure 6 | Long term activity for non-sacrificial photocatalytic $H_2O_2$ production. a**, Long term photocatalytic $H_2O_2$ production using Sb-SAPC15 and pristine PCN as the photocatalyst. **b**, Optimization for light wavelength for $H_2O_2$ degradation study. **c**, Interactions between photogenerated holes and $H_2O_2$ in different kinds of solutions. The solution was irradiated by a 300 W Xenon Lamp with a UV cut filter (light intensity: 30.3 W $m^{-2}$ at 420-500 nm).

The change in concentration of $H_2O_2$ with an electron acceptor versus time was plotted to investigate whether the holes transferred to $H_2O_2$ (Supplementary Figure 6c). The concentration of $H_2O_2$ gradually decreased in 0.1 M $NaIO_3$ without Sb-SAPC since slight decomposition of $H_2O_2$ was unavoidable under visible light irradiation with high light intensity. After addition of Sb-SAPC15, the decomposition of $H_2O_2$ was accelerated, indicating that the transfer of photogenerated holes could decompose $H_2O_2$ in 0.1 M $NaIO_3$ solution. This phenomenon further confirmed that $H_2O_2$ could serve as a hole scavenger, which should be considered during the photocatalytic $H_2O_2$ production. However, addition of the phosphate buffer solution could significantly suppress the decomposition of $H_2O_2$. These results indicate the crucial role of phosphate buffer solution, which is able to stabilize the produced $H_2O_2$ during the photocatalytic process.

**Commented [TB59]:** Please avoid the use of "Note" after the Supplementary Figurers, as this may create confusion with the Supplementary Notes.

The text can be kept without caption.

**Commented [TB60R59]:** We have removed the word "Note" below the figures.

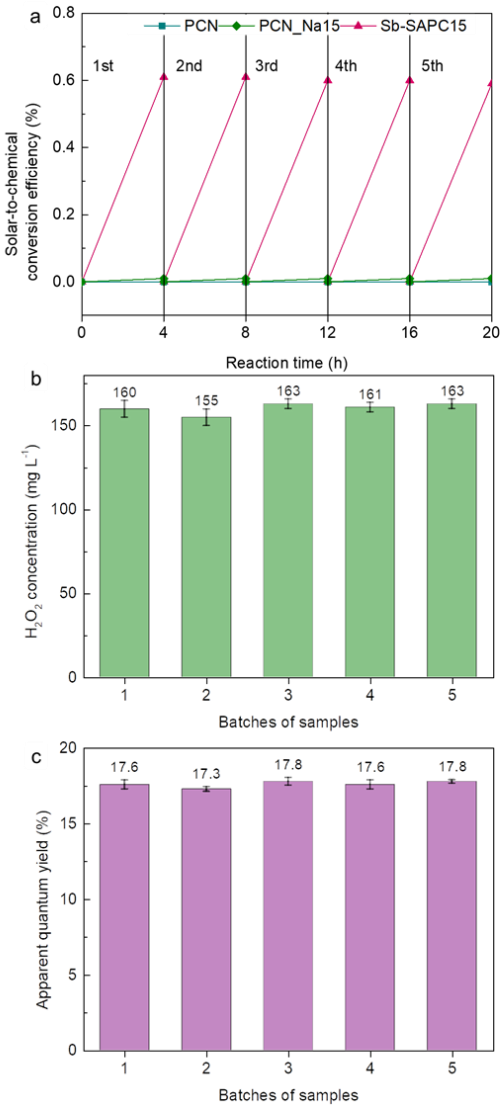


**Supplementary Figure 7 | Repeatability and reproducibility of catalysts. a**, Repeatability of the CN samples for photocatalytic production of $H_2O_2$. After each run, the catalyst was filtered and re-suspended in a fresh solution with pH adjusted to 7.4 by phosphate buffer solution. **b**, Reproducibility of photocatalytic $H_2O_2$ production for calculating solar-to-chemical conversion efficiency. **c**, Reproducibility for apparent quantum yield (λ = 420 nm). Light source: Xe lamp, light intensity at 420−500 nm: 30.3 W $m^{-2}$; reaction medium: phosphate buffer solution at pH = 7.4. Error bars represent the standard deviation of 3 replicate measurements.

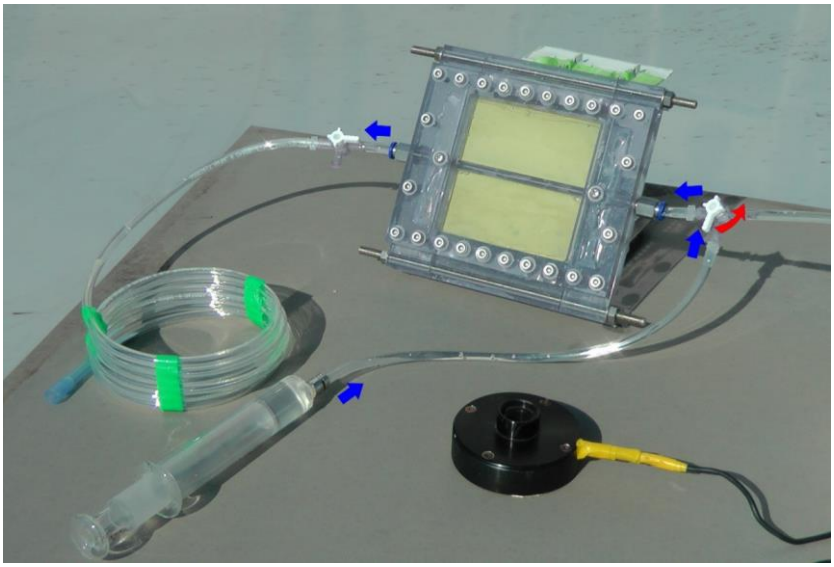

**Supplementary Figure 8 | The practical experiment of photocatalytic $H_2O_2$ production using solar light.** The blue arrow indicates the flow direction of aqueous solution. The red arrow tells the direction to open the valve.

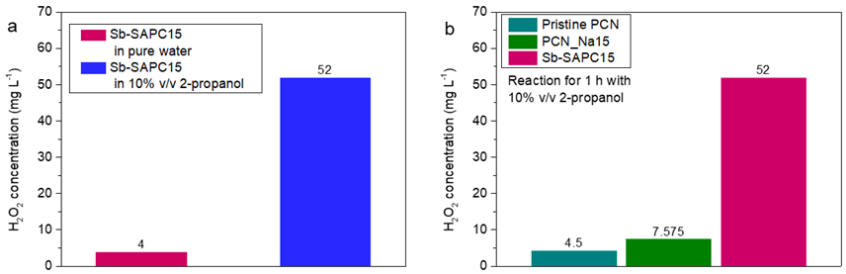


**Supplementary Figure 9 | Half reaction with addition of an electron donor. a**, Comparison of $H_2O_2$ formed in pure water and 10% (v/v) 2-propanol aqueous solution catalyzed by Sb-SAPC15. **b**, Comparison of $H_2O_2$ production in 10% (v/v) 2-propanol aqueous solution catalyzed by pristine PCN, PCN_Na15 and Sb-SAPC15. Reaction time: 60 min. Irradiation condition: λ > 420 nm (Xe lamp, light intensity at 400−500 nm: 30.3 W $m^{-2}$), at 298 K.

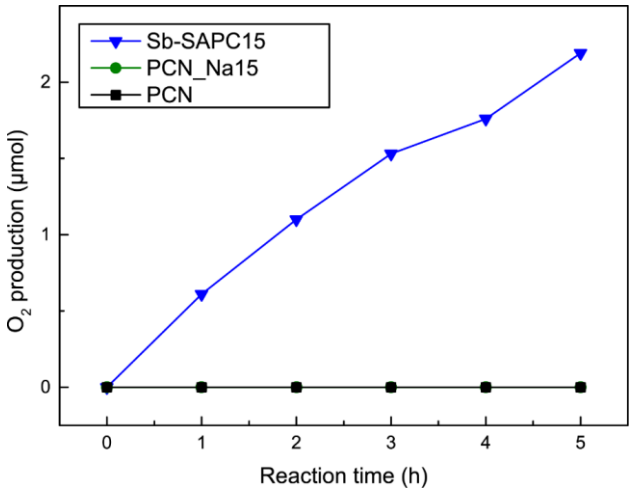


**Supplementary Figure 10 | Comparison of oxygen evolution efficiency for PCN, PCN_Na15 and Sb-SAPC15 during the half reaction.**

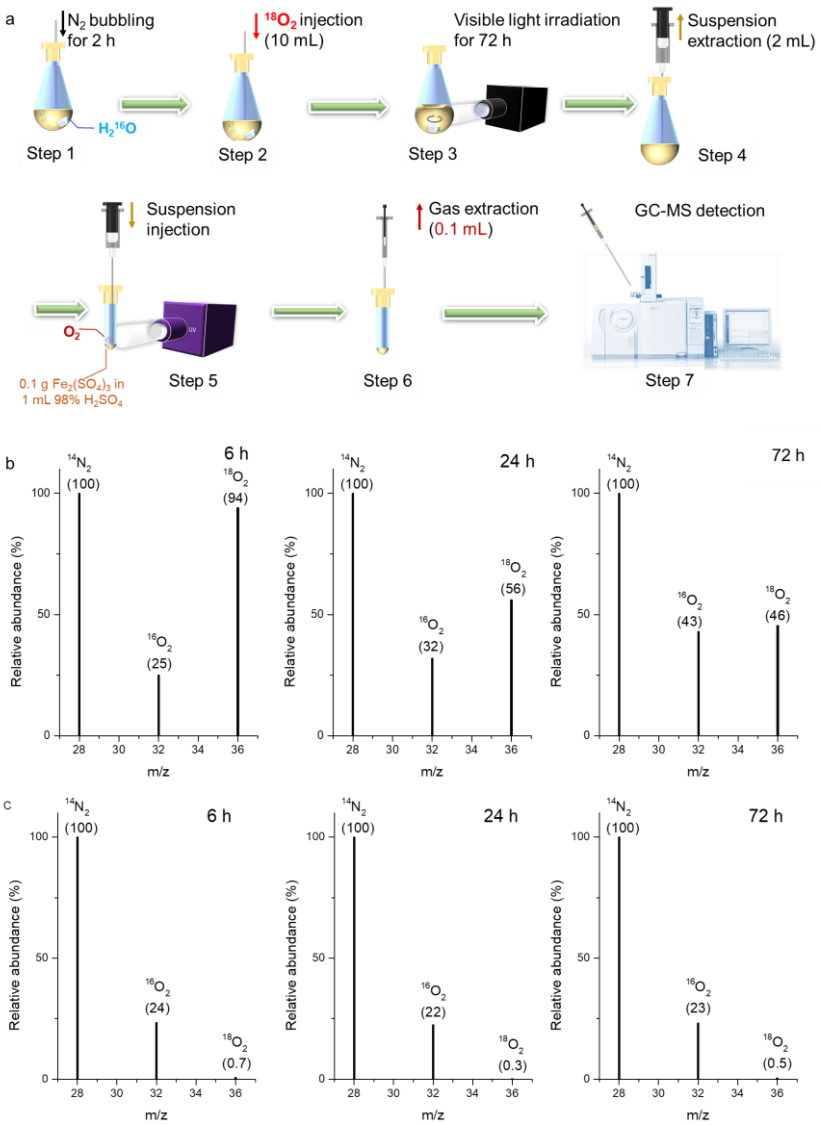


**Supplementary Figure 11 | Isotopic experiments utilizing $^{18}O_2$. a**, Schematic diagram showing the isotopic experimental procedure for $H_2O_2$ production with addition of $^{18}O_2$ as the electron acceptor (The figure of GC-MS in step 7 is taken from https://www.an.shimadzu.co.jp/gcms/2010se.htm). **b**, GC-MS spectra of the gas extracted from the Sb-SAPC15/$Fe^{3+}$ system after the light illumination for 6 h, 24 h and 72 h in step 3. **c**, GC-MS spectra of the gas extracted from the same system without addition of Sb-SAPC15 at the reaction time point of 6 h, 24 h and 72 h in step 3. The reaction solution is pure $H_2{}^{16}O$ with injection of 10 mL $^{18}O_2$.

We have performed control experiment to ensure that the $^{18}O_2$ injected at the beginning of the experiment could be barely measured later. The details for the experiment are as follows: all experiments are the same as the experimental procedure except the addition of the photocatalyst. In this case, the $H_2O_2$ could hardly be formed, and only dissolved oxygen existed in the liquid phase[1]. As shown in step 3, the dissolved oxygen could be transferred to step 4 when liquid was extracted from the solution. The gas extracted from step 6 was also measured by GC-MS. As shown in the figure above, we could hardly detect the signal of $^{18}O_2$, indicating that the dissolved oxygen in the extracted solution (step 3) barely influenced the measurement. Note that the signal of $^{16}O_2$ is attributed to the small leakage of $O_2$ during the injection process.

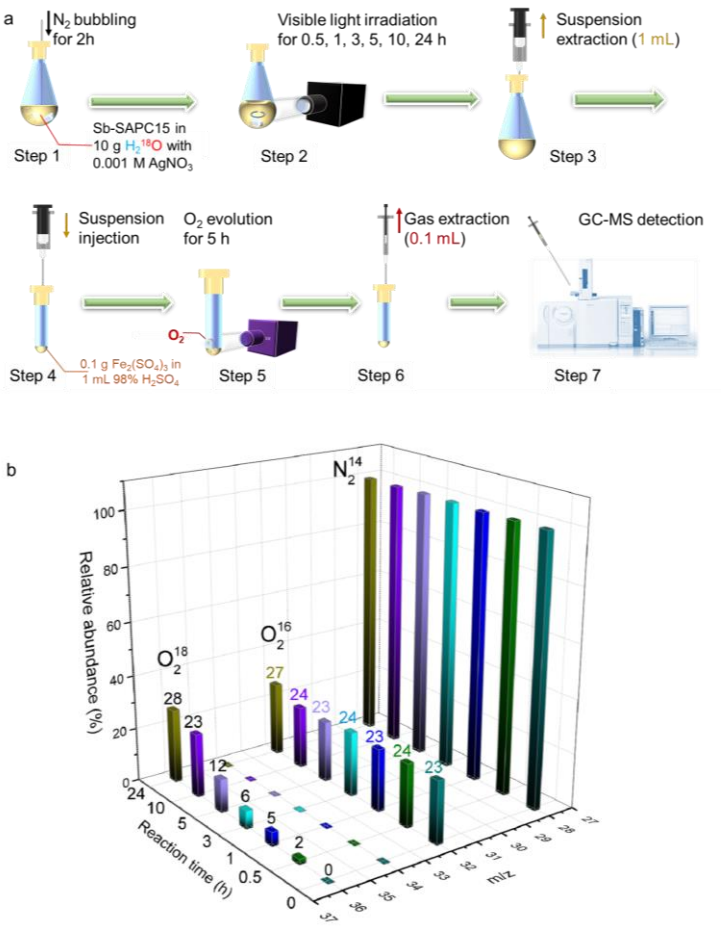


**Supplementary Figure 12 | Isotopic experiments utilizing $H_2{}^{18}O$. a**, Schematic diagram showing the isotopic experimental procedure for $H_2O_2$ production with addition of $Ag^+$ as the electron acceptor (The figure of GC-MS in step 7 is taken from https://www.an.shimadzu.co.jp/gcms/2010se.htm). **b**, GC-MS spectra of the gas extracted from the Sb-SAPC15/$Fe^{3+}$ system after the Xenon lamp illumination of 0 h, 0.5 h, 1 h, 3 h, 5 h, 10 h and 24 h in step 2. The reaction solution is pure $H_2{}^{18}O$ with saturated ultrapure $N_2$. (Mass of the catalyst in step 1: 50 mg, $Ag^+$ concentration: 0.001M).

The signal of $^{16}O_2$ is attributed to the small leakage of $O_2$ during the injection process (step 7) since the signals of $^{16}O_2$ are almost the same (~23 %). Similar phenomenon could be also observed in the Supplementary Figure 11c even no $^{16}O_2$ was injected in the system. Although this system error existed, the increasing signal of $^{18}O_2$ with extended reaction time still revealed the water oxidation gradually happened with the addition of the electron acceptor.

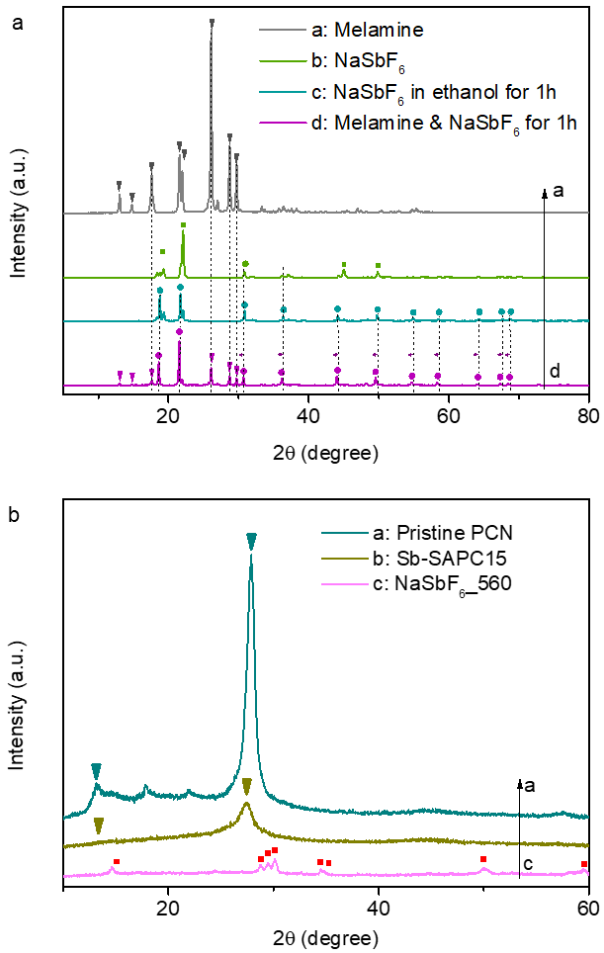


**Supplementary Figure 13 | X-ray diffraction (XRD) patterns. a**, XRD patterns of a: melamine; b: $NaSbF_6$; c: 3.881 g $NaSbF_6$ in ethanol with sonification for 1 hour (*Intermediate Product 1*); d: sample c mixed with 4 g of melamine in ethanol with 1 hour sonification (*Intermediate Product 2*). **b**, XRD patterns of pristine PCN, Sb-SAPC15 and $NaSbF_6$ prepared at 560 °C for 4 h ($NaSbF_6$_560).

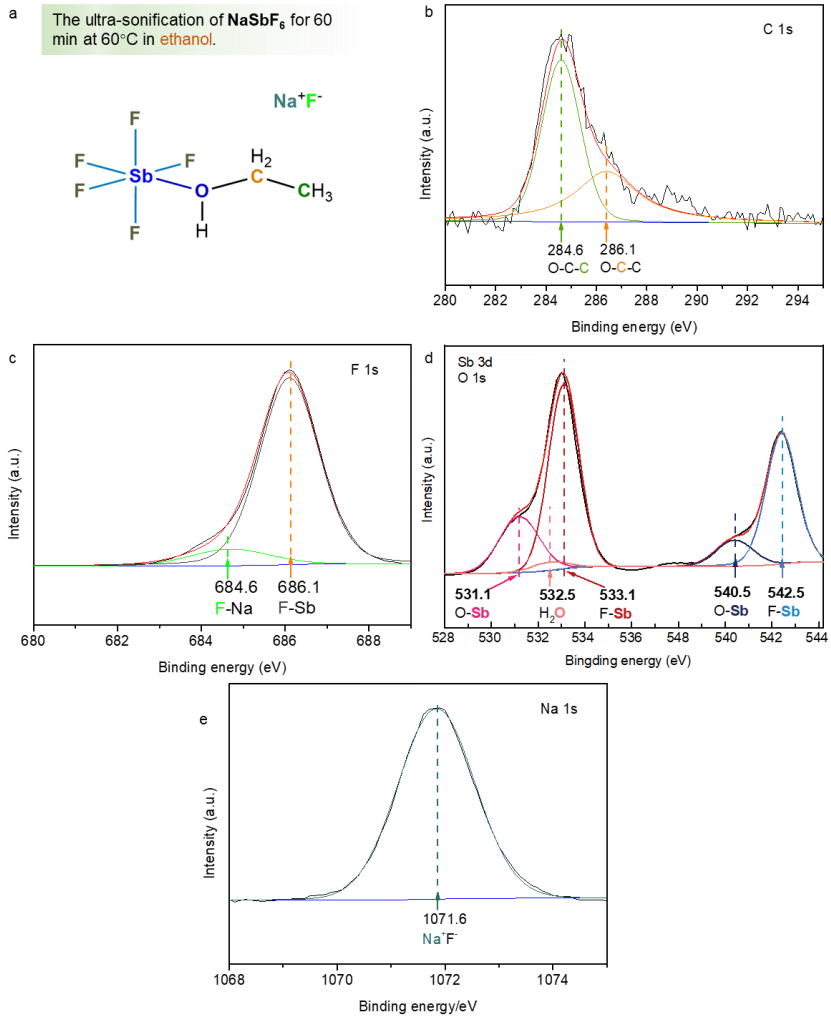


**Supplementary Figure 14 | XPS spectra of 3.881 g $NaSbF_6$ in ethanol with sonification for 1 hour (*Intermediate Product 1*). a**, Structure of *Intermediate Product 1*. **b-e**, High-resolution XPS spectra of C 1s (**b**), F 1s (**c**), Sb3d & O 1s (**d**) and Na 1s (**e**).

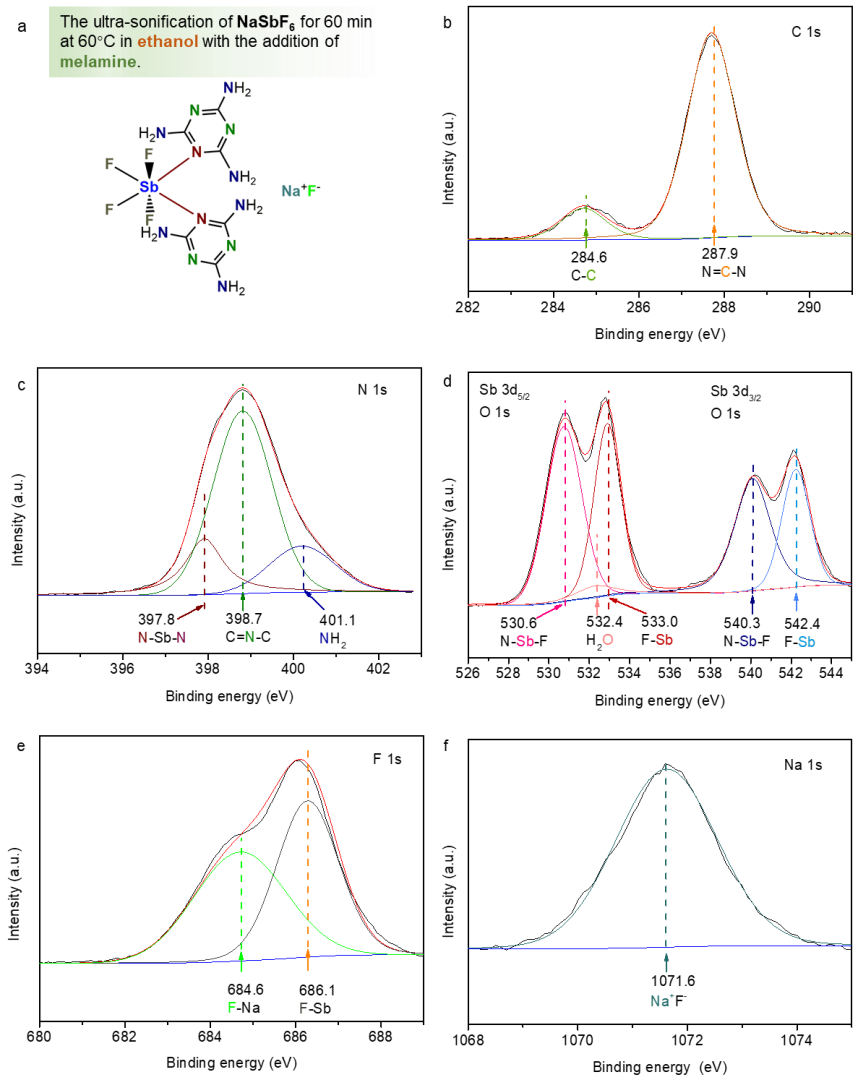


**Supplementary Figure 15 | XPS spectra of 3.881 g $NaSbF_6$ in ethanol with sonification for 1 hour, followed by mixed with 4 g of melamine in ethanol with 1 hour sonification (*Intermediate Product 2*). a**, Structure of *Intermediate Product 2*. **b-f**, High-resolution XPS spectra of C 1s (**b**), N 1s (**c**), Sb3d & O 1s (**d**), F 1s (**e**) and Na 1s (**f**).

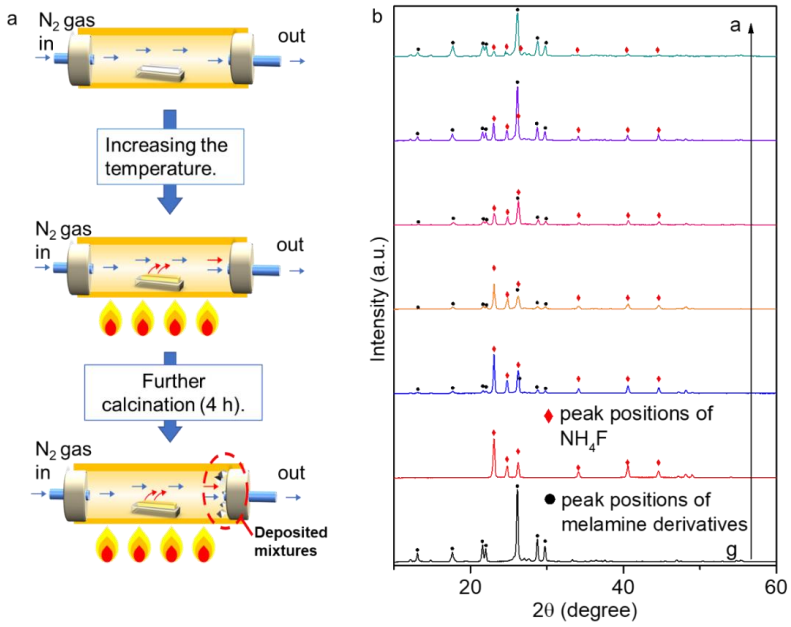


**Supplementary Figure 16 | Characterization of the deposited mixture on the silicone plug of the tube furnace. a**, A schematic diagram showing the deposition process during calcination. **b**, XRD patterns of the deposited mixture obtained during preparation of Sb-SAPC1 (pattern a), Sb-SAPC3 (pattern b), Sb-SAPC5 (pattern c), Sb-SAPC10 (pattern d), and Sb-SAPC15 (pattern e). XRD patterns of pure $NH_4F$ (pattern f) and the deposited mixture during preparation of PCN (pattern g) are also included as references.

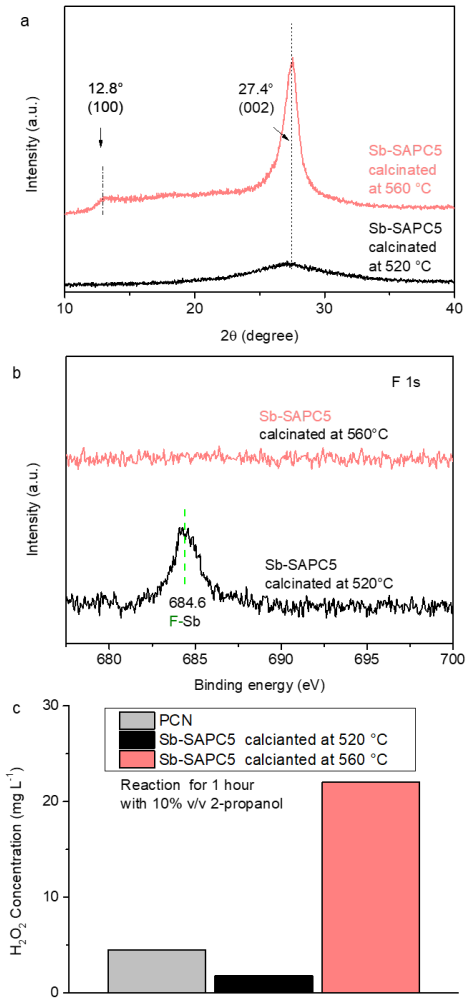


**Supplementary Figure 17 | Comparison of Sb-SAPCs prepared at different temperatures. a-b** XRD patterns (**a**) and high-resolution F 1s spectra (**b**) of Sb-SAPC5 prepared at 520 °C and 560 °C. **c**, Comparison of $H_2O_2$ formed 10% (v/v) 2-propanol aqueous solution catalyzed by PCN and Sb-SAPC5 prepared at 520 °C and 560 °C. Reaction time: 60 min. Irradiation condition: λ > 420 nm (Xe lamp, light intensity at 400−500 nm: 30.3 W $m^{-2}$), at 298 K.

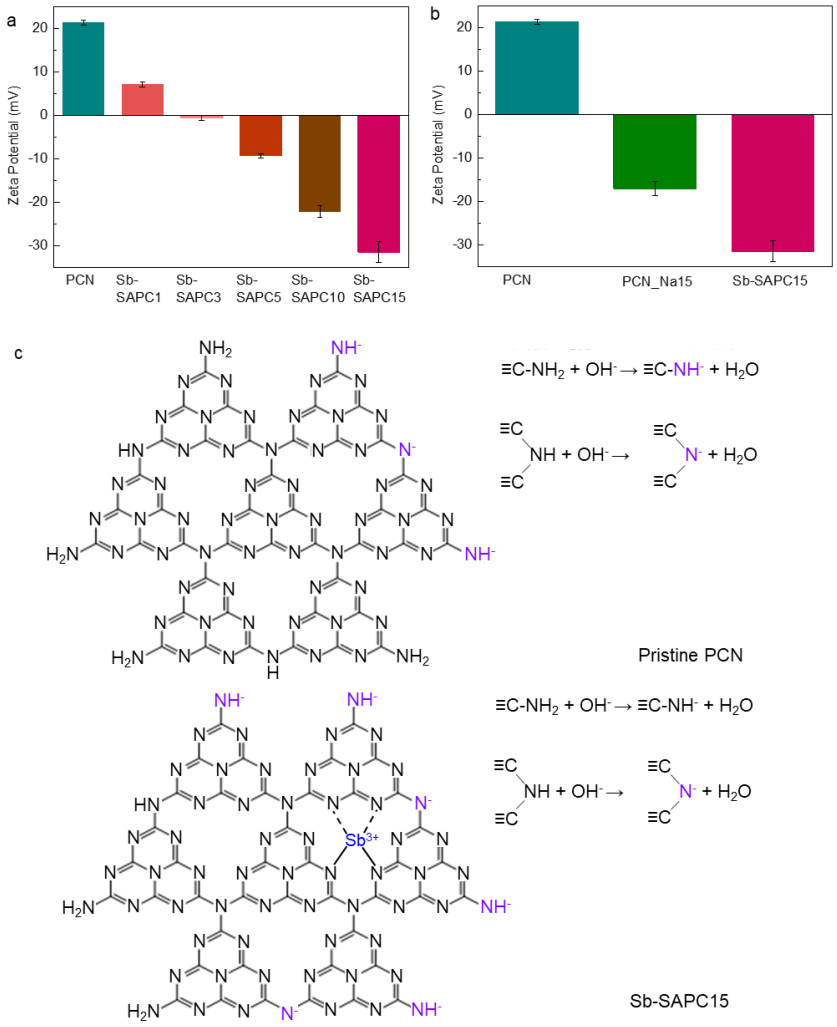


**Supplementary Figure 18 | Surface charge of Sb-SAPCs and PCN samples at pH = 3.** **a**, Zeta-potential of Sb-SAPCs with different Sb contents. **b**, Zeta-potential of PCN, PCN_Na15 and Sb-SAPC15. **c**, The possible mechanism of gradually increased surface negativity of Sb-SAPCs.

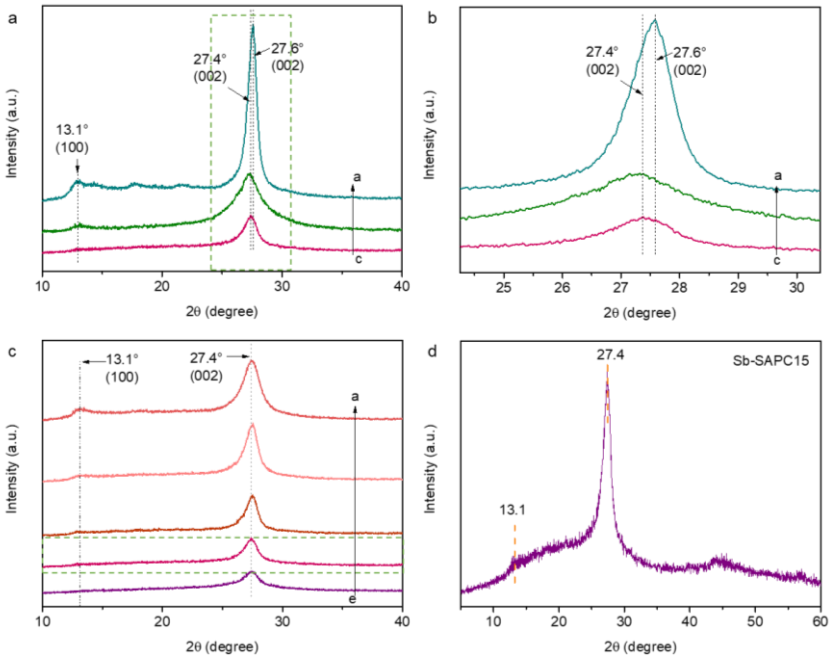


**Supplementary Figure 19 | Crystallinity characterized by X-ray diffraction. a**, XRD patterns of a: pristine PCN; b: PCN_Na15; and c: Sb-SAPC15. **b**, XRD patterns (high-resolution) of carbon nitride samples. **c**, XRD patterns of a: Sb-SAPC1; b: Sb-SAPC5; c: Sb-SAPC10; d: Sb-SAPC15; and e: Sb-SAPC20. **d**, XRD patterns (high-resolution) of Sb-SAPC15.

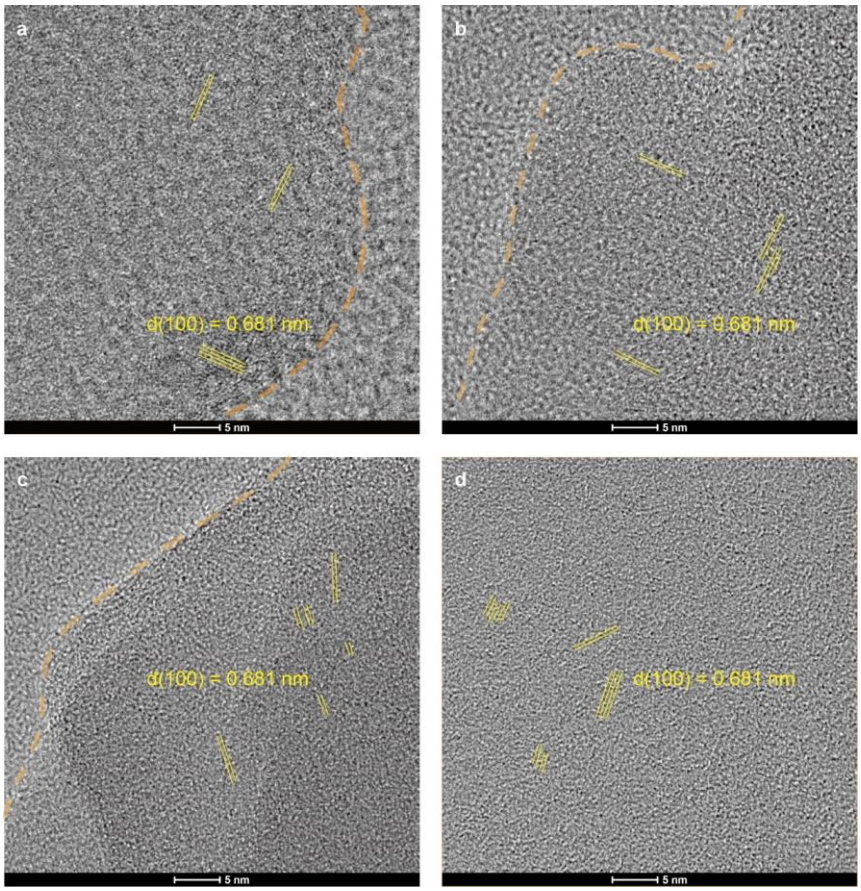


**Supplementary Figure 20 | Crystallinity characterized by high-resolution transmission electron microscopy. a-d**, HR-TEM images of Sb-SAPC1 (**a**), Sb-SAPC5 (**b**), Sb-SAPC10 (**c**) and Sb-SAPC15 (**d**). The yellow line indicates the lattice fringe of the (100) plane of PCN.

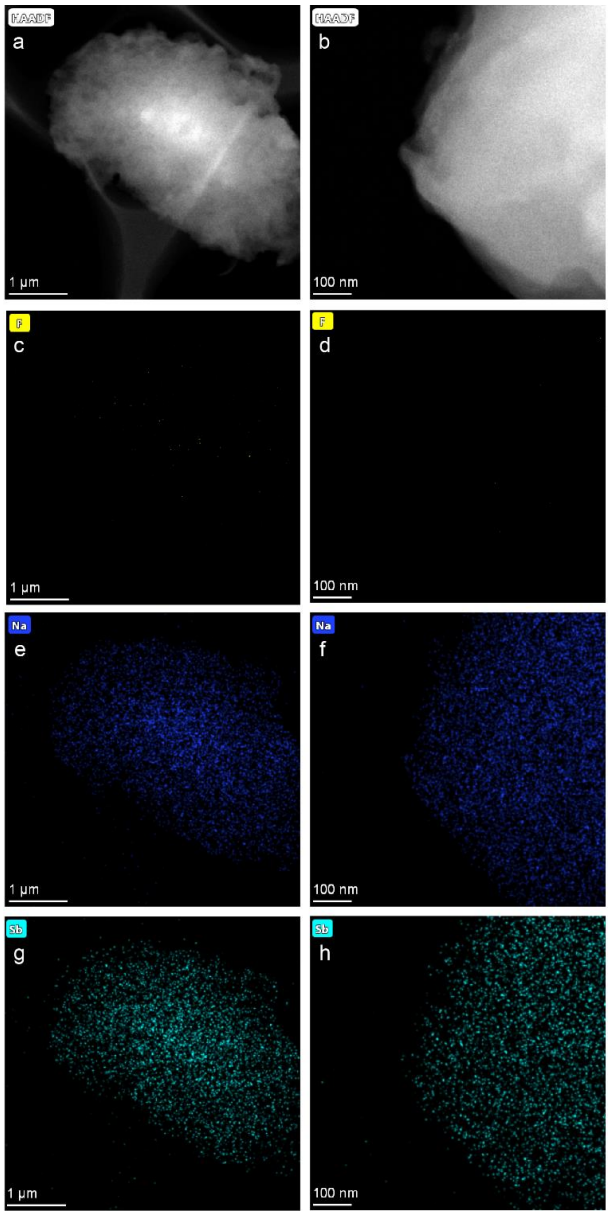


**Supplementary Figure 21 | Elemental distribution in Sb-SAPC15. a-b**, Low and high-magnification HAADF-STEM images of Sb-SAPC15. **c-h**, The corresponding EDS elemental mapping images of F (**c-d**), Na (**e-f**) and Sb (**g-h**) at low and high-magnification.

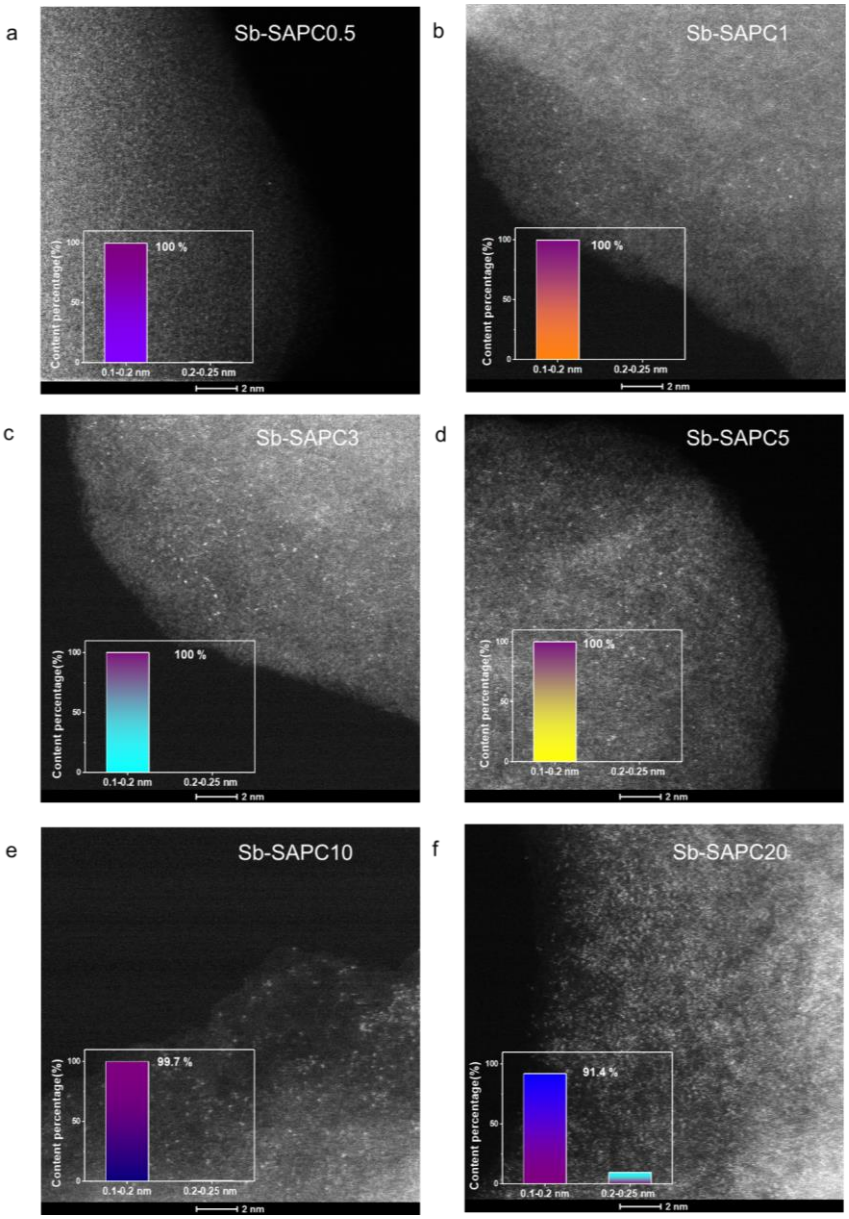


**Supplementary Figure 22 | Characterization of isolated Sb species in Sb-SAPCs with different Sb contents. a-f**, HAADF-STEM images of Sb-SAPC0.5 (**a**), Sb-SAPC1 (**b**), Sb-SAPC3 (**c**), Sb-SAPC5 (**d**), Sb-SAPC10 (**e**) and Sb-SAPC20 (**f**). Inset shows the size distribution of the bright spots.

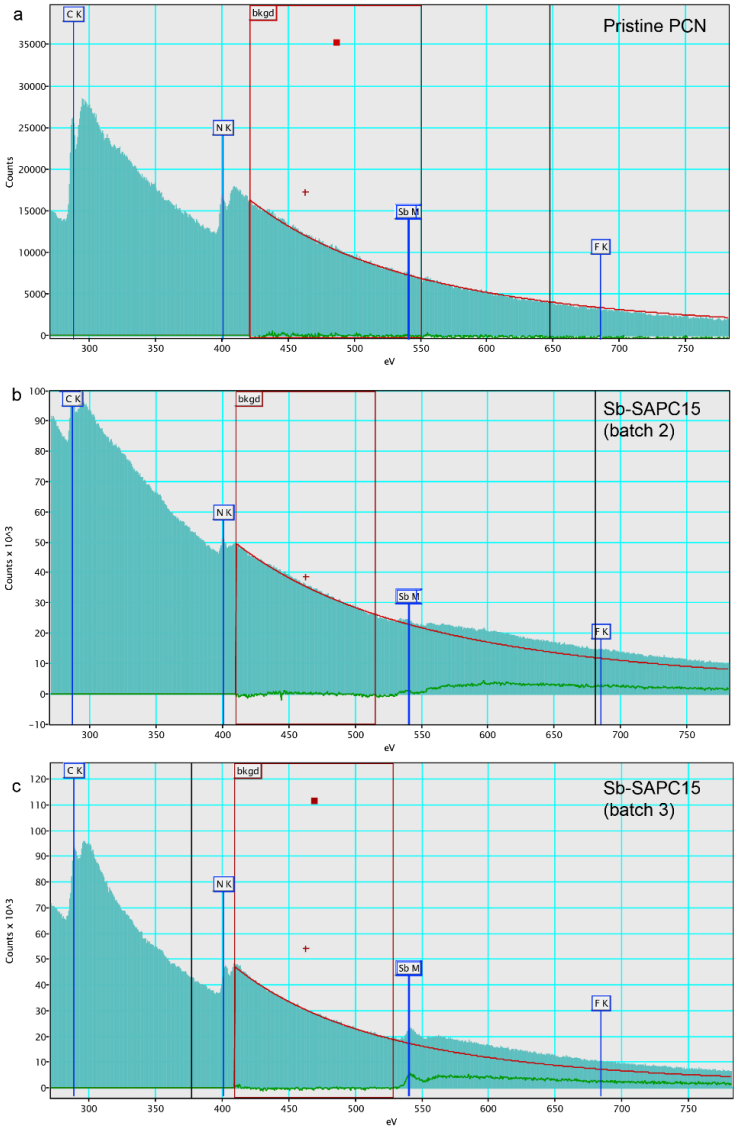


**Supplementary Figure 23 | EELS spectra of CN samples. a**, pristine PCN. **b**, Sb-SAPC15 (batch 2). **c**, Sb-SAPC15 (batch 3).

No edge could be detected at energy range of 685-695 eV of these 3 spectra[23], further suggesting no F in Sb-SAPC.

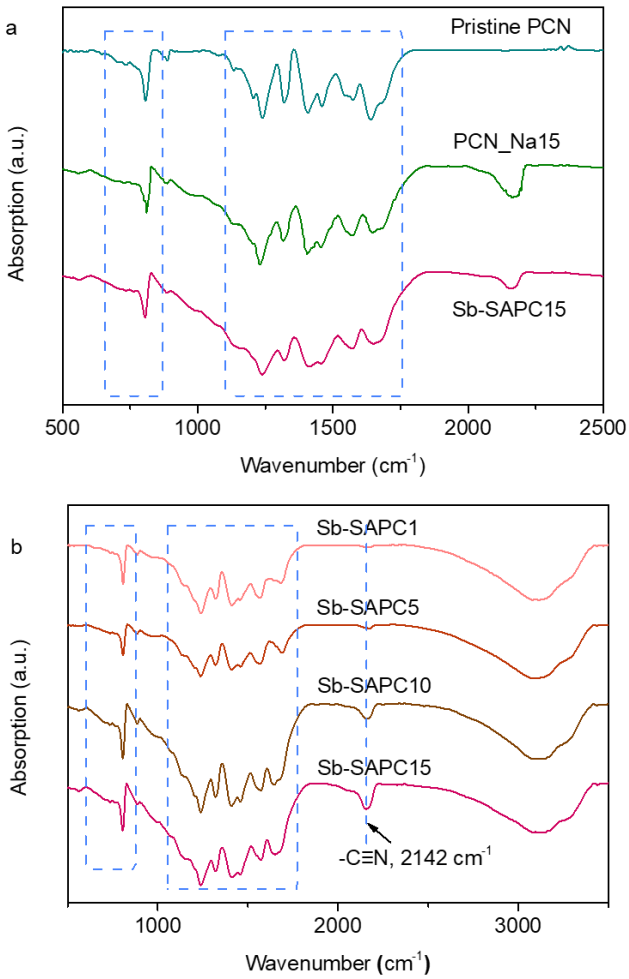


**Supplementary Figure 24 | FT-IR spectra of PCN samples and Sb-SAPCs. a**, FT-IR spectra of pristine PCN, PCN_Na15, and Sb-SAPC15. **b**, FT-IR spectra of Sb-SAPC1, Sb-SAPC5, Sb-SAPC10 and Sb-SAPC15.

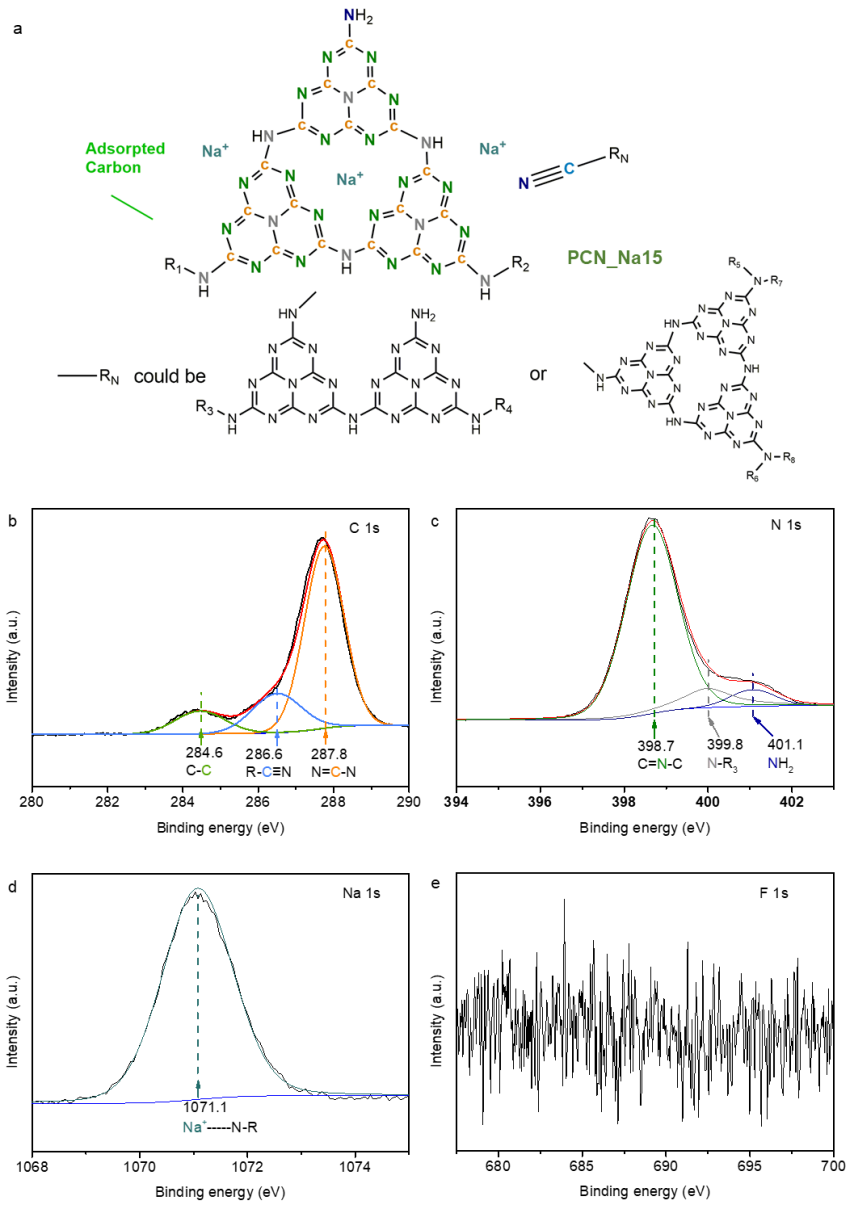


**Supplementary Figure 25 | Surface chemical states of PCN_Na15. a**, Schematic diagram showing the chemical states of elements in PCN_Na15. **b-e**, High-resolution XPS spectra of PCN_Na15: C 1s (**b**); N 1s (**c**); Na 1s (**d**); and F 1s (**e**).

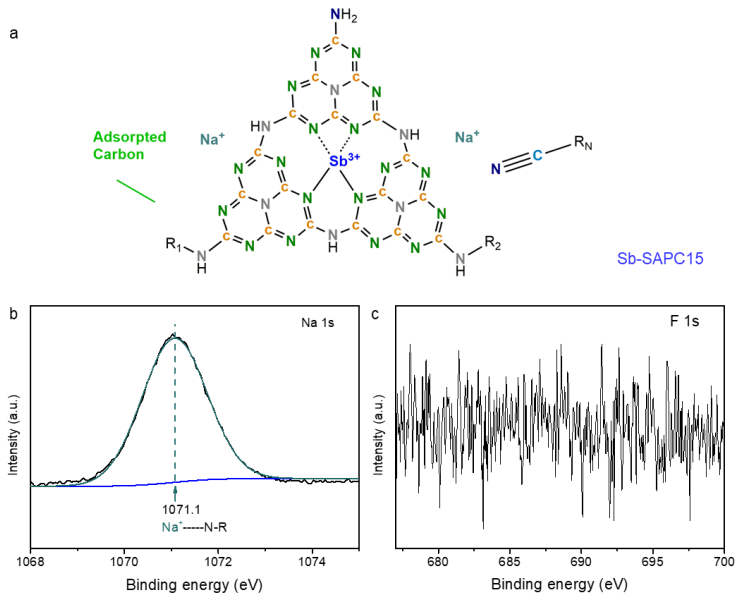


**Supplementary Figure 26 | Surface chemical states of Sb-SAPC15. a**, Schematic diagram showing the chemical states of elements in Sb-SAPC15. **b-c**, High-resolution XPS spectra of Sb-SAPC15: Na 1s (**b**) and F 1s (**c**).

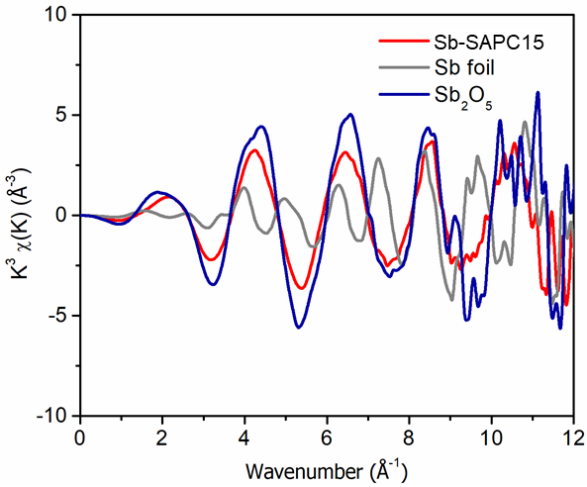


**Supplementary Figure 27 | Extended X-ray absorption fine structure (EXAFS, $k^3$-weighted k-space) of Sb-SAPC15.** The spectrum of Sb-SAPC15 show a significant difference compared with references spectra (Sb foil and $Sb_2O_5$).

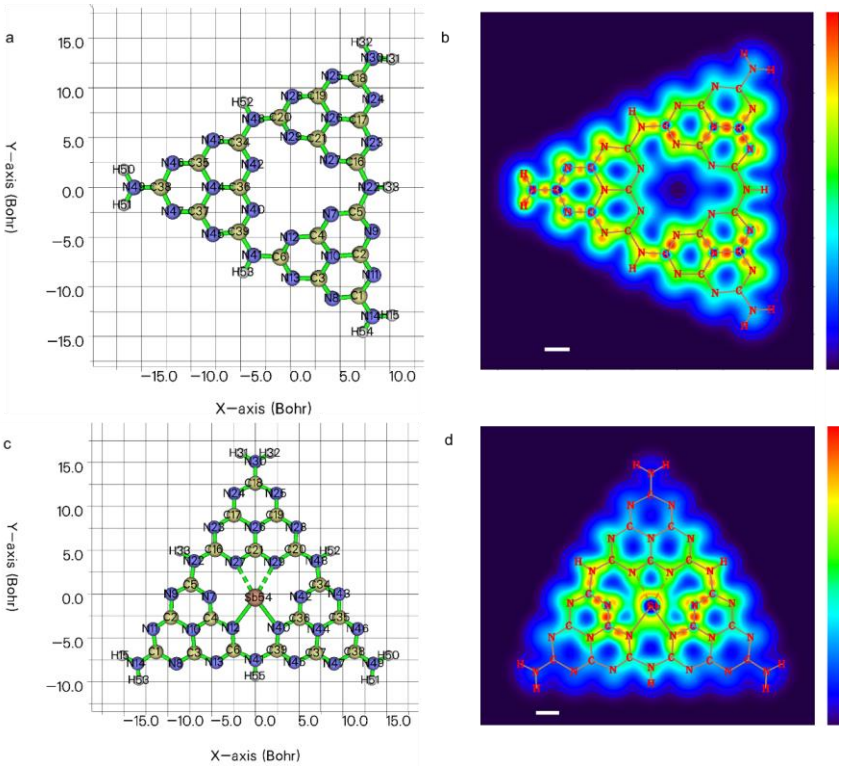


**Supplementary Figure 28 | Optimized geometry configuration and localized orbital locator of cluster models. a**, Optimized geometry configuration and atomic numbers of Melem_3 to represent pristine PCN. **b**, Localized orbital locator calculated based on π MOs of melem_3 (XY plane, Z = 0.45 Bohr). **c**, Optimized geometry configuration and atomic numbers of melem_3Sb3+ to represent Sb-SAPCs. **d**, Localized orbital locator calculated based on π MOs of melem_3Sb3+ (XY plane, Z = 1.2 Bohr). The dashed bonds refer to the weak interaction between N and Sb atoms. The scale bars in (**b**) and (**d**) are 5 Bohr. The maximum and minimum electronic density in (**b**) and (**d**) are 0.00 and 0.75.

As shown in Supplementary Figure 28c & d, the sum of occupied π MOs at N12 and N40 strongly interacts with that at Sb54, thus two strong covalent bonds can be formed. Additionally, the sum of occupied π MOs at N27 and N28 also interacts with that at Sb54. The summed electronic intensity between N27 and Sb54 (as well as N28 and Sb54) is slightly weaker that that between N12 and Sb54 (as well as N40 and Sb54), indicating the slightly weaker interaction between N27 and Sb54 (Supplementary Figure 28d). These results further manifest the best fitting result for the first shell that each Sb atom is coordinated with about 3.3 N atoms in average (Figure 2h).

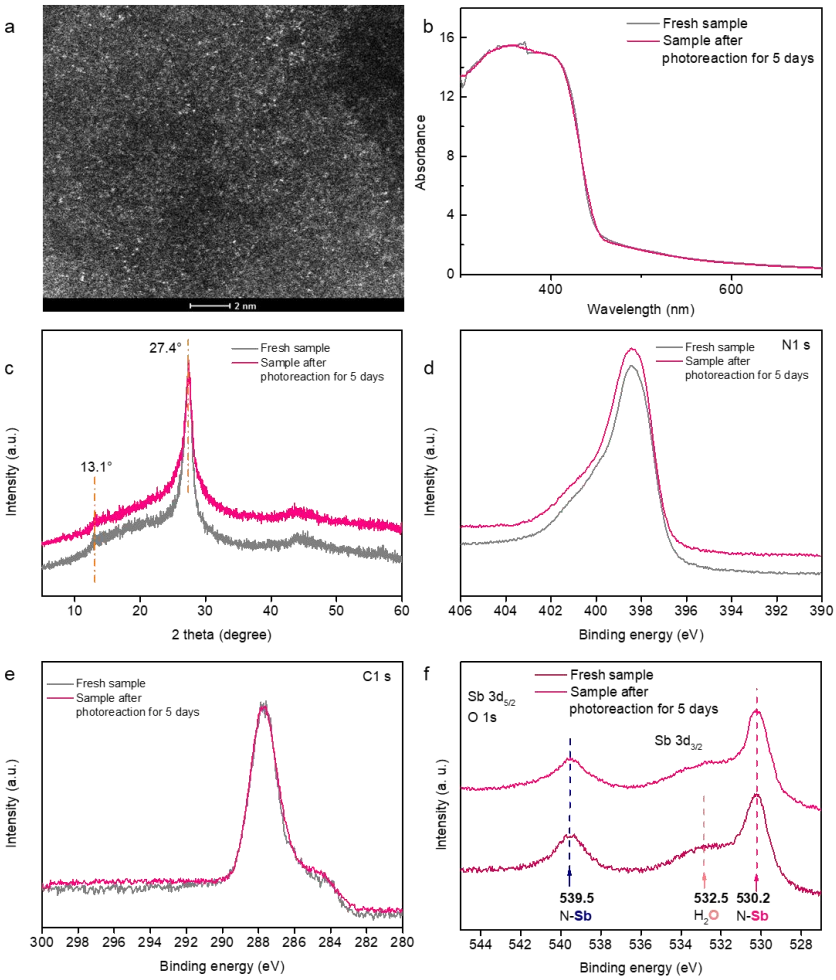


**Supplementary Figure 29 | Post-characterization of Sb-SAPC15 after photocatalysis.** **a**, HAADF STEM image of Sb-SAPC15 after 5 days of photoreaction. **b-f**, Comparison of as-prepared Sb-SAPC15 and Sb-SAPC15 after 5 days of photoreaction: (**b**) UV-vis spectra; (**c**) XRD pattern; (**d**) high resolution XPS N 1s spectra; (**e**) high resolution XPS C 1s spectra; and (**f**) high resolution XPS O 1s and Sb 3d XPS spectra. After every 8 h of reaction, the reaction solution was exchanged by fresh 0.1 M phosphate buffer solution saturated with $O_2$. Light intensity: 30.3 W $m^{-2}$ at 420-500 nm.

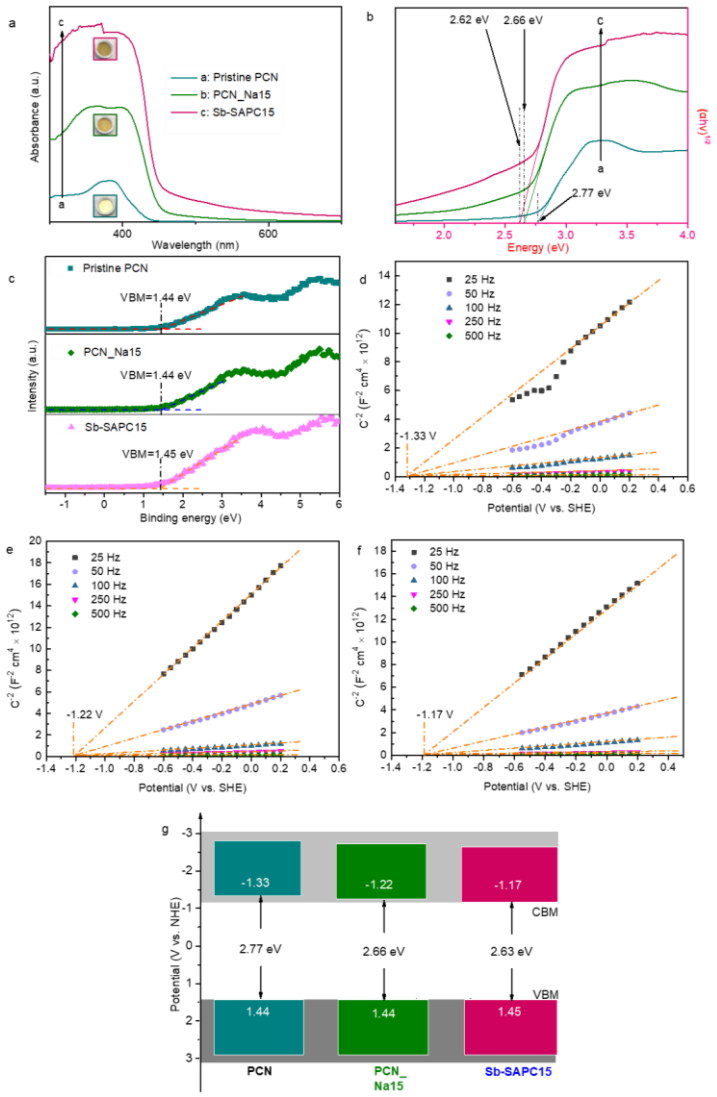


**Supplementary Figure 30 | Characterization of the CBM and VBM. a**, UV-vis diffuse reflection spectra of pristine PCN, PCN_Na15 and Sb-SAPC15. **b**, Tauc plot of pristine PCN, PCN_Na15 and Sb-SAPC15. **c**, Valence-band XPS spectra of pristine PCN, PCN_Na15 and Sb-SAPC15. **d-f**, Mott Schottky plots of (**d**) pristine PCN, (**e**) PCN_Na15 and (**f**) Sb-SAPC15. **g**, Band structure diagrams of PCN, PCN_Na15 and Sb-SAPC15. The Fermi level of the instrument (VB-XPS) is equilibrated at 4.5 eV utilizing Au metal basis as the reference. In this case, the numerical value of the binding energy in the calibrated VB-XPS spectrum is the same as the potential vs. normal hydrogen electrode.

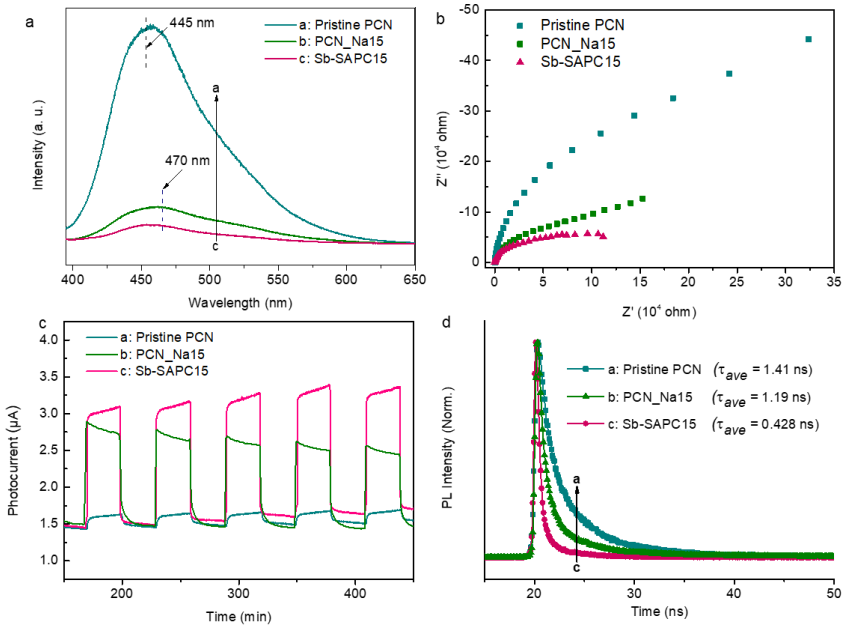


**Supplementary Figure 31 | Evaluation of charge separation. a**, Photoluminescence spectra of PCN, PCN_Na15 and Sb-SAPC15 at an excitation wavelength of 380 nm. **b**, Electrochemical impedance spectroscopy (EIS) spectra (Nyquist plots) of pristine PCN and Sb-SAPC15 in the frequency range from 100 kHz to 0.01 Hz at 0.6 V (vs. Ag/AgCl) under visible light irradiation. **c**, Comparison of photocurrent response between pristine PCN and Sb-SAPC15 at -0.6 V (vs. Ag/AgCl) under visible light illumination. The light source used in the EIS and photocurrent measurement is a Xe lamp with a UV cut ($\lambda$ > 420 nm) filter (light intensity at 420−500 nm: 30.3 W $m^{-2}$). **d**, Time-resolved photoluminescence spectra of pristine PCN, PCN_Na15 and Sb-SAPC15 recorded at 25 °C. The electrolyte used for the EIS and photocurrent measurement is 0.1 M phosphate buffer (pH = 7.4).

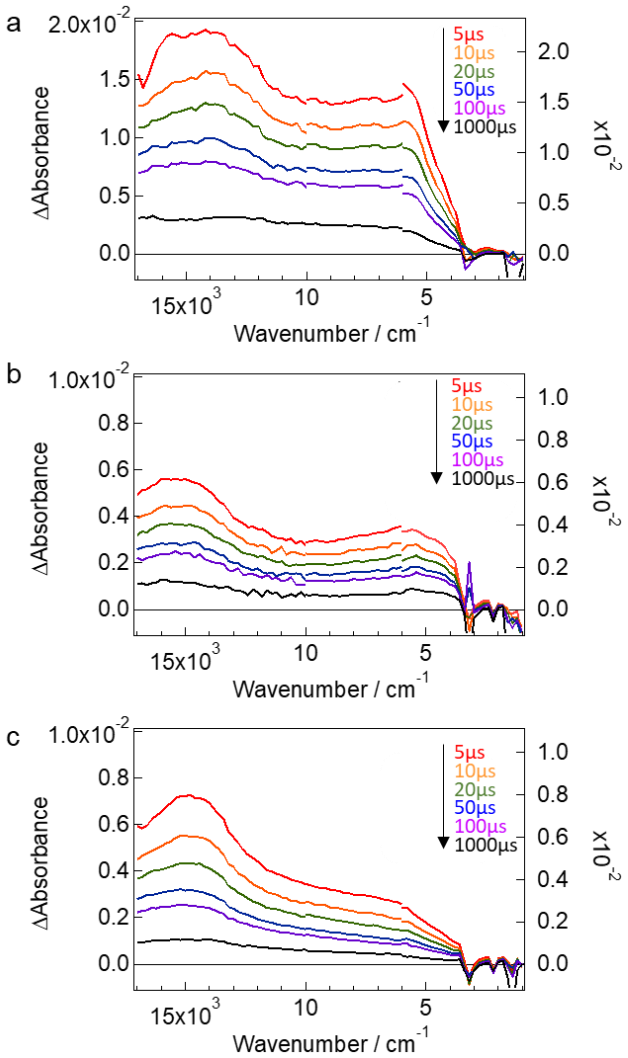


**Supplementary Figure 32 | Transient infrared red (IR) absorption spectra. a-c**, Transient IR absorption spectra for PCN (**a**), PCN_Na15 (**b**) and Sb-SAPC15 (**c**) evolved after 420 nm laser pulse excitation under vacuum (6 ns, 5 mJ, 5 Hz).

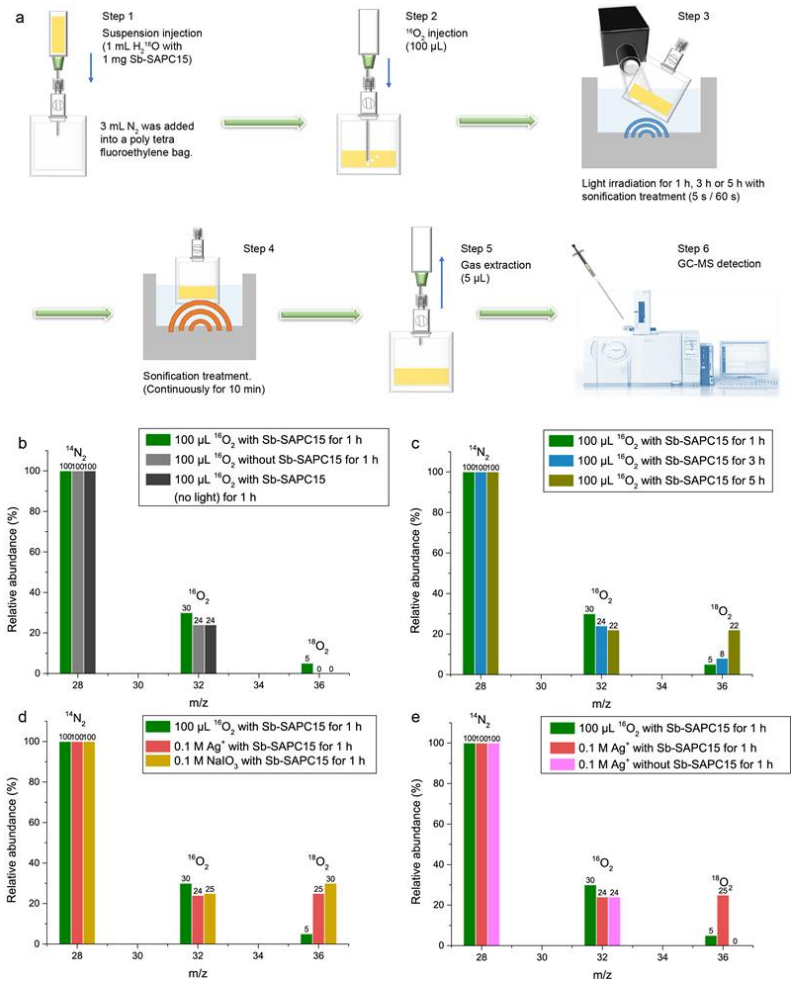


**Supplementary Figure 33 | Water oxidation mechanism. a**, Schematic diagram showing the isotopic experiment for $H_2O_2$ production with addition of $^{16}O_2$ as the electron acceptor and $H_2{}^{18}O$ as the electron donor (The figure of GC-MS in step 7 is taken from https://www.an.shimadzu.co.jp/gcms/2010se.htm). **b**, GC-MS spectra of the gas extracted from the Sb-SAPC15 system with $^{16}O_2$ as the electron acceptor and $H_2{}^{18}O$ as the electron donor. Control experiments without addition of Sb-SAPC15 or without light irradiation were conducted for confirming the photo-induced oxygen generation reaction. **c**, GC-MS spectra of the gas extracted from the Sb-SAPC15 system after Xenon lamp illumination of 1 h, 3 h and 5 h in step 3. **d**, GC-MS spectra of the gas extracted from the Sb-SAPC15 system with different electron acceptors (100 μL $O_2$, 0.1 M $Ag^+$ or 0.1 M $NaIO_3$). **e**, GC-MS spectra of the gas extracted from the system with or without addition of Sb-SAPC in condition of adding different electron acceptors (100 μL $O_2$ or 0.1 M $Ag^+$).

With increasing irradiation time, the signal of $^{18}O_2$ (m/z = 36) gradually increased (Supplementary Figure 33c). Additionally, we also investigated the oxygen generation with addition of other electron acceptors (0.1 M $Ag^+$ or 0.1 M $NaIO_3$). The signal of $^{18}O_2$ (m/z = 36) significantly increased after addition of silver ion or $NaIO_3$ compared to the case with injection of 100 μL $^{16}O_2$ (Supplementary Figure 33d), indicating that both of silver ion and $NaIO_3$ could serve as efficient sacrificial regent for oxygen evolution. To investigate whether the $Ag^+$ could directly produce oxygen or work as the sacrificial regent, we conducted a control experiment with Ag in solution. As shown in Supplementary Figure 33e, the signal of $^{18}O_2$ (m/z = 36) could not be detected without the addition of photocatalyst, indicating that pure $Ag^+$ in the system could not produce $O_2$, which suggests that the $Ag^+$ just serves as a sacrificial regent for photocatalytic WOR.

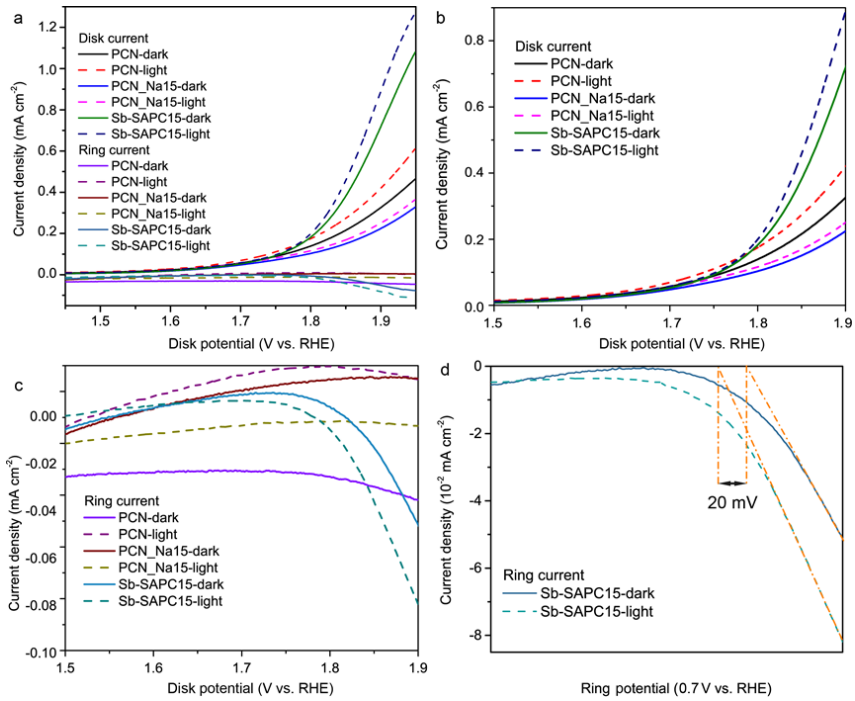


**Supplementary Figure 34 | The anodic polarization curves of rotating ring disk electrode modified by PCN, PCN_Na15 and Sb-SAPC15 with or without light irradiation. a**, Comparison of the anodic polarization curves of the rotating ring disk electrode PCN, PCN_Na15 and Sb-SAPC15 irradiated by light or in the dark condition. **b**, Anodic polarization curves of the rotating disk electrode PCN, PCN_Na15 and Sb-SAPC15 in dark condition or with light irradiation. **c**, Anodic polarization curves of the ring electrode PCN, PCN_Na15 and Sb-SAPC15 with light irradiation or in absence of light. **d**, Enlarged ring current of rotating ring disk electrode modified by Sb-SAPC15. The disk potential was shifted from 1.4 to 1.95 V (vs. RHE), and the potential of the ring was set at 0.7 V (vs. RHE). In this case, the signal of $O_2$ reduction to $H_2O$ (0.7 V vs. RHE) could be immediately captured by the ring electrode if $O_2$ was generated by water oxidation reaction. Solution: 0.1 M KOH aqueous solution (pH = 12.9).

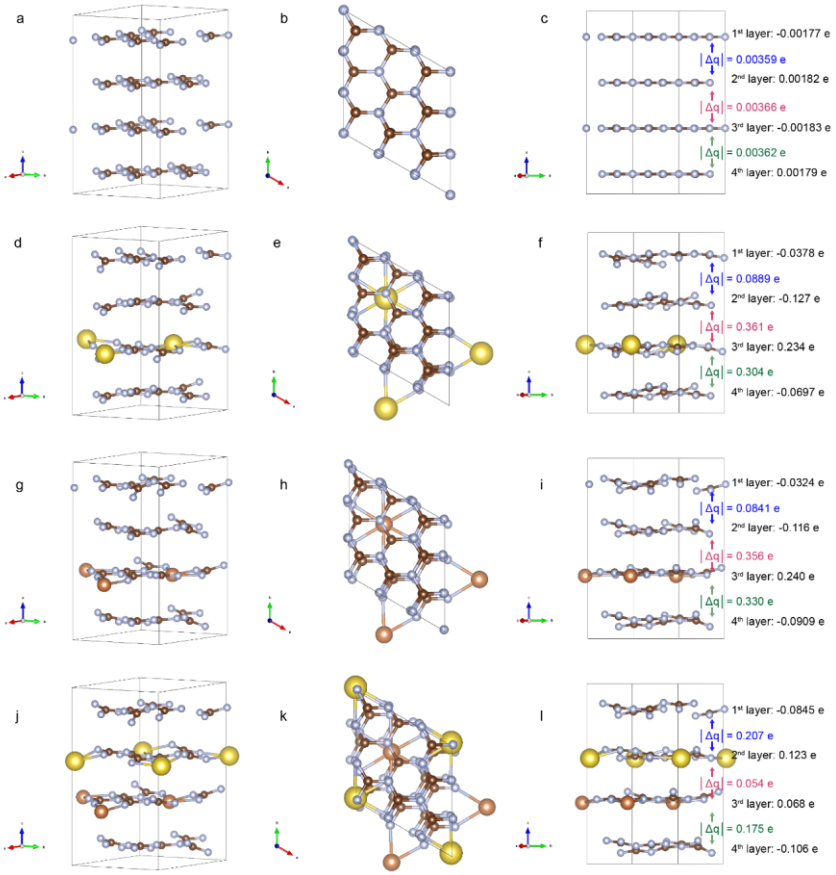


**Supplementary Figure 35 | Bader Charge distribution analysis from density functional theory (DFT) calculations. a-l**, Charge distribution of pristine GCN (**a-c**), Na-GCN (**d-f**), Sb-GCN (**g-i**), and NaSb-GCN (**j-l**). lΔql represents the absolute value of the difference of the electron distribution between the layers.

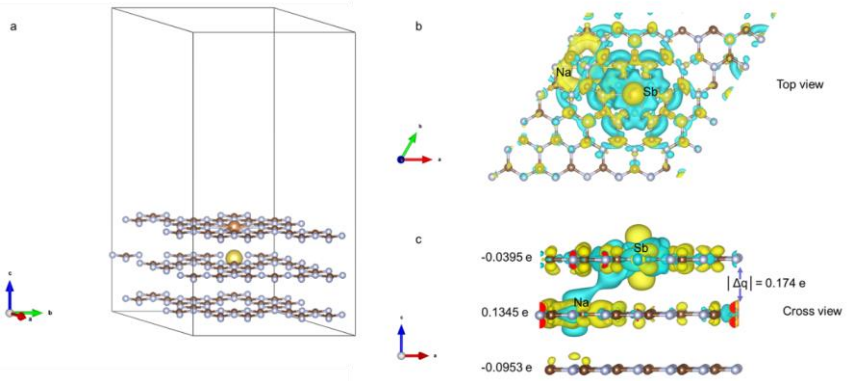


**Supplementary Figure 36 | Charge distribution analysis near surface of NaSb-GCN from density functional theory (DFT) calculations. a**, Optimized near surface crystal structure of NaSb-GCN. **b-c**, Enlarged top view (**b**) and cross view (**c**) of NaSb-GCN. lΔql represents the absolute value of the difference of electron distribution between the first and second layer. Yellow color represents electron accumulation and blue color represents electron depletion.

**Commented [TB61]:** ** Electronic structure calculations When electronic structure calculations are reported in the manuscript, the atomic coordinates of the optimized computational models should be provided. For molecular dynamics trajectories at least the initial and final configurations should be supplied. We encourage you to make them available by uploading the structures in any of the existing data repositories (see e.g. https://www.nature.com/sdata/policies/repositories). Alternatively, they can be supplied as a separate Supplementary Data file (ideally as a plain, unformatted text file).

**Commented [TB62R61]:** We have prepared the detailed file for providing the atomic coordinates of optimized computational models. Additionally, all .fchk and .log files for Time dependent measurement are provided. In this case, reader could readily do similar analysis for estimating charge separation by using as-proposed method.

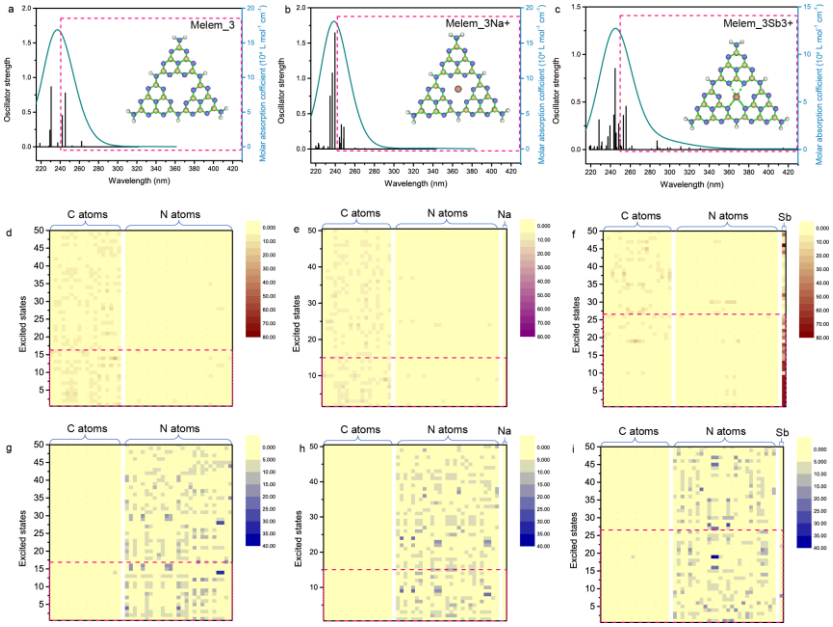


**Supplementary Figure 37 | Simulated excitation properties of Melem_3, Melem_3Na+ and Melem_3Sb3+. a-c**, TDDFT-calculated absorption spectra for (**a**) Melem_3, (**b**) Melem_3Na+ and (**c**) Melem_3Sb3+. **d-i**, The population of electron and hole distribution (vertical excitation at the excited states 1-50). (**d**) Electron distribution and (**g**) hole distribution for Melem_3. (**e**) Electron distribution and (**h**) hole distribution for Melem_3Na+. (**f**) Electron distribution and (**i**) hole distribution for Melem_3Sb3+. The magenta dash circles are the excited states that possibly participate in the photocatalytic $H_2O_2$ production.

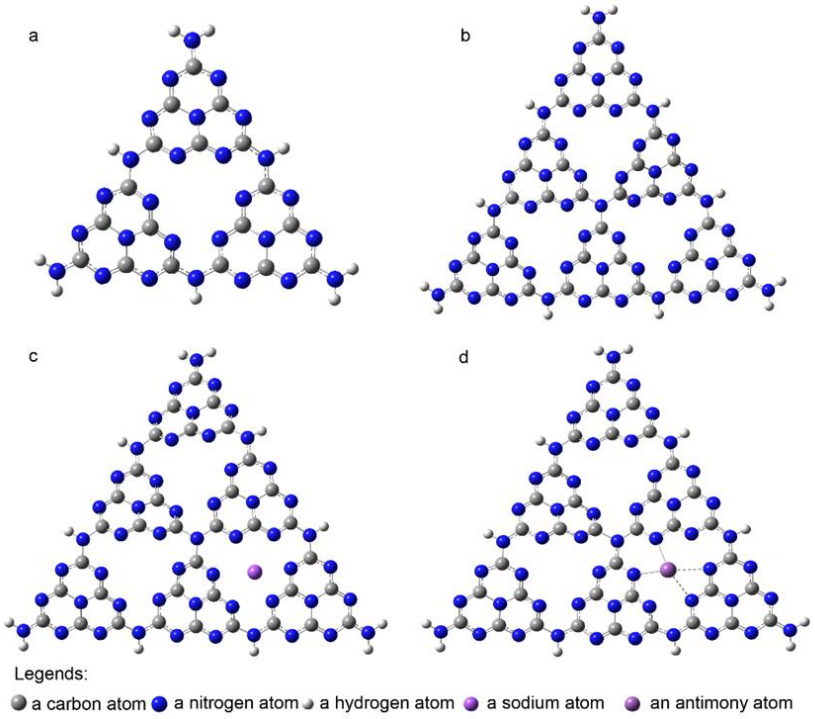


**Supplementary Figure 38 | Cluster models for investigating charge separation properties. a**, A cluster model for representing Melem_3. **b**, Melem_6 for representing PCN. **c**, Melem_6Na+ for representing sodium ion incorporated PCN. **d**, Melem_6Sb3+ for representing single atomic Sb incorporated PCN.

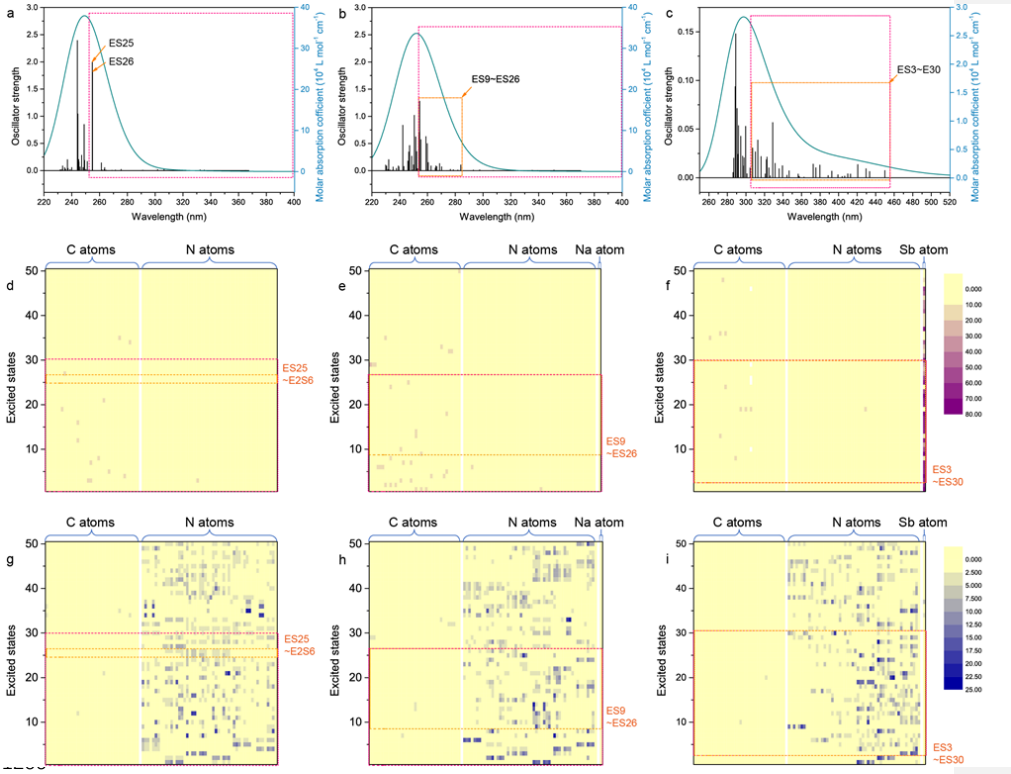


**Supplementary Figure 39 | Simulated excitation properties of Melem_6, Melem_6Na+ and Melem_6Sb3+. a-c**, TDDFT-calculated absorption spectra for (**a**) Melem_6, (**b**) Melem_6Na+ and (**c**) Melem_6Sb3+. **d-i**, The population of electron and hole distribution (vertical excitation at the excited states 1-50). (**d**) Electron distribution and (**g**) hole distribution for Melem_6. (**e**) Electron distribution and (**h**) hole distribution for Melem_6Na+. (**f**) Electron distribution and (**i**) hole distribution for Melem_6Sb3+. The magenta dash circles are the excited states that possibly participate in the photocatalytic $H_2O_2$ production. The orange dash circles represent the most important transitions that contribute the most for the spectra for photocatalytic $H_2O_2$ production.

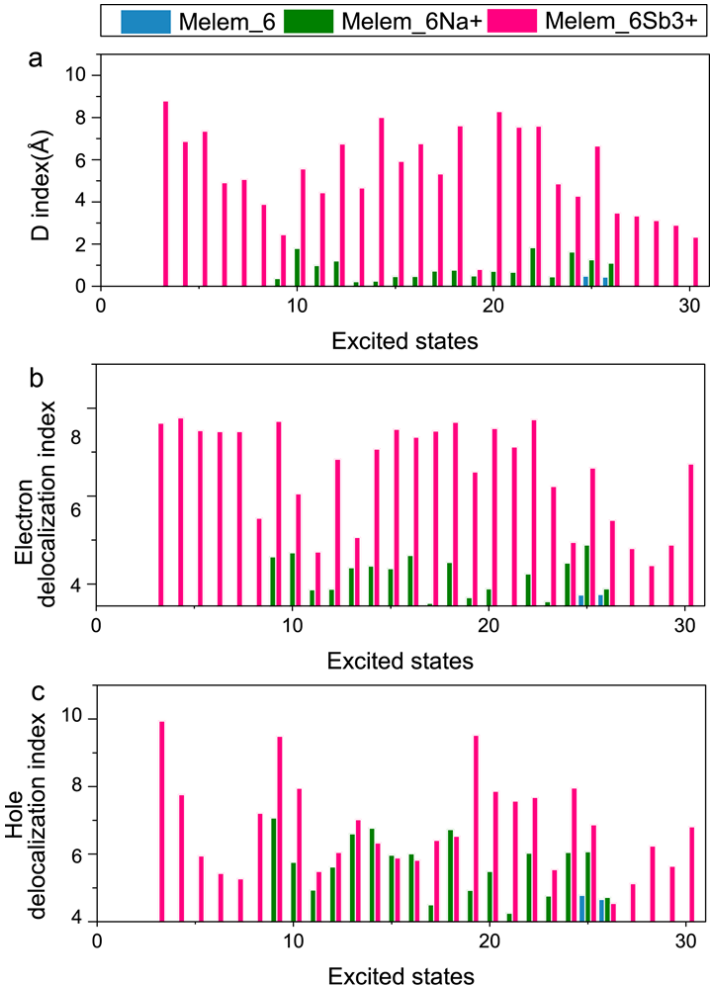


**Supplementary Figure 40 | Simulated properties of Melem_6, Melem_6Na+ and Melem_6Sb3+ for charge separation and the localization of electrons and holes.** ***a****, D index of the transitions of ES25 and ES26 of Melem_6, ES9~ES26 of Melem_6Na+ and ES3~ES30 of Melem_6Sb3+.* ***b-c****, Delocalization index of (****b****) electrons and (****c****) holes for the transitions of ES25 and ES26 of Melem_6, ES9~ES26 of Melem_6Na+ and ES3~ES30 of Melem_6Sb3+.*

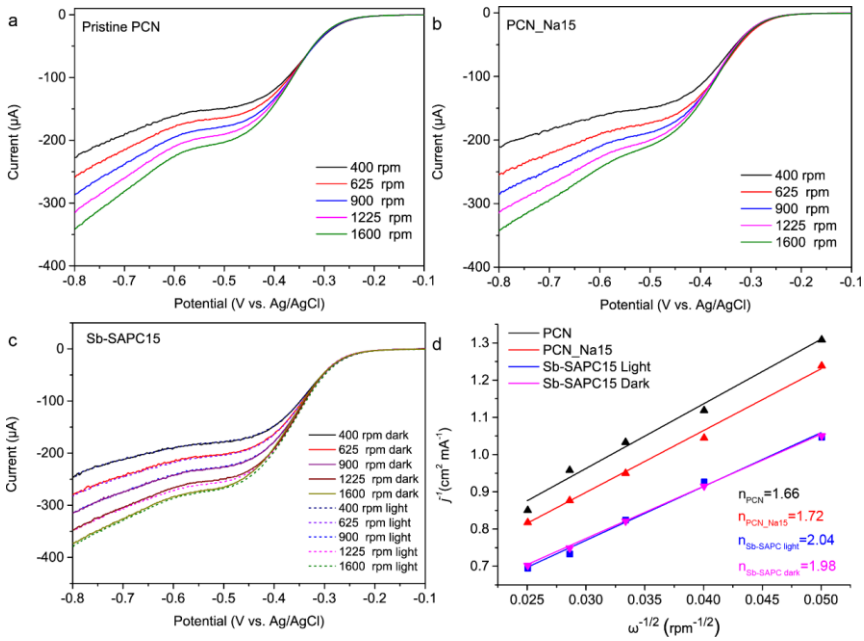


**Supplementary Figure 41 | Investigation of electron transfer numbers. a-b**, Linear sweep voltammetry (LSV) curves of pristine PCN (**a**) and Sb-SAPC15 (**b**) recorded on a rotating disk glassy carbon electrode in 0.1 M KOH saturated with $O_2$ in dark condition. **c**, Linear sweep voltammetry (LSV) curves of Sb-SAPC15 recorded on a rotating disk glassy carbon electrode in 0.1 M KOH saturated with $O_2$ under dark or visible light illumination. **d**, Koutecky−Levich plots (at -0.6 V vs. Ag/AgCl).

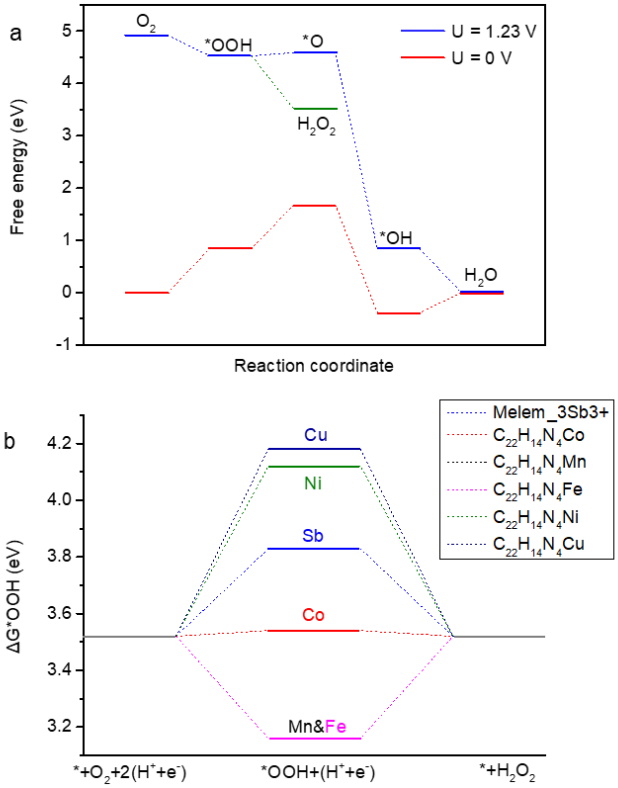


**Supplementary Figure 42 | Energetic diagram for ORR. a**, Calculated free energy diagrams at U = 0 (blue line) and U = 1.23 V (red line) vs. RHE for $2e^-$ (green line) and $4e^-$ ORR on Melem_3Sb3+. **b**, Comparison of $\Delta G_{*OOH}$ for the $2e^-$ ORR on Sb-SAPC15 and $C_{40}H_{16}N_4M$, M = Mn, Fe, Co, Ni, and Cu at U = 0.7 V vs. RHE. The free energy diagram of $C_{40}H_{16}N_4M$ is adopted from our previous report[2].

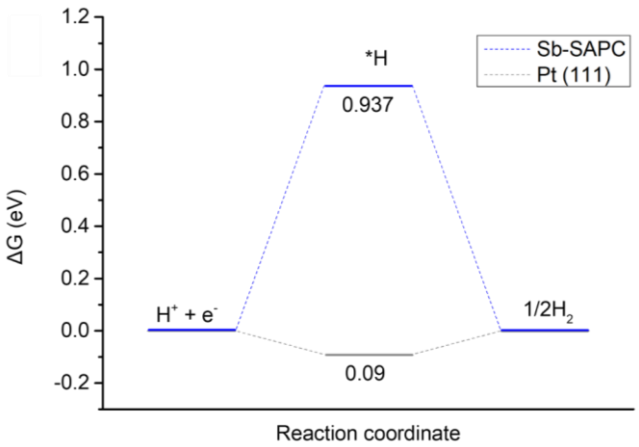


**Supplementary Figure 43 | Interaction of hydrogen atoms and Sb sites and energetic diagram for HER.** Comparison of $\Delta G_{*H}$ for HER on Melem_3Sb3+ and Pt (111).

The interaction of hydrogen atoms and Sb sites is weak for the following reasons: (1) A typical Sb-H bonding exists in $SbH_3$. The oxidation number of Sb in $SbH_3$ is -3, whereas EXAFS fitting data shows that the chemical state of Sb sites in Sb-SAPC is close to +3. Thus, chemical bonding between Sb(+3) in Sb-SAPC and hydrogen is hardly believed. (2) The free energy diagram of Melem_3Sb3+*H is close to 1 eV, indicating that the adsorption of free H is quite hard on the Sb sites.

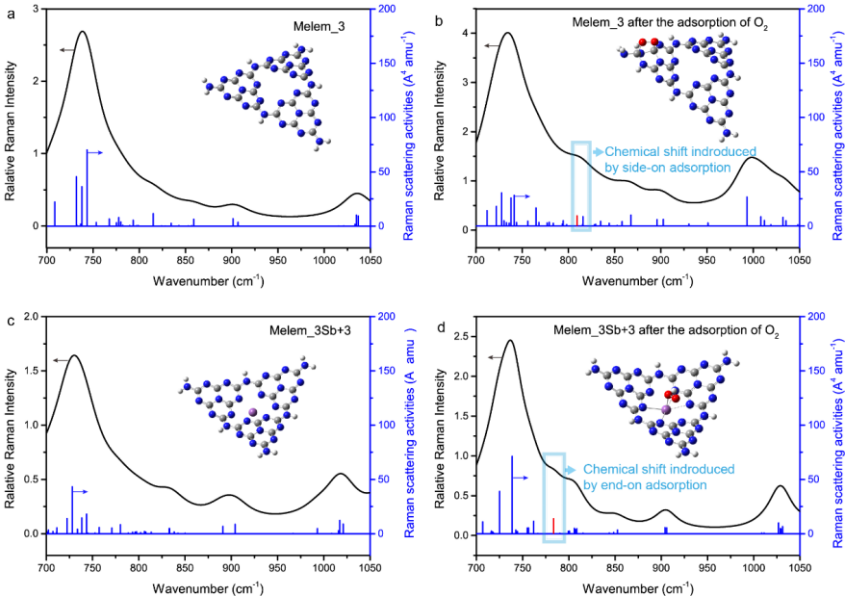


**Supplementary Figure 44 | Calculated Raman shift by using the function of ω97xd at 6-311g(d) level. a-b**, Simulated Raman spectra for (**a**) the tri-s-triazine units and the units with (**b**) $^{16}O–^{16}O$ side-on species. **c-d**, Simulated Raman spectra for (**c**) the Sb-sites and the units with (**d**) $^{16}O–^{16}O$ end-on species. The white, gray, blue, red, and purple spheres represent H, C, N, O and Sb atoms, respectively.

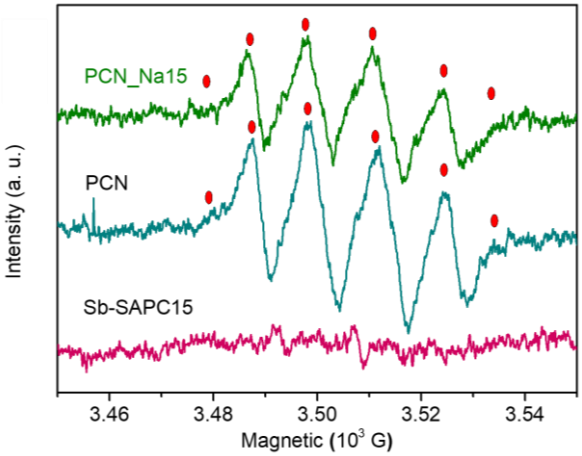


**Supplementary Figure 45 | ESR spectra of PCN, PCN_Na15 and Sb-SAPC15 recorded in methanol solution using 5,5-diemthyl-1-pyrroline N-oxide as a radical trapper.**

**Supplementary Table 1. Activity comparison between Sb-SAPC15 and other reported photocatalysts and photoelectrodes for non-sacrificial $H_2O_2$ production.**

| Photocatalytic system | Concentration of photocatalyst | Irradiation condition | $H_2O_2$ yield | AQE/ SCC efficiency | Ref. |
|---|---|---|---|---|---|
| g-$C_3N_4$/PDIx | 1.7 mg $mL^{-1}$ | λ > 420 nm | 50.6 μmol (48 h) | 2.5% at 420 nm/ NA | [3] |
| g-$C_3N_4$/PDI/RGO | 1.7 mg $mL^{-1}$ | λ > 420 nm | 38 μmol (2 h) | 6.1% at 420 nm/ 0.2% | [4] |
| Graphene oxide | 0.32 mg $mL^{-1}$ | λ > 420 nm | 1.4 μmol (6 h) | NA/ NA | [5] |
| Si/$TiO_2$-Au | ------ | λ = 365 nm | 40 μmol (75 h) | NA/ NA | [6] |
| $TiO_2$-Pt | 0.05 mg $mL^{-1}$ | Full spectrum | 5.096 μmol (1 h) | NA/ NA | [7] |
| g-$C_3N_4$/MTI | 1.7 mg $mL^{-1}$ | λ > 420 nm | 27.5 μmol (24 h) | 6.1% at 420 nm/ 0.18% | [8] |
| g-$C_3N_4$/PDI-BN-RGO | 1.7 mg $mL^{-1}$ | λ > 420 nm | 34 μmol (24 h) | 7.3% at 420 nm/ 0.28% | [9] |
| Resorcinol–formaldehyde resins | 1.7 mg $mL^{-1}$ | λ > 420 nm | 99 μmol (24 h) | 7.5% at 450 nm/ 0.5% | [1] |
| **Sb-SAPC15** | **2 mg $mL^{-1}$** | **λ > 420 nm** | **470.5 μmol (8 h)** | **17.6% at 420 nm/ 0.61%** | **This work** |

**Supplementary Table 2. Mass percentage of Sb in Sb-SAPCx.**

| | Na mass percentage (%) | Substance amount of Na in 1 g catalyst (mmol) | Mass percentage of Sb (%) | Substance amount of Sb in 1 g catalyst (mmol) |
|---|---|---|---|---|
| PCN | 0 | 0.00 | 0 | 0.00 |
| PCN_Na15 | 2.00 | 0.87 | 0 | 0.00 |
| Sb-SAPC0.5 | 0.08 | 0.03 | 0.63 | 0.05 |
| Sb-SAPC1 | 0.16 | 0.07 | 0.96 | 0.08 |
| Sb-SAPC3 | 0.44 | 0.19 | 2.28 | 0.19 |
| Sb-SAPC5 | 0.72 | 0.31 | 4.31 | 0.36 |
| Sb-SAPC10 | 1.18 | 0.51 | 7.85 | 0.65 |
| Sb-SAPC15 | 1.51 | 0.66 | 10.88 | 0.90 |
| PCN_Na15W* | 2.01 | 0.87 | 0 | 0 |
| Sb-SAPC15W* | 1.50 | 0.65 | 10.85 | 0.89 |

* PCN_Na15W and Sb-SAPC15W indicate the samples washed by hot water (90 °C) for another 24 h.

We have tried to wash the as-prepared Sb-SAPC15 by hot water (90 °C) for extremely long time (24 hours) in order to remove the alkaline ions in the CN matrix[10]. However, the ICP result showed that the Na content kept almost constant after this treatment. The difficulty of removing Na in PCN by washing could be due to its existence nature. As revealed in the simulations based on DFT (both cluster model and periodic model), sodium tends to bond onto the matrix of PCN. However, the introduction of Na into PCN only slightly enhanced its photocatalytic activity.

**Supplementary Table 3. Elemental analysis.**

| Sample name | N % | C % | H % | $Mass_C/Mass_N$ |
|---|---|---|---|---|
| PCN | 60.7 | 33.7 | 2.01 | 55.5% |
| PCN_Na15 | 57.5 | 33.1 | 1.70 | 57.5% |
| Sb-SAPC1 | 59.5 | 33.1 | 1.90 | 55.7% |
| Sb-SAPC5 | 56.8 | 31.7 | 1.78 | 55.8% |
| Sb-SAPC10 | 54.0 | 30.3 | 1.66 | 56.2% |
| Sb-SAPC15 | 49.6 | 28.5 | 1.61 | 57.5% |
| Sb-SAPC20 | 45.5 | 26.9 | 1.57 | 59.1% |

**Supplementary Table 4. Fitting parameters of EXAFS data.**

| Sample | Shell | N | R/Å | ΔE | Debye-Waller factor $\sigma^2$ (Å$^2$) | R-factor |
|---|---|---|---|---|---|---|
| $Sb_2O_5$ | Sb-O | 4.2±0.20 | 1.96±0.007 | 7.85±1.04 | 0.003±0.001 | 0.02 |
| Sb-SAPC | Sb-N | 3.3±0.20 | 2.0±0.03 | 9.74±0.94 | 0.002±0.0009 | 0.018 |

Shell: scattering pathway; N: coordination number; R: bond distance; ΔE: the inner potential correction. The obtained XAFS data was processed in Athena (version 0.9.25) for background, pre-edge line and post-edge line calibrations. The data range adopted for data fitting in k-space and R space are 3-11.5 Å$^{-1}$ and 1-3 Å, respectively.

**Supplementary Table 5. Excitation properties based on the wavefunctions of Melem_3.**

| | Molecule orbital contribution (Hole) | | | Molecule orbital contribution (Electron) | | | | Molecule orbital contribution (Hole) | | | Molecule orbital contribution (Electron) | | |
|---|---|---|---|---|---|---|---|---|---|---|---|---|---|
| | MO | 151 | 14.071% | MO | 154 | 68.397% | | MO | 138 | 16.530% | MO | 154 | 51.954% |
| S0→S1 | MO | 152 | 27.839% | MO | 155 | 14.459% | S0→S9 | MO | 143 | 22.826% | MO | 155 | 17.193% |
| | MO | 153 | 50.968% | MO | 157 | 6.912% | | MO | 145 | 9.484% | MO | 156 | 8.394% |
| | MO | 151 | 28.569% | MO | 154 | 18.080% | | MO | 137 | 19.313% | MO | 154 | 29.615% |
| S0→S2 | MO | 152 | 15.441% | MO | 155 | 62.993% | S0→S10 | MO | 138 | 11.299% | MO | 155 | 37.942% |
| | MO | 153 | 48.866% | MO | 157 | 9.812% | | MO | 150 | 11.187% | MO | 160 | 7.391% |
| | MO | 151 | 37.218% | MO | 154 | 37.462% | | MO | 151 | 36.625% | MO | 154 | 33.124% |
| S0→S3 | MO | 152 | 37.269% | MO | 155 | 37.027% | S0→S11 | MO | 152 | 15.992% | MO | 155 | 14.635% |
| | MO | 153 | 17.695% | MO | 157 | 13.292% | | MO | 153 | 26.999% | MO | 156 | 27.816% |
| | MO | 150 | 47.527% | MO | 154 | 20.177% | | MO | 151 | 3.065% | MO | 155 | 34.473% |
| S0→S4 | MO | 151 | 8.132% | MO | 155 | 57.173% | S0→S12 | MO | 152 | 34.192% | MO | 156 | 33.596% |
| | MO | 152 | 9.408% | MO | 156 | 11.088% | | MO | 153 | 35.353% | MO | 162 | 11.681% |
| | MO | 146 | 16.036% | MO | 154 | 39.300% | | MO | 151 | 26.303% | MO | 154 | 23.953% |
| S0→S5 | MO | 149 | 15.260% | MO | 155 | 32.108% | S0→S13 | MO | 152 | 7.807% | MO | 155 | 18.083% |
| | MO | 150 | 20.259% | MO | 156 | 10.911% | | MO | 153 | 40.502% | MO | 156 | 36.970% |
| | MO | 146 | 7.248% | MO | 154 | 44.219% | | MO | 138 | 22.850% | MO | 154 | 44.924% |
| S0→S6 | MO | 148 | 33.220% | MO | 155 | 23.903% | S0→S14 | MO | 141 | 33.109% | MO | 157 | 12.639% |
| | MO | 149 | 13.611% | MO | 157 | 7.874% | | MO | 142 | 18.279% | MO | 158 | 29.103% |
| | MO | 136 | 13.136% | MO | 154 | 37.571% | | MO | 140 | 22.905% | MO | 154 | 16.970% |
| S0→S7 | MO | 143 | 6.749% | MO | 155 | 28.780% | S0→S15 | MO | 142 | 26.607% | MO | 155 | 33.323% |
| | MO | 150 | 30.250% | MO | 160 | 7.516% | | MO | 152 | 8.676% | MO | 157 | 21.247% |
| | MO | 136 | 13.859% | MO | 154 | 40.885% | | MO | 140 | 33.930% | MO | 155 | 33.086% |
| S0→S8 | MO | 137 | 17.967% | MO | 155 | 29.284% | S0→S16 | MO | 141 | 24.611% | MO | 157 | 28.433% |
| | MO | 138 | 10.097% | MO | 160 | 9.744% | | MO | 142 | 6.556% | MO | 159 | 15.597% |

**Supplementary Table 6. Excitation properties based on the wavefunctions of Melem_3Na+.**

| | Molecule orbital contribution (Hole) | | | Molecule orbital contribution (Electron) | | | | Molecule orbital contribution (Hole) | | | Molecule orbital contribution (Electron) | | |
|---|---|---|---|---|---|---|---|---|---|---|---|---|---|
| | MO | 156 | 16.370% | MO | 159 | 50.714% | | MO | 150 | 16.143% | MO | 159 | 32.219% |
| S0→S1 | MO | 157 | 28.906% | MO | 160 | 28.431% | S0→S9 | MO | 151 | 14.245% | MO | 160 | 18.088% |
| | MO | 158 | 47.236% | MO | 165 | 9.882% | | MO | 152 | 23.079% | MO | 162 | 16.494% |
| | MO | 156 | 28.665% | MO | 159 | 28.572% | | MO | 150 | 17.206% | MO | 159 | 24.905% |
| S0→S2 | MO | 157 | 16.793% | MO | 160 | 50.573% | S0→S10 | MO | 151 | 17.064% | MO | 160 | 22.652% |
| | MO | 158 | 47.059% | MO | 165 | 9.935% | | MO | 152 | 15.489% | MO | 165 | 17.995% |
| | MO | 156 | 38.540% | MO | 159 | 36.710% | | MO | 151 | 19.316% | MO | 154 | 33.124% |
| S0→S3 | MO | 157 | 37.923% | MO | 160 | 37.005% | S0→S11 | MO | 152 | 19.447% | MO | 155 | 33.136% |
| | MO | 158 | 16.787% | MO | 165 | 13.014% | | MO | 153 | 8.630% | MO | 156 | 14.383% |
| | MO | 147 | 15.135% | MO | 159 | 37.061% | | MO | 143 | 9.834% | MO | 159 | 28.788% |
| S0→S4 | MO | 148 | 15.314% | MO | 160 | 37.519% | S0→S12 | MO | 157 | 18.907% | MO | 160 | 27.355% |
| | MO | 151 | 8.723% | MO | 161 | 13.147% | | MO | 158 | 10.371% | MO | 161 | 18.108% |
| | MO | 148 | 13.833% | MO | 159 | 24.221% | | MO | 142 | 9.828% | MO | 159 | 27.347% |
| S0→S5 | MO | 149 | 20.893% | MO | 160 | 48.620% | S0→S13 | MO | 156 | 18.948% | MO | 160 | 28.782% |
| | MO | 152 | 12.584% | MO | 161 | 10.043% | | MO | 158 | 10.349% | MO | 161 | 18.116% |
| | MO | 147 | 14.340% | MO | 159 | 49.006% | | MO | 141 | 10.630% | MO | 159 | 28.119% |
| S0→S6 | MO | 149 | 20.718% | MO | 160 | 23.845% | S0→S14 | MO | 141 | 18.961% | MO | 160 | 28.836% |
| | MO | 152 | 12.348% | MO | 161 | 10.014% | | MO | 142 | 16.524% | MO | 161 | 16.263% |
| | MO | 145 | 15.746% | MO | 159 | 28.623% | | MO | 141 | 10.658% | MO | 159 | 28.819% |
| S0→S7 | MO | 146 | 15.655% | MO | 160 | 28.829% | S0→S15 | MO | 156 | 18.931% | MO | 160 | 28.102% |
| | MO | 158 | 15.053% | MO | 162 | 10.142% | | MO | 158 | 16.474% | MO | 161 | 16.249% |
| | MO | 150 | 14.208% | MO | 159 | 16.990% | | | | | | | |
| S0→S8 | MO | 151 | 15.924% | MO | 160 | 33.282% | | | | | | | |
| | MO | 152 | 23.405% | MO | 162 | 16.511% | | | | | | | |

**Supplementary Table 7. Excitation properties based on the wavefunctions of Melem_3Sb3+.**

| | Molecule orbital contribution (Hole) | | | Molecule orbital contribution (Electron) | | | | Molecule orbital contribution (Hole) | | | Molecule orbital contribution (Electron) | | |
|---|---|---|---|---|---|---|---|---|---|---|---|---|---|
| | MO | 149 | 3.633% | MO | 155 | **99.112%** | | MO | 146 | 37.096% | MO | 155 | **40.942%** |
| S0→S1 | MO | 151 | 65.610% | | | | S0→S14 | MO | 153 | 11.569% | MO | 156 | 27.918% |
| | MO | 154 | 19.339% | | | | | MO | 154 | 11.569% | MO | 157 | 10.666% |
| | MO | 149 | 17.637% | MO | 155 | **98.594%** | | MO | 141 | 11.460% | MO | 155 | **37.232%** |
| S0→S2 | MO | 151 | 13.214% | | | | S0→S15 | MO | 151 | 23.242% | MO | 156 | 20.075% |
| | MO | 154 | 50.549% | | | | | MO | 154 | 12.858% | MO | 157 | 27.434% |
| | MO | 150 | 12.440% | MO | 155 | **98.773%** | | MO | 147 | 10.948% | MO | 155 | **64.773%** |
| S0→S3 | MO | 152 | 17.901% | | | | S0→S16 | MO | 148 | 37.814% | MO | 156 | 6.228% |
| | MO | 153 | 54.845% | | | | | MO | 151 | 13.782% | MO | 157 | 17.977% |
| | MO | 144 | 7.421% | MO | 155 | **99.225%** | | MO | 146 | 20.726% | MO | 155 | **44.139%** |
| S0→S4 | MO | 150 | 32.476% | | | | S0→S17 | MO | 151 | 11.805% | MO | 156 | 27.976% |
| | MO | 153 | 36.790% | | | | | MO | 153 | 11.062% | MO | 157 | 10.670% |
| | MO | 141 | 32.952% | MO | 155 | **98.441%** | | MO | 141 | 18.967% | MO | 155 | **77.536%** |
| S0→S5 | MO | 145 | 32.842% | | | | S0→S18 | MO | 142 | 35.504% | MO | 156 | 5.924% |
| | MO | 154 | 22.604% | | | | | MO | 147 | 20.012% | MO | 157 | 4.105% |
| | MO | 143 | 12.371% | MO | 155 | **98.625%** | | MO | 147 | 10.237% | MO | 157 | 55.007% |
| S0→S6 | MO | 150 | 11.062% | | | | S0→S19 | MO | 148 | 83.253% | MO | 163 | 5.986% |
| | MO | 152 | 61.864% | | | | | | | | MO | 164 | 20.416% |
| | MO | 141 | 9.700% | MO | 155 | **95.897%** | | MO | 139 | 14.951% | MO | 155 | **49.783%** |
| S0→S7 | MO | 145 | 31.267% | | | | S0→S20 | MO | 146 | 25.432% | MO | 156 | 20.017% |
| | MO | 149 | 34.516% | | | | | MO | 147 | 23.178% | MO | 157 | 6.417% |
| | MO | 139 | 7.962% | MO | 155 | **97.100%** | | MO | 146 | 36.714% | MO | 155 | **21.729%** |
| S0→S8 | MO | 143 | 23.509% | | | | S0→S21 | MO | 147 | 41.974% | MO | 156 | 31.893% |
| | MO | 144 | 49.833% | | | | | MO | 148 | 4.249% | MO | 157 | 14.042% |
| | MO | 143 | 37.403% | MO | 155 | **98.014%** | | MO | 139 | 16.928% | MO | 155 | **64.457%** |
| S0→S9 | MO | 144 | 28.745% | | | | S0→S22 | MO | 140 | 24.402% | MO | 156 | 15.844% |
| | MO | 150 | 14.566% | | | | | MO | 146 | 21.073% | MO | 157 | 5.920% |
| | MO | 152 | 9.902% | MO | 155 | 8.267% | | MO | 145 | 19.544% | MO | 155 | **29.565%** |
| S0→S10 | MO | 153 | 22.497% | MO | 156 | 26.006% | S0→S23 | MO | 151 | 8.865% | MO | 156 | 28.095% |
| | MO | 154 | 42.826% | MO | 157 | 43.742% | | MO | 152 | 16.424% | MO | 157 | 11.023% |
| | MO | 145 | 12.654% | MO | 155 | **86.894%** | | MO | 138 | 38.207% | MO | 155 | **47.750%** |
| S0→S11 | MO | 148 | 41.191% | MO | 156 | 4.160% | S0→S24 | MO | 153 | 8.226% | MO | 156 | 12.316% |
| | MO | 149 | 16.773% | MO | 157 | 2.632% | | MO | 154 | 8.707% | MO | 157 | 17.450% |
| | MO | 142 | 38.982% | MO | 155 | **84.579%** | | MO | 146 | 21.944% | MO | 155 | **19.032%** |
| S0→S12 | MO | 146 | 6.215% | MO | 156 | 5.009% | S0→S25 | MO | 147 | 24.951% | MO | 156 | 12.536% |
| | MO | 147 | 43.746% | MO | 162 | 2.747% | | MO | 148 | 15.529% | MO | 157 | 27.791% |
| | MO | 139 | 20.544% | MO | 155 | **87.222%** | | MO | 137 | 21.180% | MO | 155 | **22.031%** |
| S0→S13 | MO | 140 | 27.510% | MO | 156 | 4.259% | S0→S26 | MO | 146 | 35.194% | MO | 158 | 20.115% |
| | MO | 146 | 19.057% | MO | 157 | 2.552% | | MO | 147 | 22.580% | MO | 165 | 14.447% |

It is noteworthy that the absorption edge of simulated UV spectra as well as computed optical gaps are usually larger than the experimental band gaps because of the following two reasons: (1) To simulate the charge-transfer properties of the model with high qualities, function of ω97xd, a function including large amount of Hartree–Fock exchange, was used. These exchange functions usually overestimate the excitation energies, as well as the simulated HOMO-LUMO gap; (2) In the solid state, p-conjugated molecules adjacent to the one carrying a charge strongly polarize, an effect that stabilizes the cationic and anionic states (each generally by about one eV in p-conjugated materials). In this case, the experimental band gap is typically considerably smaller in energy than the calculated molecular fundamental gap, as well as the calculated optical gap[11]. Since the system error cannot be eliminated, the possible simulated ES that contributed to $H_2O_2$ production (corresponding to the spectra from 420 nm – 470 nm) were confirmed by comparing the experimental spectra and simulated ones. Then, the transition density of electron/holes was considered at all these ES.

**Supplementary Table 8. Initial and optimized configuration for investigating the side-on adsorption of $O_2$ on PCN surface.**

| | Side-on adsorption of $O_2$ on Melem_3 (Site 1) | | Side-on adsorption of $O_2$ on Melem_3 (Site 2) | |
|---|---|---|---|---|
| | Top view | Side view | Top view | Side view |
| Before optimization |  | 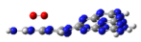 | 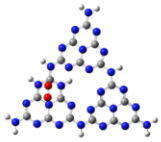 | 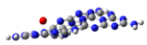 |
| After optimization |  | 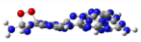 | 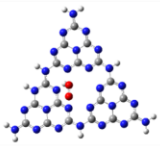 | 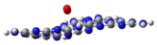 |

**Supplementary Notes 1: Probing WOR and ORR with low-concentration electron acceptor**

To calculate the $H_2O_2$ generated from the Sb-SAPC system, we made the following assumptions: (1) all added $Ag^+$ (4n mol) is consumed to provide holes to generate the initial $O_2$ (n mol); (2) then, the Sb-SAPC reduces $O_2$ (n mol) to form $H_2O_2$ (n mol) and simultaneously oxidizes $H_2O$ (n mol) to generate fresh $O_2$ (1/2n mol); (3) the $O_2$ generated in (2) keeps participating in the $H_2O_2$ production and WOR to generate $O_2$ (1/4n, 1/8n, 1/16n… mol) until all $O_2$ is completely consumed. As a result, the amount of $H_2O_2$ produced by the initially generated $O_2$ can be calculated as follows:

$$n_{H_2O_2} = \sum_{k=1}^{x} n_{O_2} r^{k-1} = \frac{n_{O_2}(1-r^x)}{1-r} \quad (1)$$

where $n_{H_2O_2}$ is the generated amount of $H_2O_2$, $n_{O_2}$ is the amount of generated $O_2$ by $Ag^+$, $r$ is 1/2, *k* is number of reaction cycles for simultaneous $H_2O_2$ production and WOR. If the initial $O_2$ generated by $Ag^+$ (*k* = 1) was all consumed for $H_2O_2$ production (i.e., *k* equals to ∞), the total amount of $H_2O_2$ produced would be 2 times the amount of $O_2$ (*k* = 1) and 1/2 times the amount of added $Ag^+$. The constant concentration of $H_2O_2$ was measured to be 0.032 mM with addition of 200 mg catalyst, 64% of the ideal value (0.05 mM) calculated based on the initially added $Ag^+$ (0.1 mM). The 36% deficiency of $H_2O_2$ could be due to the reaction equilibrium of $H_2O_2$ production[9,12] and the dissolved $O_2$ in aqueous solution ($O_2$ solubility in pure water: 0.25 mM).

**Supplementary Notes 2: Investigation of synthesis process of Sb-SAPC**

The synthesis of Sb-SAPC was first investigated to give a view of the structure of Sb-SAPC. Sb-ethoxide was formed after dissolving $NaSbF_6$ in ethanol. After addition of melamine, the lattice distance of the Sb-containing mixture was slightly increased. The formed Sb-containing compound can be assigned to the Sb-melamine, verified by X-ray diffraction (XRD, Supplementary Figure 13a) and X-ray photoelectron spectroscopy (XPS, Supplementary Figures 14-15). Then, thermal polymerization and removal of F element were performed by calcination at 560 °C for 4 hours (Supplementary Figure 16).

The calcination temperature was also investigated. Sb-SAPC5 (5 mmol of $NaSbF_6$

**Commented [TB63]:** Please remove this numbering and integrated it into "Supplementary Note 1" etc..

**Commented [TB64R63]:** All numbering has been removed and integrated them into the "Supplementary Notes"

**Commented [TB65]:** * Please number ALL Supplementary Equations sequentially as 1, 2, etc. – If mentioned in the text refer to them as "Supplementary Equation X" not "Equation X".

**Commented [TB66R65]:** We have numbered all Supplementary Equations sequentially.
All of the Equations in the test has been revised to "Supplementary Equation X"

mixed with 4 g of melamine were used as the precursor) was prepared at 520 °C and 560 °C (named as Sb-SAPC5_520 and Sb-SAPC5_560), respectively. As shown in Supplementary Figure 17a, the inner-panel diffraction of the (100) lattice completely disappears in Sb-SAPC5_520, and the inter-panel diffraction of PCN (002) lattice is also significantly decreased in Sb-SAPC5_560, while the crystalline structure of graphitic carbon nitride maintains. Additionally, the F element cannot be completely eliminated by heating at 520 °C, as shown in the XPS measurement (Supplementary Figure 17b). These results imply that low calcination temperature cannot remove the F element in the PCN matrix, leading to an incomplete polymerization of the graphitic carbon nitride[13]. Additionally, the Sb-SAPC5_520 shows much poorer photocatalytic activity toward $H_2O_2$ production, even worse than the pristine PCN (Supplementary Figure 17c). Therefore, Sb-SAPCs prepared at 560 °C were used for further photocatalytic investigation.

**Supplementary Notes 3: Structure characterization**

The crystalline structures of the as-prepared samples were examined by XRD and HRTEM. XRD patterns of all Sb-SAPC samples show two characteristic peaks at about 27.6° and 13.1° (Supplementary Figure 19), which can be ascribed to the interlayer stacking (002) and the inter planar structure packing (100) of tri-s-triazine units, respectively[14]. The slight shift in the diffraction angle of the (002) peak for Sb-SAPC15 can be attributed to the electrostatic repulsion between interlayers when positive ions are incorporated into the PCN matrix. The intensities of these two peaks gradually decrease when increasing the contents of precursors (Supplementary Figure 19c), indicating that polymeric structure of melon/g-$C_3N_4$ could be slightly influenced by the foreign ions[15]. Although the long-range order of the (002) and (100) lattices significantly decreases, these two lattices can still be observed even when the content of ions reaches as high as 20 mmol. To further investigate whether the pristine structure is changed after the ion incorporation, high-resolution TEM measurements of the exfoliated Sb-SAPC were conducted (as shown in Supplementary Figure 20). The (100) inter planar structure packing of the tri-s-triazine units can be readily observed, and the lattice distance is determined to be 6.81 Å, which is in accordance with the XRD results. Thus, the crystalline

structure of melon can be well preserved in Sb-SAPC.

**Supplementary Notes 4: Influence of the -C≡N group**

FT-IR (Supplementary Figure 24a) and XPS measurements reveal the existence of -C≡N groups in both PCN_Na15 and Sb-SAPC15. The interrelationship between -C≡N groups and cations in carbon nitride matrix was investigated. As shown in Supplementary Figure 24a, the absorption band around the wavenumber of 2180 $cm^{-1}$ in the spectrum of PCN_Na15 is slightly stronger than that in the spectrum of Sb-SAPC15, manifesting the larger content of -C≡N groups in PCN_Na15. To investigate the influence of the cation content on the formation of -C≡N groups, ICP measurements were performed. As shown in Supplementary Table 2, the Na amount in PCN_Na15 (0.87 mmol per gram) and Sb-SAPC15 (0.66 mmol per gram) are close, while PCN_Na15 contains no Sb species. Additionally, the ratios of the integration areas from the deconvoluted peaks at 288.1 and 286.5 eV are similar in the high-resolution XPS spectra of PCN_Na15 (0.268) and Sb-SAPC15 (0.228). These results indicate that the introduction of Sb sites into PCN has little influence on the formation of -C≡N groups, and the -C≡N group formation could be possibly due to the incorporation of alkaline metal ions[10]. These results are also in accordance with the proposed synthesis mechanism (Supplementary Figure 1) and the EXAFS fitting results.

Several studies have reported that the -C≡N is an electron-withdrawing group that may significantly enhance the charge separation, and thus improve the photocatalytic activity[10, 15-17]. To clarify the influence of -C≡N groups and Sb species on charge separation and photocatalytic activity, a comprehensive investigation has to be carried out by comparing the photocatalytic performance of Sb-SAPC15 and PCN_Na15. As clarified in the previous paragraph, the Na ion content in Sb-SAPC15 is similar to that in PCN_Na15, giving a similar -C≡N content. But Sb-SAPC15 exhibits a much higher photocatalytic activity (Figure 1c and Supplementary Figure 9b), suggesting the crucial function of the Sb species for photocatalysis. Additionally, the photoluminescence intensity of PCN_Na15 (Supplementary Figure 31a) is weaker as compared to that of pristine PCN, indicating that the charge recombination can be effectively suppressed by introducing the -C≡N groups.

In the case of Sb-SAPC15, the introduction of Sb species can further decrease the photoluminescence intensity, manifesting that the radiative recombination is suppressed. The TRPL spectrum also shows the similar phenomenon, i.e. lifetime of the charge carriers in Sb-SAPC15 (0.428 ns) is shorter than that in PCN_Na15 (1.41 ns), indicating that non-radiative recombination is facilitated in Sb-SAPC15.

**Supplementary Notes 5: Post characterization and investigation for catalyst poisoning**

The HAADF STEM image of Sb-SAPC15 after 5 days of photoreaction shows that the Sb sites remain atomically dispersed (Supplementary Figure 29a). The UV-vis spectra show that the light absorption property of Sb-SAPC15 was hardly influenced by the continuous photoreaction (Supplementary Figure 29b). The XRD pattern indicates that the crystallinity of Sb-SAPC15 hardly changed after 5 days of photoreaction. Note that both diffractions at 13.1° and 27.4° are clearly observable, indicating that the PCN structure in Sb-SAPC15 was well maintained after long-term photoreaction (Supplementary Figure 29c). High-resolution N 1s, C 1s, O 1s and Sb 3d XPS spectra show that the chemical states of N, C, O and Sb on the surface of Sb-SAPC15 were hardly influenced by the long-time photoreaction (Supplementary Figure 29d-f). The surface oxidation of CN and Sb were not observed. All of the above results demonstrate the excellent photocatalytic stability of Sb-SAPC15.

The maximum $H_2O_2$ concentration after 8 h of photocatalytic reaction is approximately 0.016 wt.% of $H_2O_2$. Thus to further investigate whether catalyst poisoning occurred on the surface of the catalyst, the photocatalytic activity was measured after soaking the as-prepared Sb-SAPC15 catalyst in different concentrations of $H_2O_2$ solution (ranging from 0.01 wt.% to 1 wt.%) for 8 h. The photocatalytic activity of Sb-SAPC15 showed no obvious decay after being soaked in different concentrations of $H_2O_2$ solution for 8 h. This result indicates insignificant catalyst poisoning during our photocatalytic $H_2O_2$ production process.

**Supplementary Notes 6: Optical properties and action spectra**

As shown in the insert to Supplementary Figure 30a, Sb-SAPC15 displays a deep

yellow color, darker than the pale yellow color of pristine PCN and PCN_Na15. To determine the precise band positions of these samples, UV-vis spectroscopy, Mott-Schottky and valence band XPS measurements were conducted to obtain the bandgap width, CBM and VBM, respectively. As shown in Supplementary Figure 30a-b, the light absorption ($\lambda$ < 450 nm) of Sb-SAPC15 significantly enhances compared with that of PCN_Na15 and pristine PCN, possibly due to changes in electronic states resulted from Sb incorporation. Tauc plots of pristine PCN, PCN_Na15 and Sb-SAPC15 indicate that the bandgap almost keeps constant after introducing Sb and/or Na ions. VB-XPS results show that the VBM of PCN_Na15 and Sb-SAPC15 keep almost the same (~1.45 eV) to that of PCN (Supplementary Figure 30c). Mott-Schottky plots reveal that the CBM slightly become more positive from pristine PCN to PCN_Na15 and to Sb-SAPC15 (Supplementary Figure 30d-f). By summarizing these results for band positions, we draw the band position diagrams of these samples, as shown in Supplementary Figure 30g.

The action spectra of Sb-SAPC15 (Figure 1c) show that the apparent quantum yield (ΦAQY) agrees well with the absorption spectrum (Supplementary Figure 30a). The absorption in the wavelength larger than 500 nm of Sb-SAPC15 could not contribute to the production of $H_2O_2$. These results show that the VB-to-CB excitation of Sb-SAPC15 is responsible for the $H_2O_2$ production.

**Supplementary Notes 7: Verification of WOR mechanism**

OER occurred in our photocatalytic system for the following reasons:

1) We have checked the water oxidation reaction by adding the electron acceptor of $NaIO_3$ to make sure whether molecular oxygen could indeed be produced. As shown in Figure 1f, oxygen was gradually generated in the system of Sb-SAPC15, while neither $O_2$ nor $H_2O_2$ could be detected in the system of pristine PCN and PCN_Na15.

2) We have observed that the deeply trapped electrons (at 5000 $cm^{-1}$) in Sb-SAPC15 were significantly decelerated by TR-IR after addition of 20 Torr water (Figure 3b). This result indicates that the photogenerated holes were consumed by water oxidation reaction so that the lifetime of photogenerated electrons was significantly prolonged. In the case of PCN and PCN_Na15, the lifetime of photogenerated electrons kept almost the same

(PCN_Na15) or even decreased after addition of water into the system, indicating that the photogenerated holes could barely participate in the water oxidation reaction. These results confirm that the activity of water oxidation for Sb-SAPC is significantly higher than that for PCN or PCN_Na15.

3) To further investigate the oxygen evolution reaction (OER), rotating ring-disk electrode measurement was conducted. The anodic polarization curves of the rotating ring-disk electrode modified by PCN, PCN_Na15 and Sb-SAPC15 were recorded. As shown in Supplementary Figure 34a, the disk current of the electrode modified by Sb-SAPC15 is significantly larger than that of the electrode modified by PCN or PCN_Na15, indicating that the rate of the oxidation reaction taking place on the surface of Sb-SAPC15 is faster than that on PCN and PCN_Na15 (Supplementary Figure 34b). More importantly, clear signals of $O_2$ reduction to $H_2O$ were detected by the ring electrode in both cases of Sb-SAPC15 with or without light irradiation, verifying $O_2$ generation on the Sb-SAPC15 surface via WOR (Supplementary Figure 34c). Moreover, the ring current of the electrode modified by Sb-SAPC15 under light irradiation is obviously larger than that in the dark condition, indicating that photo-induced holes indeed facilitated the WOR. Furthermore, the anodic current on the ring electrode under light irradiation appeared much earlier than that in the dark condition, which also manifested that the photogenerated holes participated in the OER (Supplementary Figure 34d). Therefore, the highly active photo-generated holes boosted the OER via the WOR pathway in the Sb-SAPC15 system.

The water oxidation reaction took place on N atoms of carbon nitride, rather than on the Sb atoms, because of the following reasons:

1) Photocatalytic reaction occurs on the surface of a photocatalyst. The excitation properties on the surface of photocatalysts have been widely investigated by the cluster models, such as N-doped $TiO_2$[18] and $In_2O_3$[19]. The excitation can be systematically discussed by combining the simulated UV-vis spectra and transition densities of charge carriers. As shown in Supplementary Figure 37a-c, the shape of the computed UV-vis absorption spectrum is almost the same as that obtained experimentally, especially in the wavelength between 420 nm and 470 nm. To give a comprehensive understanding of the transition densities of electrons/holes for boosting the $H_2O_2$ production, all transition

densities of the 50 excited states (ES) were summarized in Supplementary Figure 37d-i. Electrons are mostly distributed at the C atoms and Sb atoms, while holes are mostly distributed at the N sites. To further investigate the excitations that contribute to photocatalytic $H_2O_2$ production, the exited states 1-16 of Melem_3, ES 1-15 of Melem_3Na+ and ES 1-26 of Melem_3Sb3+ were highlighted in these figures. On the one hand, most of electrons are accumulated at the Sb sites (ES 1-26) of Melem_3Sb3+ with high density (~20-80%), while most of states show averagely distributed electrons at the C sites (< mostly 20%) in the cluster model of Melem_3 and Melem_3Na+. On the other hand, holes are distributed at the N atoms on Melem_3Sb3+, Melem_3 and Melem_3Na+.

The boundary effect of small cluster models in Supplementary Figure 37 confined the distance of possible separated charges. To give a comprehensive assessment of charge separation by TDDFT simulation, we built larger models to represent pristine PCN (Melem_6), sodium incorporated PCN (Melem_6Na+) and single atomic Sb incorporated PCN (Melem_6Sb3+) to simulate the properties of charge separation (Supplementary Figure 38). Based on the action spectra and the photocatalytic $H_2O_2$ production activities, the ES 1-26 of Melem_6, the ES 1-26 of Melem_6Na+ and the ES 3-30 of Melem_6Sb3+ are highlighted in the distribution heatmap of photogenerated electrons and holes (Supplementary Figure 39d-i). It is confirm that most of the electrons are accumulated at the Sb sites (ES 3-30, Melem_6Sb3+), a ligand-to-metal charge transfer from neighboring melem units to Sb, while most of the states (ES 1-26 for Melem_6 and Melem_6Na+) show averagely distributed electrons at the C sites. The photogenerated electrons and holes barely locate at the Na atoms, indicating that the coordinated Na species on the catalyst's surface unlikely serve as the active sites for the photocatalytic reaction. The above results from Melem_6, Melem_6Na+ and Melem_6Sb3+ give almost the same electronic configurations as the results from Melem_3, Melem_3Na+ and Melem_3Sb3+ (Supplementary Figure 37d-i).

To investigate the properties of charge separation in these three models, the most important transitions that can participate in the photocatalytic $H_2O_2$ production were figured out by checking the osillator strength of each transition in the UV spectra (as shown in the orange dash circles; i. e., the transitions of ES25 and ES26 of Melem_6, ES9~ES26 of

Melem_6Na+ and ES3~ES30 of Melem_6Sb3+)[19]. We then calculated the distance between centroid of hole and electron (D index) in these transitions. This D index was defined followed by the Manual of the Multiwfn[20,21], which could reveal whether charge separation of photogenerated electron hole pair is efficient. As shown in Supplementary Figure 40a, all of the D index of the transitions of Melem_6Sb3+ (ES3~ES30) are significantly larger than that of Melem_6 (ES25 and ES26) and Melem_6Na+ (ES9~ES26), indicating that the charge separation is significantly boosted after the introduction of atomic antimony sites.

Additionally, another crucial property of photogenerated positive charge carriers (photogenerated holes or positive polarons) for facilitating WOR is their high localization levels. To simulate the localization level of photogenerated electrons and holes, we calculated the hole delocalization index (HDI) and electron delocalization index (EDI) [20,21] as defined below:

$$HDI = 100 \times \sqrt{\int [\rho^{hole}(r)]^2 \, dr} \quad (2)$$

$$EDI = 100 \times \sqrt{\int [\rho^{ele}(r)]^2 \, dr} \quad (3)$$

$\rho^{hole}$ and $\rho^{ele}$ respectively indicate the distribution density of holes and electrons [20,21]. It is found that the smaller the HDI (EDI) is, the larger the spatial delocalization of holes (electrons). HDI and EDI are useful in quantifying breadth of spatial distribution for electrons and holes. As shown in Supplementary Figure 40b-c, the HDI and EDI of the transitions of Melem_6Sb3+ (ES3~ES30) are significantly larger than those of Melem_6 (ES25 and ES26) and Melem_6Na+ (ES9~ES26), indicating that both of the electrons and holes are highly concentrated after introduction of single atomic antimony sites.

2) Additionally, the computational hydrogen electrode (CHE) method also confirmed the preferred $2e^-$ ORR pathway on Sb-SAPC (Supplementary Figure 42). This free energy diagram could also be used to study the OER activity of Sb sites since the backward reaction for $4e^-$ ORR is $4e^-$ OER. It can be seen that the difference between *OH and *O is as high as 3.742 eV, indicating that a considerably large energetic barrier needs to be overcome for the $4e^-$ OER process. In this case, the Sb site should not function as an effective site to catalyze $4e^-$ OER.

Based on the above evidence, we can draw a conclusion that the Sb sites work as the

$2e^-$ ORR sites, and the N atoms on melem units work as the $4e^-$ OER sites.

**Supplementary Notes 8: Simulated Raman spectra for verification of adsorption configurations of $O_2$**

To investigate the side-on adsorption of $O_2$ on PCN, we have re-calculated the possible adsorption configurations of $O_2$ on PCN. In our case, a function of ω97xd at 6-311g(d) level was used for optimization to investigate the most favorable adsorption site for $O_2$ on PCN. The initial and optimized configurations are summarized in Supplementary Table S8. The calculation results show that the distance between $O_2$ and Melem_3 gradually increased during the optimization process. Therefore, the side-on adsorption of $O_2$ is not possible on site 2. On the contrary, $O_2$ can be adsorbed on site 1 of PCN with similar configuration to the previous literature. The distance between $O_2$ and the Melem unit is less than 1.5 Å. This bond length indicates that $O_2$ can be chemically adsorbed on site 1 with a typical side-on adsorption configuration.

To further understand the influence of $O_2$ adsorption configuration on the Raman spectrum, we calculated the Raman spectra of the optimized structure for Melem_3 and Melem_3Sb3+ after $O_2$ adsorption. The Raman spectra of Melem_3 and Melem_3Sb3+ before $O_2$ adsorption were also calculated for comparison (Supplementary Figure 44). A new chemical shift appears at around 820 $cm^{-1}$ (Supplementary Figure 44b) after $O_2$ adsorption on Melem_3. Similarly, a new chemical shift appears at around 780 $cm^{-1}$ (Supplementary Figure 44d) after $O_2$ adsorption on the Sb sites in Melem_3Sb3+. The relative position tendency of the changes in these newly observed chemical shifts are similar to the experimental results.

**Supplementary References**


[1] Shiraishi, Y. *et al.* Resorcinol–formaldehyde resins as metal-free semiconductor photocatalysts for solar-to-hydrogen peroxide energy conversion, *Nat. Mater.* **18**, 985-993 (2019).

[2] Gao, J. *et al.* Enabling direct $H_2O_2$ production in acidic media through rational design of transition metal single atom catalyst, *Chem* **6**, 1-17 (2020).

[3] Shiraishi, Y. *et al.* Sunlight-driven hydrogen peroxide production from water and molecular oxygen by metal-free photocatalysts, *Angew. Chem.* **126**, 13672-13677 (2014).

[4] Kofuji, Y. *et al.* Carbon nitride–aromatic diimide–graphene nanohybrids: Metal-free


**Commented [TB67]:** Please change to Supplementary References

**Commented [TB68R67]:** We have change phrase 'Reference' to 'Supplementary References'.

photocatalysts for solar-to-hydrogen peroxide energy conversion with 0.2% efficiency, *J. Am. Chem. Soc.* **138**, 10019-10025 (2016).

[5] Kofuji, Y. et.al, Hydrogen peroxide production on a carbon nitride-boron nitride-reduced graphene oxide hybrid photocatalyst under visible light, *ChemCatChem* **10**, 2070-2077 (2018).

[6] Kaynan, N., Berke, B.A., Hazut, O. & Yerushalmi, R. Sustainable photocatalytic production of hydrogen peroxide from water and molecular oxygen, *J. Mater. Chem. A* **2**, 13822–13826 (2014).

[7] Wang, L. *et al.* Simultaneous hydrogen and peroxide production by photocatalytic water splitting, *Chin. J. Catal.* **40**, 470-475 (2019).

[8] Hou, W.-C. & Wang, Y.-S. Photocatalytic generation of $H_2O_2$ by graphene oxide in organic electron donor-free condition under sunlight, *ACS Sustainable Chem. Eng.* **5**, 2994−3001 (2017).

[9] Kofuji, Y. et al. Mellitic triimide-doped carbon nitride as sunlight-driven photocatalysts for hydrogen peroxide production, *ACS Sustainable Chem. Eng.* **5**, 6478-6485 (2017).

[10] Qiu, C. *et al.* Photocatalysis: highly crystalline K-intercalated polymeric carbon nitride for visible-light photocatalytic alkenes and alkynes deuterations, *Adv. Sci.* **6**, 1970002 (2019).

[11] Bredas, J.-L. Mind the gap! *Mater. Horiz.* **1**, 17-19 (2014).

[12] Qu, X. *et al.* The effect of embedding N vacancies into g-$C_3N_4$ on the photocatalytic $H_2O_2$ production ability via $H_2$ plasma treatment, *Diamond Relat. Mater J.* **86**, 159-166 (2018).

[13] Zhu, B., Xia, P., Ho, W. & Yu, J. Isoelectric point and adsorption activity of porous g-$C_3N_4$, *Appl. Surf. Sci.* **344**, 188-195 (2015).

[14] Teng, Z. *et al.* Bandgap engineering of ultrathin graphene-like carbon nitride nanosheets with controllable oxygenous functionalization, *Carbon* **113**, 63-75 (2017).

[15] Zhang, P. *et al.* Modified carbon nitride nanozyme as bifunctional glucose oxidase-peroxidase for metal-free bioinspired cascade photocatalysis, *Nat. Comm.* **10**, 940 (2019).

[16] Kim, S. *et al.* Selective charge transfer to dioxygen on $KPF_6$-modified carbon nitride for photocatalytic synthesis of $H_2O_2$ under visible light, *J Catal.* **357**, 51-58 (2018).

[17] Moon, G.-H. *et al.* Eco-friendly photochemical production of $H_2O_2$ through $O_2$ reduction over carbon nitride frameworks incorporated with multiple heteroelements, *ACS Catal.* **7**, 2886-2895 (2017).

[18] Govind, N., Lopata, K., Rousseau, R., Andersen, A. & Kowalski, K. Visible light absorption of N-doped $TiO_2$ rutile using (LR/RT)-TDDFT and active space EOMCCSD calculations. *J. Phys. Chem. Lett.* **2**, 2696-2701 (2011).

[19] Ghuman, K.K. *et al.* Photoexcited surface frustrated Lewis pairs for heterogeneous photocatalytic $CO_2$ reduction, *J. Am. Chem. Soc.* **138**, 1206-1214 (2016).

[20] Lu, T. Multiwfn -A Multifunctional Wavefunction Analyzer-Software Manual. http://sobereva.com/multiwfn/misc/Multiwfn_3.7.pdf (2020).

[21] Liu, Z., Lu, T. & Chen, Q. An sp-hybridized all-carboatomic ring, cyclo[18]carbon: Electronic structure, electronic spectrum, and optical nonlinearity, *Carbon* **165**, 461-467 (2020).